עבודת גמר (תזה) לתואר
דוקטור לפילוסופיה

מוגשת למועצה המדעית של
מכון ויצמן למדע
רחובות, ישראל

Thesis for the degree
Doctor of Philosophy

Submitted to the Scientific Council of
the
Weizmann Institute of Science

במתכונת "רגילה"
In a "Regular" Format

מאת
מרקו קורטסי

By
Marco Cortesi

איבחון סרטן הערמונית באמצעות מיפוי לא פולשני של האבץ בערמונית ע"י פלואורסנציה בקרינת X (XRF)

Prostate-cancer diagnosis by non-invasive prostatic Zinc mapping using X-Ray Fluorescence (XRF)

מנחה:
פרופ׳ ע. ברסקין
ד״ר ר. צ'צ'יק

Advisor:
Prof. Amos Breskin
Dr. Rachel Chechik

נובמבר 2010

November 2010

This Ph.D. research was performed under the supervision of Prof. A. Breskin and Dr. R. Chechik at the Particle Physics Department of the Weizmann Institute of Science, Rehovot, Israel.

Acknowledgments:

I would like to express my deep gratitude to all of those who advised, supported and helped me to carry out this work.

In particular, I would like to thank my supervisors, Prof. Amos Breskin and Dr. Rachel Chechik, without whose help, encouragement and patience, not to mention their unsurpassed knowledge in the field of radiation and radiation detection physics, this thesis would not have been possible. Their good advice, support and friendship have been invaluable on both an academic and a personal level, for which I am extremely grateful.

I am grateful to Prof. David Vartsky and Dr. Sana Shilstein, for their guidance and for conversations that clarified my thinking on this and other matters. Their friendship and professional collaboration meant a great deal to me.

We have learnt a great deal from those who have worked with us over the years and gratefully acknowledge our debt to them, especially Dr. Eddi Fridman, Dr. Alexander Volkov, Dr. Gil Raviv and Dr. Jacob Ramon from the Institute of Pathology and the Department of Urology of the Sheba Medical Center, Tel Hashomer, Israel.

A number of colleagues and students cooperated and shared interest along the way, making the laboratory a pleasant and congenial environment. In this regard, I am indebted to Dr. Volker Dangendorf, Dr. Sergei Shchemelinin, Dr. Chen Shalem, Irene Carne, Giorgio Carlo Brambilla, Dr. Lior Arazi, Carlos Azevedo, Dr. Hugo Natal da Luz, Dr. Joost Melai, Dr. Jun Miyamoto, Shai Cohen, Dan Rubin, Michael Pitt and Roi Kaner; a special thank to Dr. Alexey Lyashenko and Raz Alon.

This research would not have been possible without the financial assistance, academic and technical support of the Weizmann Institute of Science and of the Particle Physics Department and its staff.

In conclusion, I would like to express my deepest gratitude to the Sergio Lombroso Program, especially to the Di Segni family, for giving me the possibility to start my Ph.D. research project at the Weizmann Institute and for their uninterrupted encouragement and support.

To My Family

Abstract:

At present, the major screening tools (PSA, DRE, TRUS) for prostate cancer lack sensitivity and specificity, and none can distinguish between low-grade indolent cancer and high-grade lethal one. The situation calls for the promotion of alternative approaches, with better detection sensitivity and specificity, to provide more efficient selection of patients to biopsy and with possible guidance of the biopsy needles.

The prime objective of the present work was the development of a novel non-invasive method and tool for promoting detection, localization, diagnosis and follow-up of PCa. The method is based on in-vivo imaging of Zn distribution in the peripheral zone of the prostate, by a trans-rectal X-ray fluorescence (XRF) probe.

Local Zn levels, measured in 1–4 mm^3 fresh tissue biopsy segments from an extensive clinical study involving several hundred patients, showed an unambiguous correlation with the histological classification of the tissue (Non-Cancer or PCa), and a systematic positive correlation of its depletion level with the cancer-aggressiveness grade (Gleason classification). A detailed analysis of computer-simulated Zn-concentration images (with input parameters from clinical data) disclosed the potential of the method to provide sensitive and specific detection and localization of the lesion, its grade and extension. Furthermore, it also yielded invaluable data on some requirements, such as the image resolution and counting-statistics, requested from a trans-rectal XRF probe for in-vivo recording of prostatic-Zn maps in patients. By means of systematic table-top experiments on prostate-phantoms comprising tumor-like inclusions, followed by dedicated Monte Carlo simulations, the XRF-probe and its components have been designed and optimized. Multi-parameter analysis of the experimental data confirmed the simulation estimations of the XRF detection system in terms of: delivered dose, counting statistics, scanning resolution, target-volume size and the accuracy of locating at various depths of small-volume tumor-like inclusions in tissue-phantoms.

The clinical study, the Monte Carlo simulations and the analysis of Zn-map images provided essential information and promising vision on the potential performance of the Zn-based PCa detection concept. Simulations focusing on medical-probe design and its performance at permissible radiation doses yielded positive results - confirmed by a series of systematic laboratory experiments with a table-top XRF system.

Our studies led to a conceptual design of a medical Zn-imaging trans-rectal prostatic probe for PCa detection and diagnosis and on its expected performance.

Table of Contents

Notations

%gland	Fraction of Surface Occupied by the Glandular Tissue
AUC	Area under ROC curve
BPH	Benign Prostatic Hyperplasia
CT	Computed Tomography
DRE	Digital Rectal Examination
EDXRF	Energy-Dispersive X-Ray Fluorescence
FFT	Fast Fourier Transform
FWHM	Full Width at Half Maximum
HIFU	High-Intensity Focused Ultrasound
HOPG	Highly Oriented Pyrolytic Graphite
ICC	Incomplete Charge Collection
ICRP	International Commission on Radiological Protection
KMC	Kaplan Medical Center (Rehovot, Israel)
keV	Kilo-electron volt (1 keV = 1.6 10^{-16} Joule)
K-S	Kolmogorov-Smirnov statistical test
LOD	Limit of Detection
MC	Medical Centre
MCNP	Monte Carlo N-Particle simulation code
Mo	Molybdenum
MRI	Magnetic Resonance Imaging
P/B	Peak-To-Background ratio
PCa	Prostate Adenocarcinoma
PCA3	Prostate Cancer Antigen 3 (also referred to as DD3)
Poly-CCC	Poly-conical capillary collimator
ppm	One Part per Million (1 ppm = 1 μg/g)
PSA	Prostate-Specific Antigen
ROC	Receiver Operating Characteristic
SMC	Sheba Medical Center (Tel-Hashomer, Israel)
TE	Tissue Equivalent
TRUS	Trans-rectal Ultrasound
TRNB	Trans-rectal Ultrasound-guided Needle-Biopsy
TURP	Transurethral Resection of Prostate
US	Ultra-Sound
XRD	X-rays Diffraction
XRF	X-rays Fluorescence
Z_{eff}	Effective photoelectric atomic number
Zn	Zinc
Zr	Zirconium

1. Introduction

The thesis work was motivated by the need for novel efficient methods of prostate cancer (PCa) screening and diagnosis. Though the lack of efficacy and specificity of current screening methods was well known, recent publications in the New England Journal of Medicine (Andriole et al. 2009; Schröder et al. 2009; Lee et al. 2009) clearly point at the remarkable deficiency of the currently used PSA test. The North American study showed no reduction in PCa mortality attributable to PSA screening, while a 20% reduction in mortality was observed in the European study, together with a significant false-positive rate of ~50% (Schröder et al. 2009). PSA remains though a major screening tool, together with DRE, despite the fact that none of these are sufficiently specific; although a total PSA exceeding 4 ng/mL is the generally accepted threshold for recommending a prostate biopsy, this value of 4 ng/mL was established by somewhat arbitrary means. For example, in multiple major screening studies (Selly et al. 1997), it was reported that the positive predictive value (PPV) in a patient with a PSA 4-10 ng/mL and normal DRE is 18% to 25% (mean, 21%), and when PSA is > 10 ng/mL, the PPV is 58% to 64% (mean, 61%) (Jeldres et al. 2008, Babaian et al. 1992, Aziz et al. 1993, Bangma et al. 1995). Most high-PSA patients suffer benign diseases, and as a result an unnecessary large number of patients are referred to Trans-rectal Ultrasound-guided Needle-Biopsy (TRNB) examination which serves as a secondary screening test. Furthermore, none of the above screening methods provide any indication about tumor dimensions (clinical staging), location or differentiation (histological staging). The entirely lack of such information, which could serve as guidance during the selection of the needle-biopsy site, renders the TRNB a rather “blind” procedure. For instance, based mostly on PSA test, the urologists in USA performed ~1.5 million TRNB in 2006, of which 80% turned out to be negative for PCa (Etzioni et al. 2002).

Relying on biopsy-based detection and grade assignment is dangerous not only because of the known limited sensitivity of this examination (it captures only ~70% of PCa cases in the first biopsy and up to ~85% in repeated) but also because of the limited tissue volume involved; as an example, the biopsy-based Epstein criterion, for 336 patients underwent radical prostatectomy, was recently shown to be falsely optimistic in about 24% of the cases (Jeldres et al. 2008). More details on the current status of PCa diagnosis rates can be found in (Concato et al. 2006; Graif et al. 2007; Jemal et al. 2007).

Therefore, the pursuit for new screening and diagnostic techniques for prostate cancer is currently an animated field of interest: on the one hand, heading for Molecular Biology/Genetic

markers in blood or urine screening tests (Mol et al. 2007; Leman et al. 2007; Karam et al. 2007; Catz & Johnson 2003; Petrescu et al. 2006; Jiang et al. 2004; Marks & David G Bostwick 2008), on the other, it is heading for improved Ultra Sound or MRI based imaging modalities (Kravchick et al. 2003; Moskalik et al. 2001; Govindaraju et al. 2008; Nakashima et al. 2004). Blood or urine tests are simple and possibly economic approaches for screening large population; nevertheless, current tests suffer from very low sensitivity and specificity with no staging or grading information. The imaging approaches have the potential benefit of providing location information, with a potential of guiding biopsy and treatment tools. Such information provided at an early phase of the diagnosis chain could be very important since the majority of PCa cases are low-grade, dormant lesions that do not call for immediate intervention. Numerous improvements of standard TRUS have been developed, such as the power Doppler imaging (DPI) (Nakanouchi et al. 2001; Govindaraju et al. 2008), the Color Doppler TRUS (CDUS) (Kravchick et al. 2003) and the Three-dimensional Doppler (3DD) (Moskalik et al. 2001). However, these modalities cannot reliably reveal the pathological stage of the lesions (Scattoni et al. 2005), which is a crucial factor for the choice of treatment and the prognosis. No other proposed imaging methods introduced so far (like pelvis CT, bone scintigraphy, abdomen PET) have the potential to provide detailed information regarding the tumor grade.

The Magnetic Resonance (MR) techniques are some of the most powerful tools available for evaluating PCa. Conventional MR imaging (MRI) provides more detailed depiction of the anatomy of the prostate and surrounding structures than any other imaging modality. MRI may enhance PCa staging compared with clinical evaluation, transrectal ultrasound, or computed tomography (CT), allowing for concurrent evaluation of prostatic, periprostatic, and pelvic anatomy. Though conventional MRI is generally limited in its ability to differentiate PCa from other abnormalities within the peripheral zone, the addition of dynamic contrast-enhanced MRI (DCE-MRI) to conventional imaging methods improves PCa localization in most cases and may improve diagnostic performance (Fuchsjäger et al. 2008). In addition, imaging capabilities are enhanced using 3 Tesla MRI (3-T MRI) compared to standard lower-field magnets (e.g. 1.5 Telsa); the 3-T MRI results in two-fold higher signal-to noise ratios (SNR) compared to 1.5 T (Futterer et al. 2004); Sosna et al. showed an image quality at 3 Tesla without an endorectal coil to be comparable to that at 1.5 Tesla with an endorectal coil, which is of practical advantages (Sosna et al. 2004).

MR spectroscopy (MRS) adds sensitivity and specificity to conventional MRI of biological information associated with many different metabolites (Negendank 1992); useful

molecules that can be studied with MRS for PCa include water, lipids, choline, citrate, lactate, creatine, and amino acids.

The prostate gland is unique by the fact that it contains high levels of citrate and polyamines (Costello and Franklin 1994); as the normal glandular epithelial cells are replaced by cancer, the concentration of citrate, polyamines and choline change in the transformation to a malignant state. Choline levels increase and citrate levels decrease in the presence of active cancer (Costello et al. 1999). The reason for the decline in the levels of citrate is likely in correlation with the altered intermediate metabolism in the Krebs cycle – see chapter 2.1. Although the mechanism choline peaks elevation is less understood, it is thought to be associated with changes in cell membrane synthesis and degradation that is normally associated with cancer; it likely reflects the increase in lipogenesis/cholesterogenesis associated with malignant cell activity.

The criteria for PCa diagnosis with MRS rely on increased choline-to-citrate ratios. The majority of prostate MRS-imaging data in the literature is derived from 1.5 Tesla systems; since the choline cannot be discriminated from creatine, the ratio measured is indeed that of choline plus creatine to citrate (choline+creatine/citrate). Higher fields result in better SNR, smaller voxel size, improved temporal resolution, and more accurate separation of metabolite peaks. For instance, MRS performed at 3T enables distinction of the choline peak from the creatine peak, improving specificity (Futterer et al. 2005). Besides choline, citrate and creatine analysis, newer image acquisition and analysis software may enable evaluation of other metabolites such as the polyamine peaks; Shukla-Dave et al. reported the feasibility of evaluating polyamines by MRS and concluded that the polyamine peaks may be lower than the choline peak in tumors (Shukla-Dave et al. 2007). In addition, it has been demonstrated that MRS of prostate tumors (Choline+Creatine/Citrate) and tumor volume correlate with pathologic Gleason score, though there was an overlap between MRS imaging parameters at various Gleason score levels, which may result from both the methodology and physiological variations (Zakian et al. 2005, Fradet et al. 2010).

The overall sensitivity of combined MRI/MRSI as measured in various studies was 57%–100%, whereas specificity was 44%–96% (Panebianco et al. 2009).

Although the combination of MRI and MRSI in conjunction with the endorectal and phased-array body coil is emerging as a sensitive tool for anatomic and metabolic evaluation of the prostate gland (De Visschere et al. 2010), the application of this technology has proven to be far from trivial; the deep location of the prostate, the possible movement of the prostate gland

during the MRSI acquisition, and the dominating triglyceride signals from the surrounding adipose tissues often pose a challenge in obtaining reliable data. In addition, despite their qualities, MR methods **cannot be considered as a means for screening large portions of population** due to their prohibitive costs. Nevertheless, improving cancer detection rate of biopsy, selecting cases for watchful management or repeated biopsy, directing probes to the affected part for the treatment, follow-up after definitive treatment for detecting recurrence, etc., are some aspects where MRSI might play a role in the near future (Nayyar et al. 2009).

The present research aimed at validating the concept and developing a novel method for the detection and grading of adenocarcinoma of the prostate by a trans-rectal X-ray fluorescence (XRF) probe (Shilstein et al. 2004; Shilstein et al. 2006; Vartsky et al. 2003). The proposed diagnostic procedure consists of mapping the Zn distribution in the peripheral zone of the prostate, by local X-ray irradiation of the gland followed by the measurement of characteristic Zn emission. **Sites of depleted Zn would be indicative of PCa, with the depletion level uniquely indicating the disease aggressiveness (grade).**

The scanning of the prostate's peripheral zone is expected to provide a 2D digital image of Zn-distribution within an acceptable irradiation time and with permissible absorbed dose, carrying information on the pathological stage of the examined gland (Cortesi et al. 2009). Though the proposed method is limited to the backside of the peripheral zone, it should be reminded that 70% of PCa lesions develop in this zone, constituting the more severe form of the disease (Theodorescu 2009). Indeed, central- and transitional-zone carcinomas, occurring respectively in 10% and 20% of the cases (McNeal 2003), are less aggressive (low Gleason score) and in any case are not probed nowadays by needle biopsy (Shannon et al. 2003). Ductal carcinoma (<1% of PCa) disease, not probed by needle biopsy, is diagnosed by TURP (McNeal et al. 1988). Thus the proposed method addresses the same prostatic region probed by needle biopsy, but probing a hundred-times larger tissue mass (roughly 5.4cc compared to 0.05cc probed by a 12-needle biopsy); moreover, since in 90% of the cancer cases at least one lesion is located within 5 mm from the rectal wall (derived from this study), the sensitivity of the method, even though with a limited depth, is expected to be significantly greater than that of biopsy.

The new concept and medical probe are expected to have a significant impact on PCa screening, promoting early detection of clinically-significant tumors. It is expected to improve patient selection for biopsy, screening out benign conditions; following PSA test, this should permit reducing the PSA threshold, without the overload of un-necessary biopsies. It could also improve

selection of needle-biopsy sites, indicate pre-operative tumor location and extension as well as a guiding tool for local PCa treatments; it can also serve for non-invasive follow-up.

The new method has the potential of reducing mortality and morbidity of PCa patients.

2. Scientific background

2.1 Role of Zn in the pathogenesis of PCa

Zn is an essential trace element in the human body; it is involved in many important and diverse functions of the human metabolism (Prasad 1982), it affects several organ systems functioning (Hambidge & Krebs 2007) and it plays an important role in wide range of cellular processes, including cell division and proliferation (MacDonald 2000), immune function (Shankar & Prasad 1998), defenses against free radicals (T. M. Bray et al. 1986); it also helps to protect cellular components from oxidation and damage (Yan et al. 2008). In the seminal fluid, Zn acts as an antibacterial factor (Kavanagh 1983). Low Zn concentration in seminal plasma may also affect the mobility of sperm which can result in infertility (Carreras & Mendoza 1990).

At the beginning of the twentieth century, Bertrand and Vladesco were the first to show the remarkably high concentration of Zn in the human prostate (Bertrand & Vladesco 1921). Their result was later confirmed by Mawson and Fisher, who recounted that Zn concentration in human and mammalian prostate glands was around 10 times higher than those in the majority of soft tissue (Mawson & Fischer 1951). In a succeeding paper, the same authors reported that Zn concentration in malignant prostate tumors were much lower than those in healthy prostate tissue (Mawson & Fischer 1952). These early results initiated and promoted a series of more exhaustive studies of Zn contents in healthy prostate glands and in those affected by different prostate diseases, including chronic prostatitis, BPH, PCa of different cancer staging (Hoare et al. 1956; Schrodt et al. 1964; F. Gyorkey et al. 1967; Gonick et al. 1969; Dhar et al. 1973; Habib et al. 1979; Feustel et al. 1982; V. Zaichick et al. 1997; Costello et al. 2004). In this context, it is worthwhile to mention in details the pioneering work of Zaichick et al., from the late 1970s: a XRF elemental analysis were performed on dried needle-biopsy cores segments, reveling 7–8 eightfold decrease in Zn concentration in PCa tissue compared to normal one or BPH (V. Zaichick et al. 1997) - no dependence on the tumor stage and histological grade is reported. However, we should bear in mind that this 30-years old study relates to a clinical situation which is uncommon at present: 40% of the patients in their study had distant metastases or positive findings in regional lymph nodes; although not specified, we may assume that the majority of their patients had a considerably advanced stage disease.

Zn is not uniformly distributed throughout the different anatomical regions of the prostate (figure 1). As documented by ref. (F. Gyorkey et al. 1967), Zn content is highest in the lateral lobe of the peripheral zone (PZ), on average of about 200 ppm wet weight. Central (CZ), transitional

(TZ) and anterior (AZ) zones show a much lower Zn concentration, of about 100 ppm wet weight. The PZ comprises up to 70% of the normal prostate gland in young men, including the sub-capsular portion of the prostate gland which surrounds the distal urethra (figure 1).

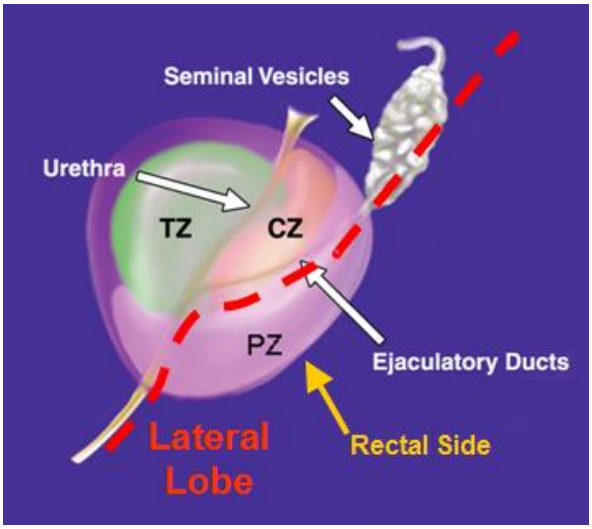

Figure 1. Anatomy of the prostate.

The lateral lobe of the PZ, accessible through the rectum, is the palpable portion of the gland in DRE and it is the region where more than 70% of prostatic cancerous tumors originate (Naz 1997). The CZ constitutes approximately 20-25% of the normal prostate gland and it accounts for roughly 10% of all PCa, while the TZ, being around 15-20% of the prostate volume, is responsible for BPH onset in addition to around 20% of the adenocarcinomas. TZ and CZ tumors are generally diagnosed incidentally during TURP undertaken for clinical BPH; they show organ-confined diseases (Noguchi et al. 2000), with low aggressiveness and thus more favorable prognosis under these conditions (McNeal et al. 1988).

Another interesting factor to consider is the difference in the density and distribution of Zn, at the single cell level, in cancerous and normal tissues. As shown by (Ide-Ektessabi et al. 2002) using SR-XRF analysis applied to both cancerous and control tissues of the human prostate, in comparison with the glandular epithelium part of the prostate tissue, the density of Zn in the normal tissue resulted to be at least twice higher than that in the cancer tissue. On the contrary, the difference in the average density of Zn in the stroma turned out not so significant between cancer and normal tissues.

According to (Costello et al. 2000), the unique functional capability of the normal peripheral zone of the prostate to accumulate extremely high Zn concentration is associated with the accumulation of high intracellular level of Zn, in particular with the remarkable high mitochondrial

Zn level. Furthermore, the high level of Zn in mitochondria is essential to inhibit m-aconitase activity, which limits the oxidation of citrate via the Krebs cycle and allows its accumulation (Costello et al. 1995). By this mechanism, Zn may be regarded as a true compelling regulator of the Krebs cycle and the related energy metabolism of prostate epithelial cells - with inhibited citrate oxidation the cellular ATP synthesis cycle operates only at 30% of its efficiency. Since mobile reactive Zn that can have toxic effects (Vallee & Falchuk 1993), while other mammalian cells generally possess mechanisms that prevent accumulation of high Zn levels, and since the inhibition of m-aconitase and citrate oxidation is lethal, it then well understood that the accumulation of extraordinarily of high levels of Zn, leading to the specialized metabolic process of ‘‘net citrate production’’, is a unique and peculiar feature of the normal peripheral zone glandular epithelium of the prostate. Notice that the level of prostate m-aconitase enzyme appears to be similar to that associated with other cells, although the levels of m-aconitase activity and citrate oxidation are significantly lower in prostate cells.

Nevertheless, what specific function the high citrate content accomplishes in semen still remains an unanswered question. Suggested functions include a role of citrate as a buffer to maintain the pH of semen (Kavanagh 1985); as a chelator for highly concentrated cations (including Zn) involved in liquefaction of semen (Mann & Lutwak-Mann 1981); as an energy source for the viability of sperm and/or the capacitation process of fertilization (Hicks et al. 1972).

Further, according to the model proposed by Costello et al., neoplastic cells lose the ability of accumulating Zn and become dormant malignant cells. As the cellular Zn level declines, the pre-malignant cells undergo a metabolic transformation in which the inhibition of citrate oxidation (m-aconitase) is eliminated and the energy production rises. It has been reported (Costello & Franklin 1997), that normal human prostate tissue and BPH contains extraordinary high citrate levels (about 8000 to 15000 nmol/g tissue) while PCa sample contains relatives low levels (about 1000 to 2000 nmol/g tissue) – in principle PCa samples are generally admixture of malignant, normal and often BPH tissue, so the net citrate level of the PCa component must be considerably lower (around 100 to 400 nmol/g tissue).

One of the possible mechanisms responsible for this "metabolic" transformation is the down regulation of hZIP1, which is the major transporter responsible for the uptake and accumulation in prostate cells (Franklin et al. 2005).

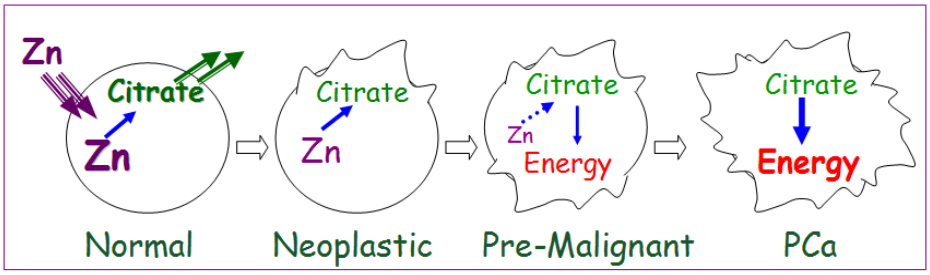

Figure 2.The progression of malignancy in prostatic epithelial cell according the model suggested by Costello et al.: the inhibitory effect of Zn on m-aconitase activity is responsible for the impaired citrate oxidation by normal citrate-producing prostate cells. The lost ability of the malignant cells to accumulate Zn removes the inhibition of existing m-aconitase so that citrate oxidation occurs.

So the pathogenesis of PCa involves the metabolic transformation of sane Zn-accumulating, citrate-producing cells to citrate-oxidizing cells that have lost the ability to accumulate Zn (figure 2). It was also speculated (Costello & Franklin 2006) that the accumulation of Zn exhibits tumor-suppressor effects that are incompatible with the process and activities of prostate malignancy. In addition, the restoration of high Zn levels in premalignant/malignant prostate cells may arrest and/or abort prostate malignancy (Liang et al. 1999).

2.2 Prostate-Cancer Grading, Gleason score

The histological grade, also called pathologic grade, is an important predictive factor of malignant disease, and is commonly used to define the potential for local and/or distant progression of malignant tumors (Gardner 1982). Not all adenocarcinomas progress along the same path: the majority of PCa cases are indolent with no clinical manifestation; in other cases, the disease is localized, well confined to the prostate, with very slow progression; other carcinomas, with metastatic potential, evolve rapidly to a life-threatening disease (Mikuz 1997). The rapidity and path of the carcinoma development depend on how closely the cancerous cells resemble normal ones.

Several grading systems for prostatic carcinoma have been proposed, based on various factors: differentiation capacity, architectural growth patterns, mitotic activity or nuclear abnormalities (Humphrey 2004). The most accepted histopathological grading system is the one proposed by Donald F. **Gleason** (Gleason 1992), which is presently the most practiced prognostic factor, being significantly associated with survival and/or progression of the PCa (David G. Bostwick 1995). The Gleason-grade system is based on the histological pattern of differentiation

and arrangement of carcinoma in hematoxylin-eosin (H&E)-stained sections. Five patterns are identified, from grade 1, being the most well-differentiated cancer (slow-growing), to grade 5, being the most poorly-differentiated cancer (most aggressive and fast-growing) (figure 3). To take into account the large heterogeneity displayed by the prostate-carcinoma tissue, to each tumor a primary and a secondary pattern-grade are assigned, with respect to the most common pattern (>50% of the total cancer-lesion area) and the second most common one (<50%, but ≥5% of the total cancer-lesion area). The two values, between 1 and 5, are added to generate the histological Gleason sum score (also called Gleason score and combined Gleason grade), ranging from 2 to 10 (Humphrey 2004).

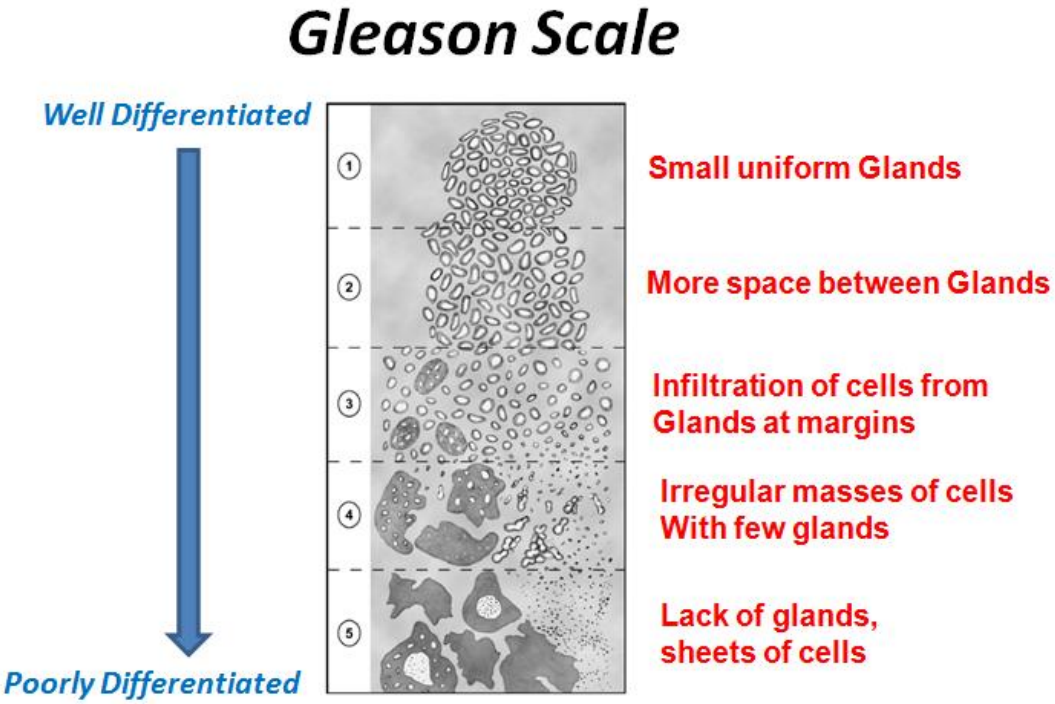

Figure 3. Schematic diagram of the Gleason grading system (Epstein et al. 2005). Gleason grade: lower grades are associated with small, closely packed glands. Cells spread out and lose glandular architecture as grade increases. Gleason score is calculated from grade as described in the text.

However, Gleason's original description of each pattern has undergone significant revision over the years, first by Gleason and his colleagues, and most recently at the 2005 International Society of Urological Pathology Consensus Conference (Epstein et al. 2005). As patterns 1 and 2 have become less common following the advent of immunohistochemical stains for basal cells (many tumors originally defined as pattern 1–2 by Gleason were probably benign glandular proliferations), pattern 3 has become the default lowest grade tumor in most settings (Berney 2007; Epstein 2000). For example, many of Gleason's original 1 + 1 = 2 adenocarcinoma of the prostate

would today probably be regarded as adenosis, a benign mimic of prostate cancer (Epstein 2000). As a result, the community of urologists and uropathologists agrees that, in handling and pathology reporting of prostate biopsies, the minimum Gleason score that should be reported from is 6 (T. L. Lotan & Epstein 2010; McWilliam et al. 2002).

In this Ph. D. thesis work we will adopt the more updated histological classification based on Gleason score, defining "well differentiated" a PCa of grade (3+3), as "moderately differentiated" the grades (3+4, 3+5, 4+3, 5+3), and as "poorly differentiated" the high Gleason grades (4+4 , 4+5 , 5+4 , 5+5). When specified, data analysis will be carried out considering single Gleason grade classification.

2.3 Elemental Analysis using Energy-Dispersive X-ray Fluorescence (EDXRF)

EDXRF is a common, simple and fast analytical technique used to identify and quantify the concentrations of elements present in environmental, geological, biological, industrial and other samples. Compared to other competitive techniques, such as Atomic Absorption Spectroscopy (AAS), Inductively Coupled Plasma Spectroscopy (ICPS) and Neutron Activation Analysis (NAA), EDXRF has the main advantage of being non-destructive. Since it does not cause any damage to the analyzed samples, it is possible to combine elemental analysis with histological examination of biological material, or to perform XRF analysis *in-vivo*. Furthermore, it provides a fairly uniform detection limit across a large portion of the Periodic Table and is applicable to a wide range of concentrations, from a 100% to few parts per million (ppm). Finally, the X-ray fluorescence analysis of trace elements in small samples has the advantage to be a remote approach, performed with a simple portable X-ray source.

XRF analysis is based on the fact that the X-rays emitted from an ionized atom have energies that are characteristic of the element involved. The fluorescence X-ray yield is proportional to the elemental concentration, energy and intensity of the radiation source, and to the self absorption within the material. X-ray photons may be produced by Roentgen tubes, radioactive isotopes, synchrotron radiation form particle accelerators (Bilderback et al. 2005) and with laser-induced techniques - see for example (Key 1985).

In the stable atom, electrons occupy discrete energy levels that are designated (in order of decreasing binding energy) K, L_l, L_2, L_3, M_l, ... M_5, N_l, ... N_7, and so forth. The minimum amount of energy required to release an electron from the atom, and thus the energy with which it is bound

to the nucleus, is referred to as the binding energy of the electron in the atom. The binding energies are different and characteristic for every element as a result of the varying number of electrons (or similarly to the number Z of the positive charges in the atomic nucleus).

When an atom is ionized, namely one or more electrons are ejected from the atom (it may takes place if the atom is exposed to radiation with an energy greater than the binding energy of the electron in that atom), the vacancy thus created is filled by an electron from an outer orbit. The resulting loss in potential energy may appear as a characteristic X-ray whose energy is equal to the difference in the binding energies of the two electron states. The relationship between the wavelength λ of a characteristic X-ray photon and the atomic number Z of the excited element was first established by Mosley (the Mosley's law), and it is written as

$$\frac{1}{\lambda} = K\,(Z - \sigma)^2 \tag{2.1}$$

in which K is a constant, of a different value for each spectral series, and σ is the shielding constant, of a value just less than unity.

The most frequent transitions between outer and inner shells are given names. For example, an L shell to K shell transition is traditionally identified as K_α transition. Other possible transitions are shown in figure 4.

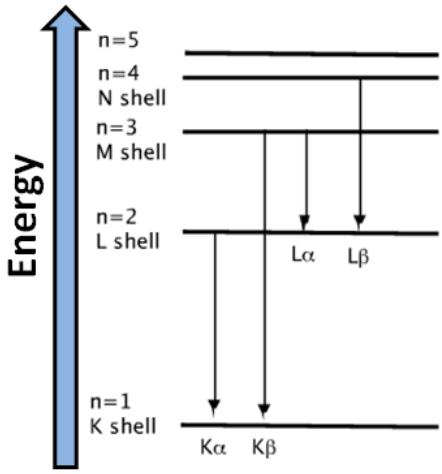

Figure 4. Depiction of electron shells and energy levels and transitions that give rise to X-ray emission line observed in X-ray fluorescence spectroscopy.

Not all ionizations result in X-ray emission. The Auger effect is a competing mechanism of atomic relaxation. In this process, the atom regains energy stability by emitting an outer shell electron. The ratio of the number of emitted X-rays to the total number of ionizations is called the fluorescence yield ω_i, where the index i designates the shell involved. Fluorescence yield increases

with atomic number Z and is greater than 95% for K-line X-ray emission of elements with Z >78. For a given element, the fluorescence yield decreases from the K series to the L and M series.

The fluorescence yield can be approximated by the following expression:

$$\omega_i = \frac{Z^4}{(A_i + Z^4)} \tag{2.2}$$

where A_i is in the order of 10^6 for the K shell and 10^8 for the L shell.

Consider a narrow beam of mono-energetic photons with an incident intensity I_0, penetrating a layer of material with thickness x [cm] and density ρ [g/cm^3]. The emerging photon beam has intensity I given by the following exponential attenuation law

$$\frac{I}{I_0} = \exp\left[-\left(\frac{\mu}{\rho}\right)\rho\, x\right] \tag{2.3}$$

where (μ/ρ) is the mass attenuation coefficient [cm^2/g] of the absorbing material.

From a general point of view, attenuation of photons by an absorbing material at very low energy is caused by three major types of interaction, namely coherent scattering, photoelectric effect and Compton effect. Each of these processes may be represented by its own mass attenuation coefficient which varies in its particular way with the energy of the photon and with the atomic number of the absorbing material. Thus the total mass attenuation coefficient is the sum of individual coefficients for these processes:

$$\left(\frac{\mu}{\rho}\right) = \left(\frac{\sigma}{\rho}\right)^{\mathrm{Comp}} + \left(\frac{\tau}{\rho}\right)^{\mathrm{Phot}} + \left(\frac{\delta}{\rho}\right)^{\mathrm{Coher}} \tag{2.4}$$

where $(\sigma/\rho)^{\mathrm{Comp}}$, $(\tau/\rho)^{\mathrm{Phot}}$ and $(\sigma/\rho)^{\mathrm{Coher}}$ are the mass attenuation coefficients for Compton scattering, photoelectric effect and coherent scattering (also known as Thomson or Rayleigh scattering), respectively. For mixtures and compounds the values of the mass attenuation coefficient (μ/ρ) can be obtained according to simple summation:

$$\left(\frac{\mu}{\rho}\right) = \sum_i w_i \left(\frac{\mu}{\rho}\right)_i \tag{2.5}$$

where w_i and $(\mu/\rho)_i$ are respectively the fraction by weight and the mass attenuation coefficient of the ith atomic constituent.

Tabulations for the mass attenuation coefficient - see for example (National Institute of Standard and Technology - NIST), rely heavily on the total cross section per atom, σ_{tot}:

$$\left(\frac{\mu}{\rho}\right) = \frac{\sigma_{tot}}{u\, A} \tag{2.6}$$

where u (= $1.66 \cdot 10^{-24}$ g) is the atomic mass unit (1/12 of the mass of an atom of the nuclide ^{12}C) and A is the relative atomic mass of the target element. The total cross section σ_{tot} is frequently given in units of b/atom (barns/atom), where b = 10^{-24} cm^2.

As an example, figure 5 illustrates a plot of the mass attenuation coefficient for Zn versus photon energy; the sharp discontinuities in the lower range of energy are due to photoelectric absorption edges. The edges indicate the sudden decrease in the photoelectric cross section for incident photon energies just below the binding energy of that particular electron state.

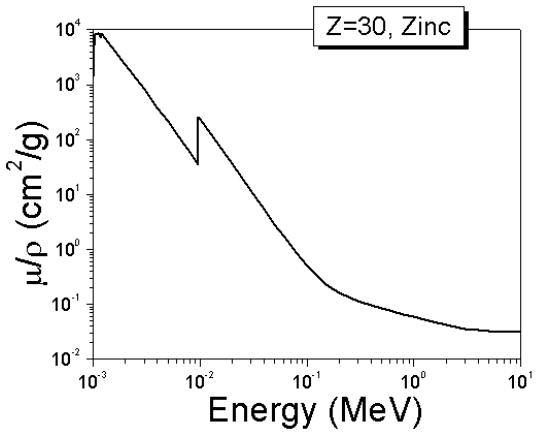

Figure 5. Zn mass attenuation coefficient μ/ρ as function of the energy (E) of the exciting photons; graph data were taken from NIST database (Seltzer 1993).

For a quantitative analysis of the composition of a sample, the X-ray fluorescence emission rate must be related to the element concentration. For simplicity, consider a far-field measurement geometry where the sample (composed of different elements, each of them with density ρ_i) is approximated by a slab and the excitation source is mono-energetic (see figure 6).

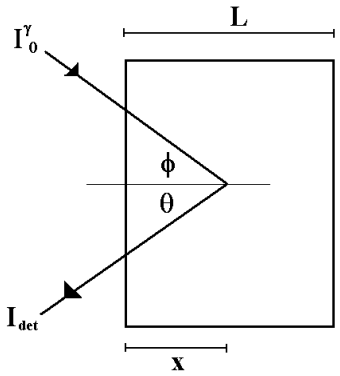

Figure 6. General XRF slab geometry.

The fluence rate I_x^y of excitation photons at a depth x in the sample is given by

$$I_x^y = I_0^y \exp\left[-\mu^y \frac{x}{\cos(\phi)}\right] \tag{2.7}$$

where $\mu^y = \sum \mu_i^y \rho_i$ is the total linear attenuation coefficient, at energy y, and I_0^y is excitation fluence rate at sample surface.

The number of excitation photons N_x that interact in the volume dx and create a K-edge X-rays fluorescence photon, per unit time, is given by

$$N_x\, dx = I_x^y \rho_j \left(\frac{\tau}{\rho}\right) \omega \frac{A\, dx}{\cos(\phi)} = I_0^y \exp\left[-\mu^y \frac{x}{\cos(\phi)}\right] \rho_j \left(\frac{\tau}{\rho}\right) \omega \frac{A\, dx}{\cos(\phi)} \tag{2.8}$$

where (τ/ρ) is the mass attenuation coefficient for the K-shell photoelectric effect, A is the cross section of the excitation beam, ω is the K fluorescence yield and ρ_j is the density of the element under study. The fluorescence X-rays are attenuated within the sample according to the equation

$$N_x(out) = N_x \exp\left[-\mu^\upsilon \frac{x}{\cos(\theta)}\right] \tag{2.9}$$

where $\mu^y = \sum \mu_i^\upsilon \rho_i$ is the total linear attenuation coefficient, at energy ν.

Combining and integrating the above equations, the portion of K-edge X-ray fluorescence photon flux (phot/s) reaching a detector surface is expressed as:

$$I_{det} = \frac{I_0^y \rho_j \left(\frac{\tau}{\rho}\right) \omega\, \Omega\, A}{4\pi\left[(\cos(\theta)/\cos(\phi))\,\mu^y + \mu^\upsilon\right]} \left\{1 - \exp\left[-\left(\frac{\mu^y}{\cos(\phi)} + \frac{\mu^\upsilon}{\cos(\theta)}\right) L\right]\right\} \tag{2.10}$$

where Ω is the detector solid angle.

The factor $[(\Omega/4\pi)\,(\cos(\varphi)/\cos(\theta))]$ has been added for normalization. If the exciting beam is polychromatic then the equation (2.8) must be integrated over the exciting spectrum.

When the sample is infinitely thick for the radiation of interest, we may simply write

$$I_{det} = \frac{I_0^y \rho_j \left(\frac{\tau}{\rho}\right) \omega\, \Omega\, A}{4\pi\left[(\cos(\theta)/\cos(\phi))\,\mu^y + \mu^\upsilon\right]} \propto \rho_j \tag{2.11}$$

The above result is very important for XRF elemental analysis because it implies that the measured X-ray flux I_{det} is directly proportional to the concentration of the fluoresced element ρ_j.

3. Assessment of the Cancer Diagnostic Value of Prostatic Zn – a clinical study

In order to assess the potential diagnostic value of Zn-content measurement and prostatic Zn-map imaging, we have undertaken a broad clinical study (first of its kind), encompassing around 600 patients referred to TRNB - these patients had abnormal findings in their DRE or PSA. The Zn distributions in needle-biopsy samples have been measured with the means of a dedicated XRF analyzer and correlated with histological diagnosis, cancer aggressiveness grade (Gleason score) and other relevant medical parameters like patient age, PSA level, gland size etc. In spite of the recognized potential of Zn concentration as a specific and early cancer indicator, *in-vivo* prostatic Zn measurements for PCa detection in clinic have never been reported. The impediments are twofold: the technical complexity of such an *in-vivo* measurement and the fact that the distribution of mean prostatic-Zn concentrations in malignant and benign tissue have a significant overlap (Lahtonen 1985; Habib et al. 1979; V. Zaichick et al. 1997). This large overlap is probably related to the size of the cancerous lesions, namely, a large lesion occupying a significant fraction of the prostate volume exhibits a significant drop of the mean Zn-concentration value, while small lesions may have a negligible effect on the measured mean. This understanding poses an even greater challenge on the idea of exploiting Zn concentration for PCa detection, because it implies that **only a local Zn-detection approach may carry relevant diagnostic value**.

This clinical study described here involved the development of methods for investigating small fresh samples and methods for reliable calibration of the XRF instrumentation. It also involved spectroscopic analysis of a vast amount of collected data and a detailed data analysis searching for the most meaningful and relevant correlations between Zn concentration, histological results and other clinical data.

3.1 Material and Methods

The Zn-concentration measurements in biopsy samples were carried out, in parallel, in two medical centers, with two tabletop XRF systems: a locally assembled system at the Kaplan Medical Center (KMC) and a commercial unit (EX-2600 bench top XRF analyzer, Jordan Valley Applied Radiation, Israel.), custom-modified for our application, at Sheba Medical Center (SMC) (figure 7); the latter system, with fully automated operation, had about 20-fold higher X-ray flux and superior

spectral performance. Both XRF systems were calibrated with the same calibration standards (see section 3.1.1), permitting to combine data from the two experiments, if desired.

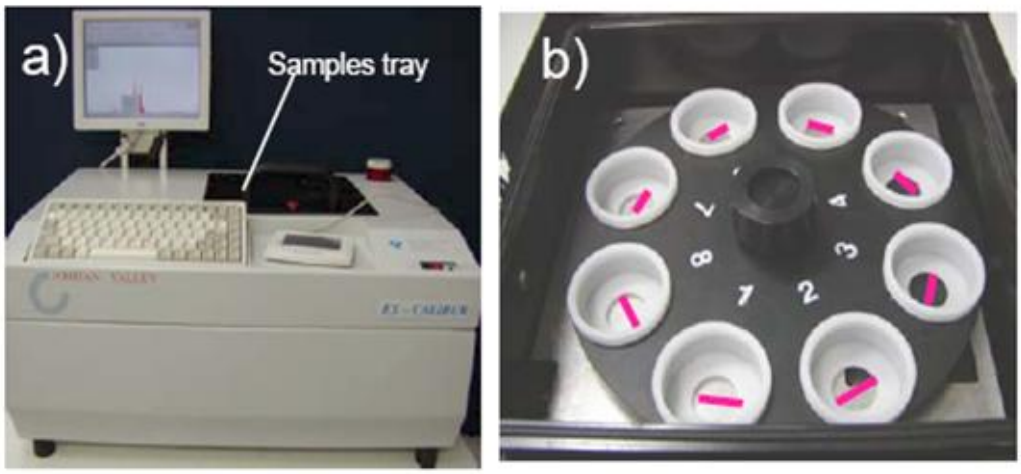

Figure 7. a) The EX-2600 bench-top XRF analyzer used at SMC; b) Details of the carousel with 8 biopsy sample placed in dedicated cups for XRF.

At KMC, up to six needle-biopsy samples per patient, each being a 0.5 mm in diameter and 15–20 mm long tissue cylinders folded in two, were placed at 8 mm distance on a sample-table; the latter was made of a 2.5 μm Mylar foil stretched on a rectangular plastic frame. Wet sponges and water drops were placed at the table edges; the samples were covered with an identical Mylar foil (see figure 8a). This procedure was found to ensure minimal scattering from the table constituents; it also prevented sample drying during the measurements (measured to be ≈ 1%). The sample-table was linearly translated manually, introducing one sample at a time into the measurement site. The irradiated area on the sample-table was 4×9 mm^2, defined by a rectangular aperture on the primary beam. Signals from the X-ray detector, after proper amplification and time-shaping, were analyzed by a PC-borne multi-channel analyzer (MCA); the stored spectra were then analyzed and the intensities of the Zn fluorescence peak as well as the Compton-scattering peak were recorded, which permitted deriving the absolute Zn content as explained below. The measurements, carried out over a fixed time duration of 120 s per sample, yielded the average Zn content per sample with a precision (defined by the number of counts within the peaks) ranging from 30% to 5%, for 30 and 500 ppm, respectively. Due to the manual handling of sample displacement and data acquisition, and the relatively long measurement time per sample (dictated by the limited X-ray generator flux), sample measurements of each patient lasted 20–30 min.

At SMC, in the automatic XRF system, up to eight needle-biopsy samples, aligned in the tangential direction, were mounted on a rotating table. Each sample was placed on a 2.5 μm Mylar foil fixed on standard plastic cups (inner diameter 24 mm) which, in turn, were tightly fitted into Al cups placed on the instrument table; the Al cups were sealed by an identical Mylar foil. (To eliminate contribution from traces of Zn in the plastic cups material, a thin Al layer was inserted in these cups, see figure 8b.) Thus each sample was individually sandwiched between the two Mylar foils, which prevented them from drying. The sample loading procedure took only a couple of minutes per patient; the table movement, the data acquisition and the analysis were performed automatically.

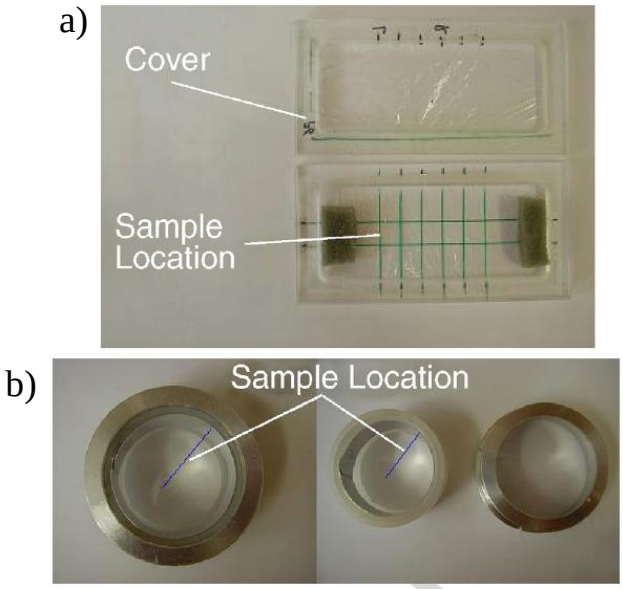

Figure 8. The needle-biopsy sample supports used with (a) the home assembled XRF system at KMC and (b) the commercial XRF systems used at SMC. In (a) wet sponges are included next to the six samples to avoid drying; in (b) each sample is secured between the two foils closing the plastic and metal cups (right), when these are tightened together (left).

The SMC XRF system was designed to scan the samples and measure the Zn content within four different segments, each 5 mm long, along the sample. For this purpose, the irradiated area was limited to 2×5 mm^2 and four different spectra were acquired and analyzed for each sample. The duration of each acquisition point lasted 20 s, with a total of 90 s per sample and typically 12 min per patient. The resulting precision was 15% to 5% for Zn levels of 50 to 200 ppm, respectively.

The clinical protocols were identical in both medical centers. The fresh needle-biopsy tissue cores were placed on their respective supports immediately after extraction, and introduced into the XRF system within minutes. Following the Zn measurement, the rectal-side edge of all samples was

marked with a black tissue-ink (Black India, No 4418, Item # 44204 by Stanford, USA) and they were stored in Formaldehyde, in separate tubes; track was kept of the extraction prostate site. The samples were then processed in the routine way at the pathology institutes: embedding in paraffin wax, slicing into 4 mm thick slices, and staining with hematoxylin and eosin. The slides were examined by one pathologist in each MC to provide the diagnosis including Gleason score, and the %gland, namely the fraction of surface occupied by the glandular tissue. At SMC this analysis was done in the four, 5 mm long segments along the core, to match the four-segment Zn measurement. The diagnosis type were: PCa (adenocarcinoma), benign prostatic hyperplasia (BPH), prostatic intraepithelial neoplasia (PIN), atypical small acinar proliferation (ASAP), or granulomatous inflammation (GRAN) (Humphrey 2003; Sauter & Cancer 2004).

The present mode of analysis provided three levels of data: a segment Zn concentration and its corresponding histological classification; a core Zn concentration and its corresponding diagnosis and a Patient-Average Zn concentration and its corresponding diagnosis. (The Patient-Average Zn is the average of measured Zn-concentration values over the entire volume of the extracted tissue per patient). A patient is defined as PCa one if any of his biopsy cores was diagnosed as PCa. A core or a segment is defined as PCa only if the diagnosis of that core or segment is PCa. All other diagnoses otherwise specified, will be referred to as Non-Cancer. This approach allowed defining three distinguished levels in the data analysis: per patient, per core, and per segment. Other relevant patient data from his medical files, such as PSA, age, Zn-rich nutrition supplements, prostate size, etc., has also been collected. The data analysis included correlation of different variables (e.g., Zn concentration) with the diagnosis, PSA, %gland, and other parameters from the patient's files.

3.1.1 Absolute Zn content and calibration standards

The analytical goal of the proposed quantitative XRF analysis was the determination of absolute Zn concentration in the needle-biopsy samples. The method is based on the assumption that the amount of Zn in the irradiated sample is proportional to the net intensity of the Zn-K_α line, $I(Zn)_{sample}$; the latter is obtained from the X-ray spectra by integrating the intensity under the peak and subtracting the background (see Zn-K_α peak in figure 9).

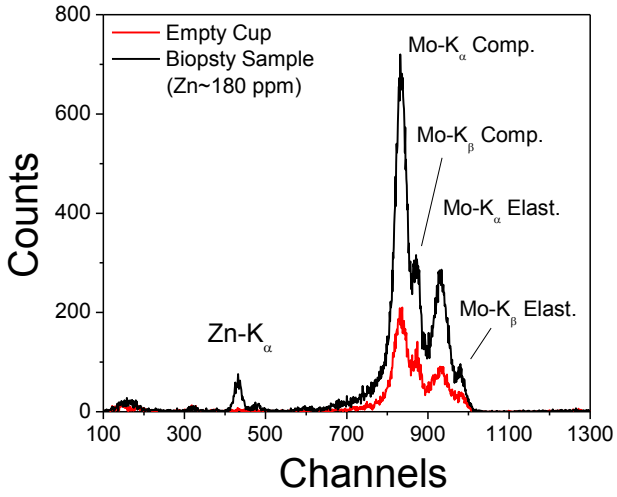

Figure 9. Examples of X-ray spectra measured at SMC from biopsy samples containing 180 ppm of Zn (black line) and from an empty sample-cup (red line).

The mass of the irradiated sample is unknown and could not be directly measured. However, since the amount of incoherent scattered radiation is proportional to the amount of irradiated material, the Compton-scattering intensity, I(Cs), obtained from the same X-ray spectrum by integrating the intensity under the Compton Mo-K_α peak, has been used instead (see Mo-K_α peak in figure 9). From this quantity we subtracted the contribution $I(Cs)_{empty}$ from the empty table or empty cup (typically amounting to less than 30% of I(Cs)), and calculated the net scattered radiation intensity due to the irradiated tissue.

$$I(Cs)_{sample} = I(Cs) - I(Cs)_{empty} \tag{3.1}$$

The relation between $I(Cs)_{sample}$ and the actual sample weight was derived from calibration standards made for this purpose.

The calibration standard was a sample having a known Zn_{st}(ppm) concentration value and designed to have a geometry and composition similar to that of a tissue sample. A measurement of the calibration standard yielded the respective $I(Zn)_{st}$ and $I(Cs)_{st}$ intensities (the latter is the value after correction for the empty table or cup), from which the calibration coefficient K was calculated:

$$K = \frac{I(Cs)_{st} \times Zn_{st}(ppm)}{I(Zn)_{st}} \tag{3.2}$$

The Zn concentration in the sample is given by:

$$Zn_{sample}(ppm) = K \times \frac{I(Zn)_{sample}}{I(Cs)_{sample}} \tag{3.3}$$

The calibration coefficient K was determined from measurements performed with various standard samples. It is most important for the standard sample to have a similar composition to the

tissue, because both the self-absorption effect and the Compton scattering are very strongly dependent on the composition. Most notably the observed spectrum originating from the specimen strongly depends also on the irradiated shape and size. Standards made of tissue-equivalent (TE) material of similar dimensions to those of the tissue samples have been accurately prepared. We have used samples extracted with a needle-biopsy instrument, from a hardboiled egg-white substance, previously loaded with a known amount of Zn. Only very short measurements could be performed on the egg samples, which tended to dry rapidly.

A more practical standard sample was made of a 0.5 mm inner diameter and ~ 0.25 mm thick wall polyethylene tube, filled with TE solution of known Zn concentration (see section 6.1.5 for details on chemical composition of TE solution used for standards preparation). In this case the $I(Cs)_{empty}$ was measured with an empty tube, to account for the tube wall contribution to the Compton peak, and the wall attenuation correction was measured independently from the X-ray fluorescence of a thin Cu wire placed inside this plastic tube. Another very convenient standard sample was made of Vaseline loaded with a known Zn concentration, and placed on the sample holder foil with a syringe to obtain the correct size and shape. Sandwiched between two foils, this standard was stable over many months; it is routinely used to check the system calibration stability, together with a thin Cu wire used to verify the energy calibration stability. The calibration factor K was derived from the average results of all calibration measurements. Another stable standard was produced from a 0.5 mm thick rectangular Lucite bar, on which a drop of Zn-loaded varnish was deposited; it was used to inter-calibrate both XRF systems, ensuring that absolute Zn concentration values were consistent in both sets of data.

3.2 Results

KMC belongs to the largest medical-insurance organization in Israel, treating mainly its own insured patients; SMC is a government institution, treating patients from all medical insurance organizations in the country. We expected to observe differences in the results due to distinct differences in the patient selection strategy, resulting for example from examination-cost considerations. Furthermore, the tissue classification was carried out by two different pathologists and may differ due to the subjective aspect of this task. We therefore analyzed the two data bodies separately, and identified the data source on each graph or table. Tab. I summarizes the total patient statistics while Tab. II summarizes the total tissue-segments statistics (SMC); in parentheses the number of patients consuming Zn-rich dietary supplements.

Table 1. Total Patient Statistics

Medical Center	Total no. of Patients	Non-Cancerous Diagnosis	PCa Diagnosis
Sheba (SMC)	272 (21)	203 (17)	69 (4)
Kaplan (KMC)	326	237	89

Table 2. Total Statistics of 1 mm^3 Tissue Segments (SMC)

Total no. of Segments	Non-Cancerous Segment	Cancerous Segments
8,992	8,232 (635)	699 (33)

3.2.1 Age, Size and PSA Distribution

A known risk factor for prostate cancer is age. According to (Bloom et al. 2006) the PCa risk increases significantly after the age of 40 in black men and men who have a close relative with prostate cancer above age of 50 in white men who have no family history of the disease. This general trend is also reflected by our data depicted in figure 10; it shows the age distribution (fraction of cases) of Non-Cancer and PCa patients in the two MCs. The risk of PCa linearly increases with age; about two-thirds of all prostate cancers are diagnosed in men above 65 and about 50% of the tested patients, above 75, had a confirmed PCa diagnosis.

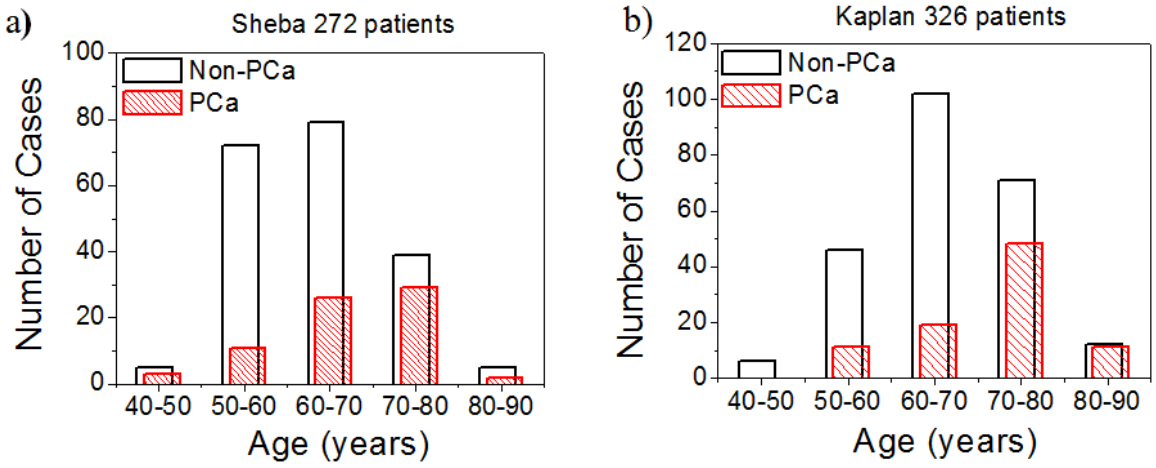

Figure 10. Age distributions of Non-Cancer and PCa diagnosed patients in (a) SMC and (b) KMC.

The risk of PCa linearly increases with the age and about two-thirds of all prostate cancers are diagnosed in men age 65 and older and about 50% of the tested patients, older then 75, has a confirmed PCa diagnosis.

Since prostate volume may influence the operative approach in patients with prostatism, its estimation is of concern to urologists and it is considered as a preoperative prognostic factor (Freedland et al. 2005). The impact of prostate volume on PCa probability and the inclusion of prostate volume in the multivariate linear model for reduction of unnecessary biopsies have also been proven by many reports - see for example (Catalona et al. 2000). The most common approach for the prostate volume (P_{Volume}) determination, also used in our clinical trial, is by TRUS using prolate ellipse volume calculation:

$$P_{Volume} = (\text{Height} \times \text{length} \times \text{Width}) \times \frac{\pi}{6} \qquad (3.4)$$

Transverse diameter (width) is defined as the maximal transverse diameter at mid-gland level, while longitudinal diameter (length) is defined as the distance from the proximal external sphincter to the urinary bladder. Anteroposterior diameter (height) may be measured in two planes-axial and sagittal (Littrup et al. 1991).

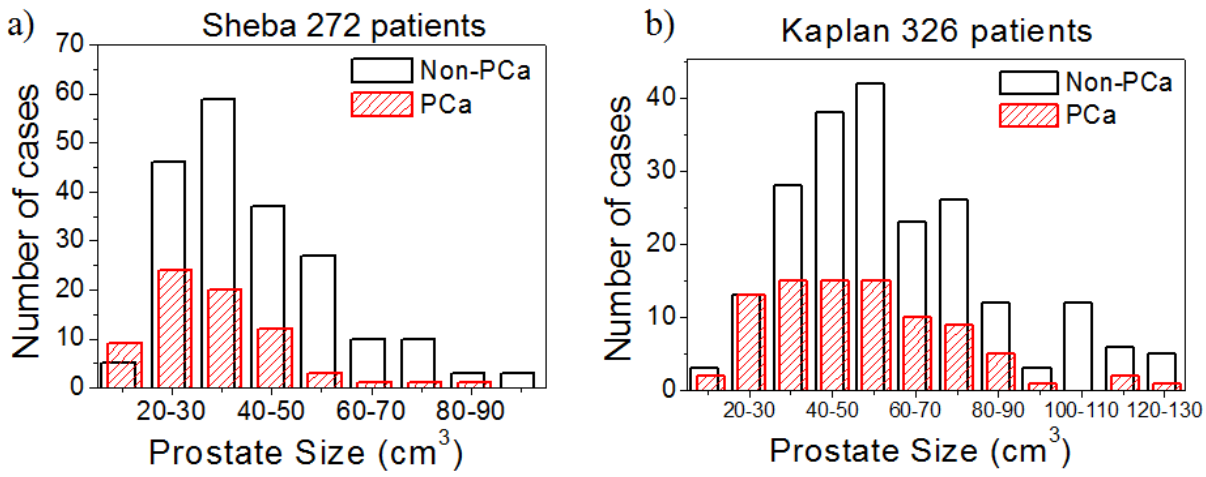

Figure 11. Prostate-volume distributions of Non-Cancer and PCa diagnosed patients in (a) SMC and (b) KMC.

Figure 11 depicts the prostate-volume distributions (fraction of cases) of Non-Cancer and PCa cases in both MCs; the distribution in KMC is broader, probably due to a larger number of examined patients with symptomatic BPH diseases. In both MCs the mean volume for the PCa group (33 and 52 cm^3 SMC and KMC, respectively) is smaller than that of the Non-Cancer group (42 and 60 cm^3 SMC and KMC, respectively). Nevertheless, from our data analysis, the shift in the

respective distributions' mean values is small compared to their widths and they remain overlapped, even when age and size are combined.

The PSA distributions for the same patient groups, together with normal curves fitting the data up to PSA = 15 ng/ml, are presented in, showing very similar mean and width values for PCa and Non-Cancer in both medical centers.

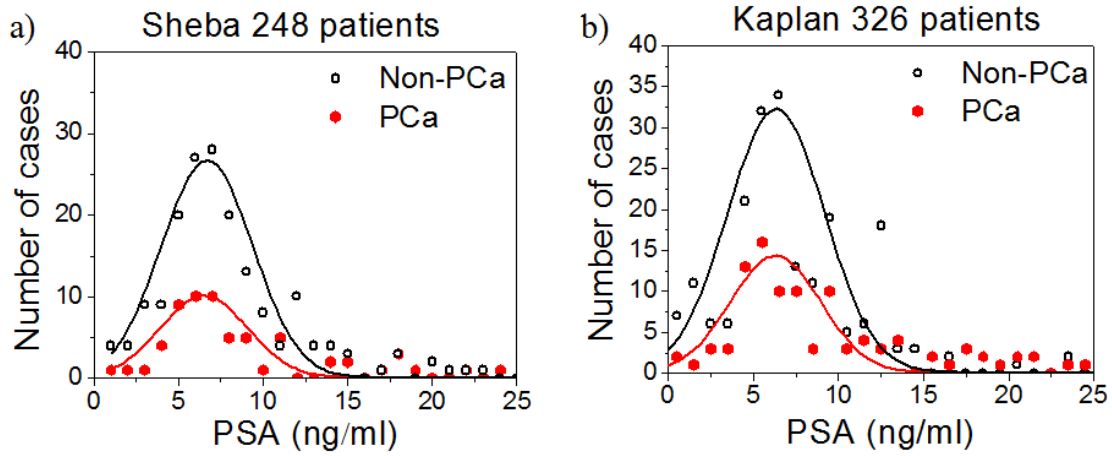

Figure 12. PSA distributions and normal distributions fitting the data up to PSA = 15 ng/ml, for Non-Cancer and PCa diagnosed patients in (a) KMC and (b) SMC. The fitted mean and width values for Non-Cancer and PCa groups, in each of the MCs, coincide within the fit error.

More interestingly, figure 13 presents the same data as fraction-of-PCa cases versus PSA: this fraction is rather constant, of about 25%; that the large errors for PSA levels above 15 ng/ml are due to insufficient statistics, preventing any significant conclusion.

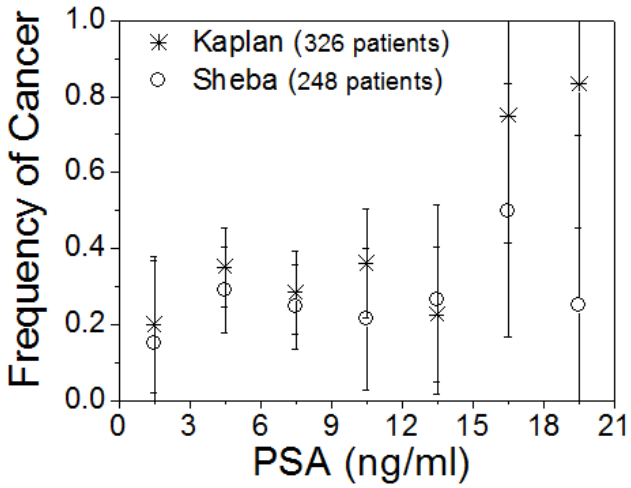

Figure 13. The data of figure 12 presented as fraction of PCa cases vs. PSA. This fraction is rather constant, at about 25% (above PSA = 15 ng/ml there is no sufficient statistics to draw any significant conclusion).

Figure 12 and figure 13 together are consistent with the conclusion that PSA has no diagnostic value for those patients referred to the biopsy clinics. In addition, using PSA derivatives, namely PSA normalized to the prostate volume (PSA density) and to patient's age, actually reflects the sensitivity of the diagnosis to age and size but not to PSA. In spite of this, PSA density has been shown to be directly related to age, because of three principal reasons: first, PSA levels are higher in older men with larger prostate glands. Second, as men age, the physiological barriers that keep PSA in the prostatic ductal system may also become more permeable and allow more PSA to enter the general circulation. Increased PSA levels with age may also be influenced by prostatic ischemia or infarction, chronic sub-clinical prostatitis and prostatic intraepithelial neoplasia. Finally, a large prostate volume is likely to increase the percentage of free PSA, and therefore these variables may not be totally independent (Stenman et al. 1998).

The effect of patient age on the average Zn concentration in the prostate is depicted in figure 14, based on 204 non-cancer patients at SMC. For each age group Zn has a normal distribution with mean of 110 and standard deviation of about 60 ppm. There is no evident age effect.

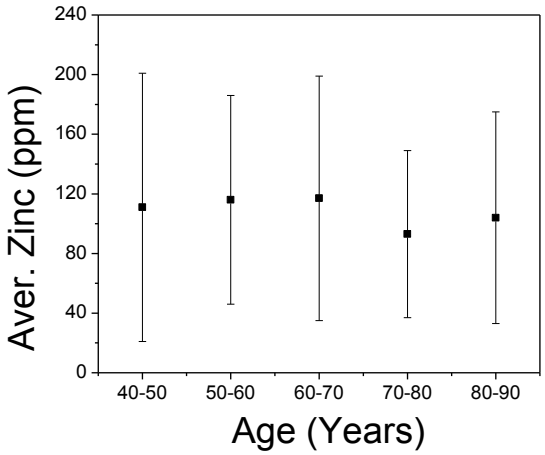

Figure 14. The average Zn value per patient as function of age, for 203 non-cancer patients at SMC.

3.2.2 Zn-rich nutrition effects on Zn concentration

One of the main concerns regarding the validity of the clinical data was a possible falsely-elevated Zn concentration resulting of Zn-supplements consumption (e.g. multi-vitamins - see Tab. 1). The effect was studied at SMC only, both on the segment and on the patient-average data levels.

Figure 15 presents the patient-average Zn concentration for PCa- and Non-Cancer diagnosed patients, from SMC, with and without Zn supplement in their diet. (see Tab. 1).

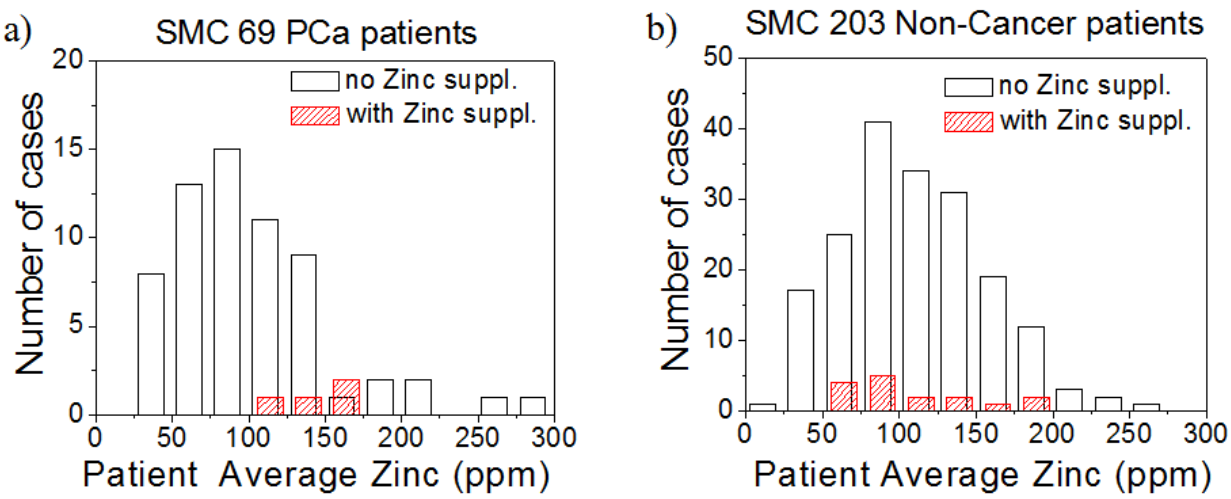

Figure 15. Patient-Average Zn distribution and the effect of Zn-rich diet for PCa (a) and Non-Cancer (b) diagnosed patients at SMC. See text for interpretation.

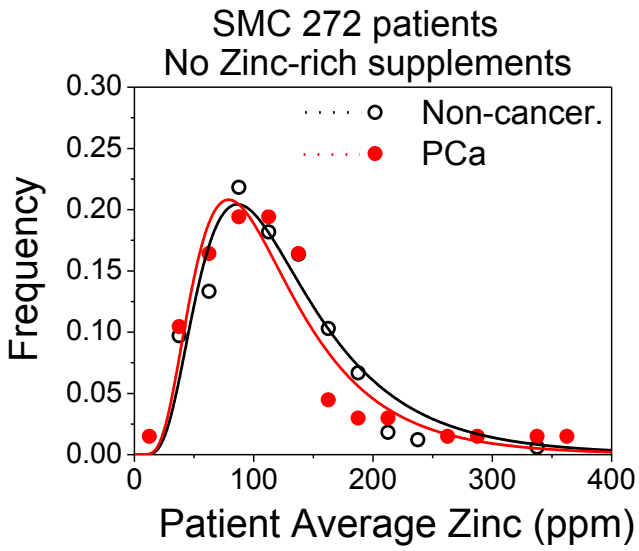

Figure 16. Patient-Average Zn distributions in the absence of Zn-rich diet for Non-cancer and PCa diagnosis (SMC); the distributions are identical for both diagnoses (c).

Among the 68 PCa-diagnosed patients only 4 persons declared practicing Zn-rich diet; seemingly, their average Zn values are significantly different from the others, but the poor statistics does not permit evaluation. Statistical Kolmogorov-Smirnov (K-S) test (Mood et al. 1974), with confidence 5%, confirms that the two Non-Cancer populations and the PCa "no-Zn-supplement" population may all be considered identical. In other words, in the absence of Zn-rich diet, the

patient-average Zn has identical distributions for both diagnoses (figure 16). In the presence of Zn-rich diet, the results are non-conclusive.

The situation seems clearer when studying the Zn-rich nutrition effect in tissue segments. Figure 17 shows Zn-concentration distributions (Fraction of cases) measured within a 5 mm long biopsy segments (~1 mm^3 of biopsy tissue), for PCa- and Non-cancer tissue segments, for patients with and without Zn-rich diet. The data was fitted with lognormal curve[1], and analyzed with K-S test to compare the distributions of different ensembles. The Zn-rich diet does not affect the distribution's width but it does shift its mean. The shift is negative (from 109 to 103 ppm) for Non-Cancer tissue segments, and statistically significant; it is more pronounced and positive (from 56 to 81 ppm), and statistically significant, in the PCa tissue segments. More importantly, the Non-Cancer "no-Zn-supplement" distribution and the PCa with Zn supplement distribution are not statistically different, clearly demonstrating the obscuring effect of Zn-rich dietary components.

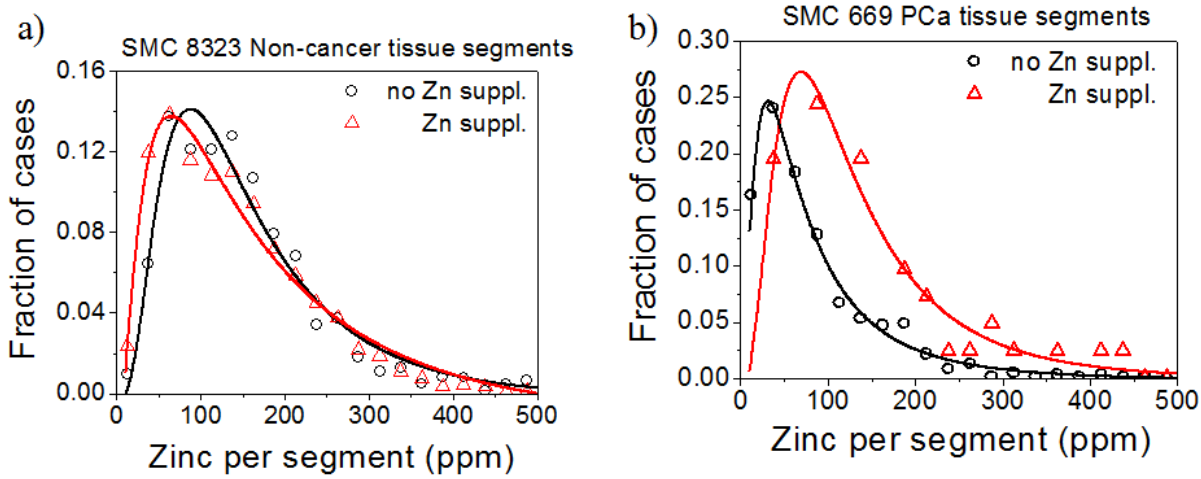

Figure 17. The effect of Zn-rich diet on Zn concentration, measured at SMC in 1mm^3 tissue segments, classified as (a) Non-Cancer and (b) PCa. The data is fitted with log-normal distributions.

[1] the variable's logarithm is normally distributed.

$$f(x;\mu,\sigma) = \frac{1}{x\,\sigma\sqrt{2\pi}} \exp\left[-\frac{(\ln(x)-\mu)^2}{2\,\sigma^2}\right]$$

for $x > 0$, where μ and σ are the mean and standard deviation of the variable's logarithm.

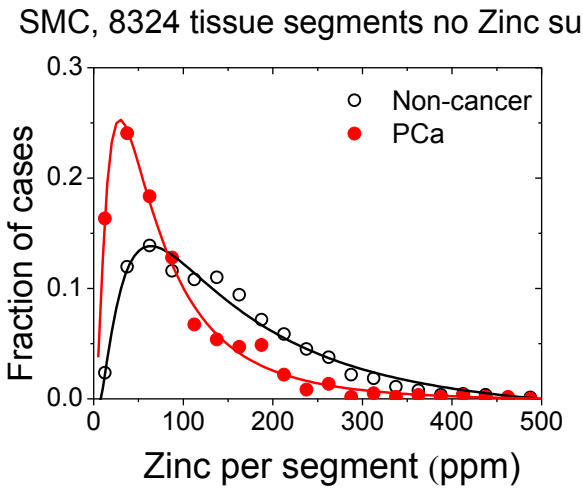

Figure 18. The Zn distributions of Non-Cancer and PCa diagnosed tissue segments, measured at SMC in the absence of Zn-rich diet, fitted with lognormal curves. They are shifted by a factor of 1.44 and are statistically significantly different, with a clear potential diagnostic value.

On the other hand, and in opposite to the Patient-Average Zn concentration distributions, the Local Zn concentration (figure 18) in the absence of Zn-rich diet has distinctly different distributions for tissue segments classified as PCa or Non-Cancer, with their mean (μ) shifted by a factor of 1.44 and their respective standard deviation (σ) by factor 0.96. This shift ratio is smaller than the one reported in the 20-years old literature (Lahtonen 1985; Habib et al. 1979; V. Zaichick et al. 1997) that comprised patients having advanced disease. Nevertheless, the shift between the two distributions represents a confirmed diagnostic value attributed to the Zn concentration measured in 1 mm^3 segments. It is also evident that the diagnostic value is degraded in patients subject to Zn-rich diet. Based on these findings, all the results described further on exclude patients consuming Zn-rich nutrition supplements. The effect of this exclusion on the statistics is negligible.

3.2.3 Zn Concentration in PCa patients - correlation with Gleason Score

In the following (figure 19-figure 22) we present the Zn-concentration in PCa-diagnosed patients at SMC (confirmed to lack Zn-rich diet), and its correlation with the Gleason Score. The correlation is presented for Patient-Average, segment and core data levels. In almost all cases the Gleason score values assigned to all the malignant segments of a given patient were identical and equal to the Gleason score diagnosis assigned to the patient. Therefore, in the following we also classified the Non-Cancer tissue according to the Gleason score of the patient. Tab. 3 provides the

information on PCa-patients number per each Gleason score category (64 in total); the conventional nomenclature has been employed, which defines the well-, moderately- and poorly-differentiated categories corresponding to Gleason score values of 5-6, 7 and 8-9. 6 patients diagnosed for minimal volume carcinoma (MVC) are considered separately. Tab. 3 also summarizes the statistics of tissue-cores and tissue-segments classified in the same way.

Table 3. The number of PCa-diagnosed patients and of cancerous and Non-Cancer tissue cores and tissue segments, classified according to the various Gleason score categories. Minimal volume carcinoma (MVC) was considered separately. Data from SMC.

	Min. volume carcinoma	Well differentiated Gleason 5-6	Moderately differentiated Gleason 7	Poorly differentiated Gleason 8-9
PCa patients	7	36	22	11
Non-Cancer cores	38	192	86	14
PCa cores	55	84	99	55
Non-Cancer segments	180	896	462	100
PCa segments	26	177	246	166

Figure 19 shows the patient-average Zn concentration distribution (Fraction of cases) for the cancer patients according to their Gleason score; the non-cancer patients' distribution is given for comparison. The distributions were analyzed by the K-S test and it was confirmed that, excluding the low-statistics group of Gleason 8-9, all the other distributions are statistically equivalent. The same conclusion holds for the data from KMC.

Figure 20 shows Zn concentrations of all (cancerous and non-cancerous) biopsy cores (4 mm^3 tissue), from PCa-diagnosed patients, plotted as fraction of cases and fitted with lognormal functions. The shift in the geometrical mean is small (10% between the categories) for the Non-Cancer cores, but very pronounced (factors 1.7 and 2.7) for the PCa cores. In accordance with the shift of the mean, the distribution width becomes smaller with increasing Gleason score.

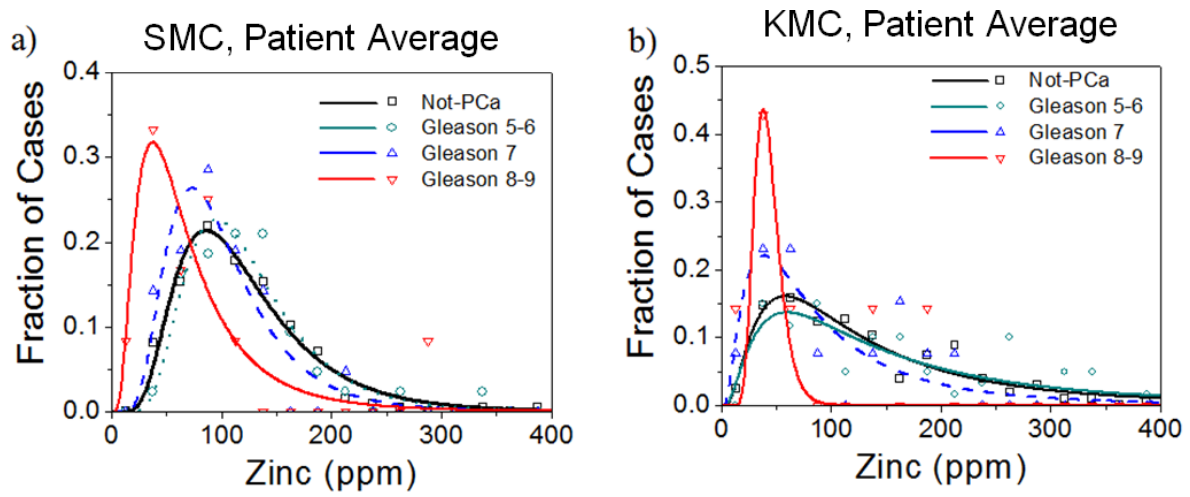

Figure 19. Patient-Average Zn concentration distributions (fraction of cases), and their lognormal fits, in Non-Cancer and in PCa diagnosed patients at SMC and KMC, according to their Gleason score.

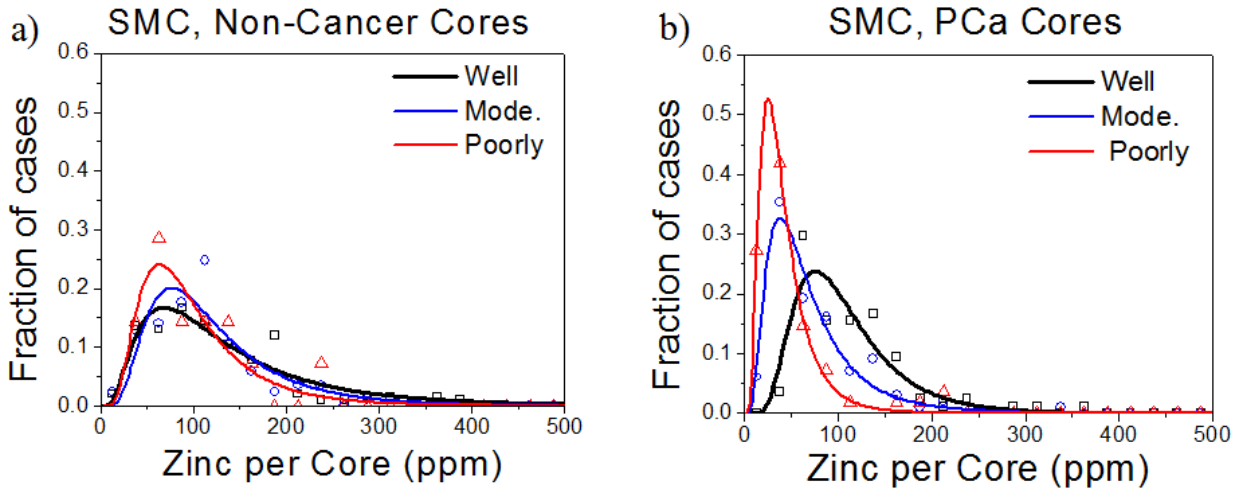

Figure 20. Zn concentration distributions (fraction of cases), and their lognormal fits, in Non-Cancer (a) and cancerous (b) tissue cores, of PCa diagnosed patients at SMC. In the PCa tissue cores a pronounced systematic decrease (factors 2 and 3) with increasing Gleason score is evident. A slight (10%) decrease is observed in the Non-Cancer tissue surrounding the lesion.

A K-S test (run at confidence level 5%) on the data of SMC depicted in figure 20 confirmed that the two Zn-value groups, of the well differentiated PCa and of Non-Cancer, are statistically identical populations. But the moderately and poorly differentiated PCa Zn-value groups are statistically different from the Non-Cancer group.

Figure 21 shows Zn concentration distributions (plotted as fraction of cases) of all (non-cancerous and cancerous) tissue segments (1 mm^3) from PCa diagnosed patients at SMC, fitted with

lognormal functions, for the Non-Cancer and the PCa tissue segments, as function of Gleason score category.

A very pronounced systematic shift to lower Zn values with increasing Gleason score is observed for the cancerous tissue, while a much more moderate shift exists in the Non-Cancer component. (The distribution in Non-Cancer tissue segments from Gleason score 5-6 patients is practically identical to that found in non-cancer patients). As a result, **the contrast in the Zn levels between cancer and non-cancer is increasing with Gleason score.**

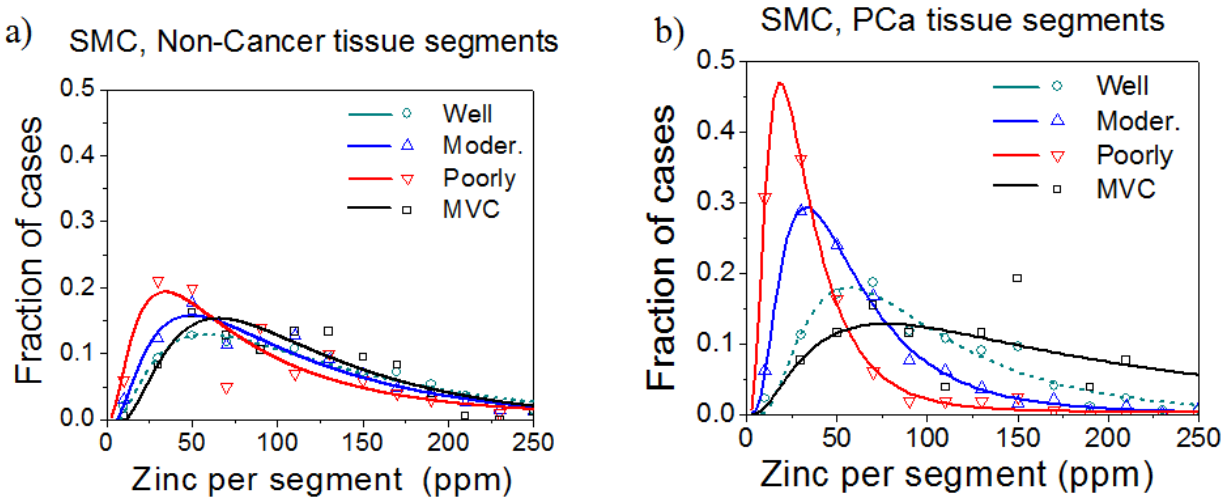

Figure 21. Zn concentration distributions (fraction of cases) in Non-Cancer (a) and cancerous (b) tissue segments, in PCa diagnosed patients at SMC (see Tab.3). The Zn in PCa tissue segments shows a pronounced systematic decrease with increasing Gleason score. A more moderate decrease is observed in the Non-Cancer tissue surrounding the lesion.

This is demonstrated in figure 22(a-c), showing together the Zn distributions for Non-Cancer and PCa tissue segments of PCa patients, and their respective fits, for each Gleason score category. While for low Gleason scores (well differentiated cancer) the peaks of Non-Cancer and cancer tissue are shifted by only 30%, and their widths are very similar, the separation becomes more pronounced with increasing Gleason scores; for high Gleason scores (poorly differentiated cancer) the distributions mean values (μ) differ by a factor of 2.6, and their respective standard deviation (σ) by a factor 0.8.

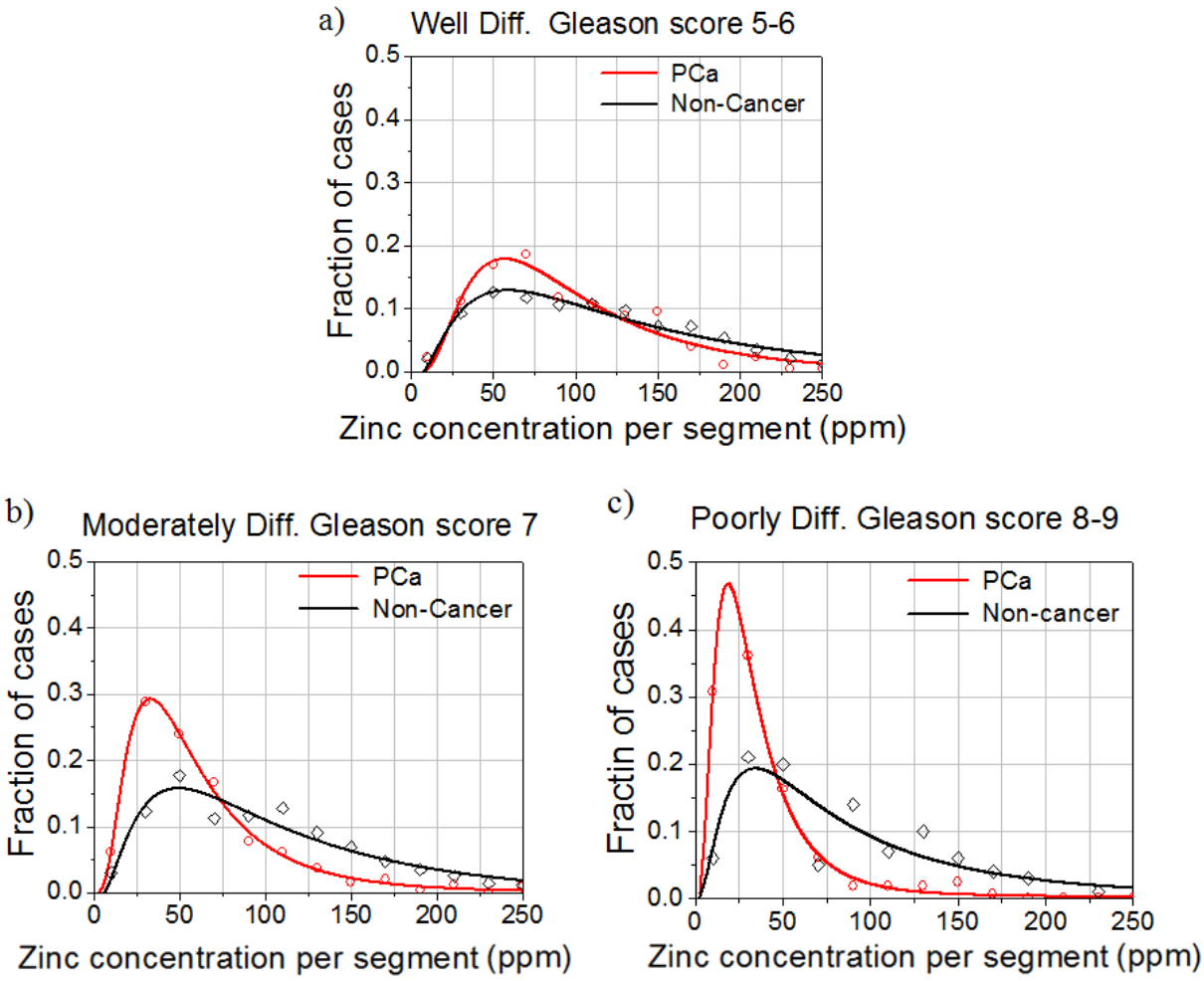

Figure 22. The contrast in Zn content between Non-Cancer and cancerous tissue-segments of PCa-patients, according to the level of cancer cells' differentiation: well differentiated (a), moderately differentiated (b) and poorly differentiated (c).

So far all the Zn data of tissue-segments scored as 5-6, 7 and 8-10 were grouped together and were labelled as 'well-', 'moderately-' and 'poorly-' differentiated, respectively. The same experimental Zn-concentration may be re-analysed and the Zn-content data may be grouped according to a more refined Gleason grade classification (figure 23a), namely according to the separate classification of the primary and secondary histological patterns: 3+3, 3+4, 4+3, 4+4, 4+5 and 5+4. This classification complies better to current medical approaches - combinations of grades 1 and 2, are excluded since they were not diagnosed in needle-biopsy specimens, as well as the combination 5+5, due to a limited number of patients with such assessed pathological condition. Figure 23a also shows the frequency distributions of Zn concentration measured in the non-PCa tissue component. All the Zn distributions in figure 23a appear to be strongly asymmetric, a feature usually attributed to frequency distribution of non-essential trace elements (Liebscher & H. Smith

1968). The asymmetry is statistically more significant at higher Gleason grades, with a sizable increase of the distribution skewness towards lower Zn values. All the frequency distributions were fitted with lognormal functions.

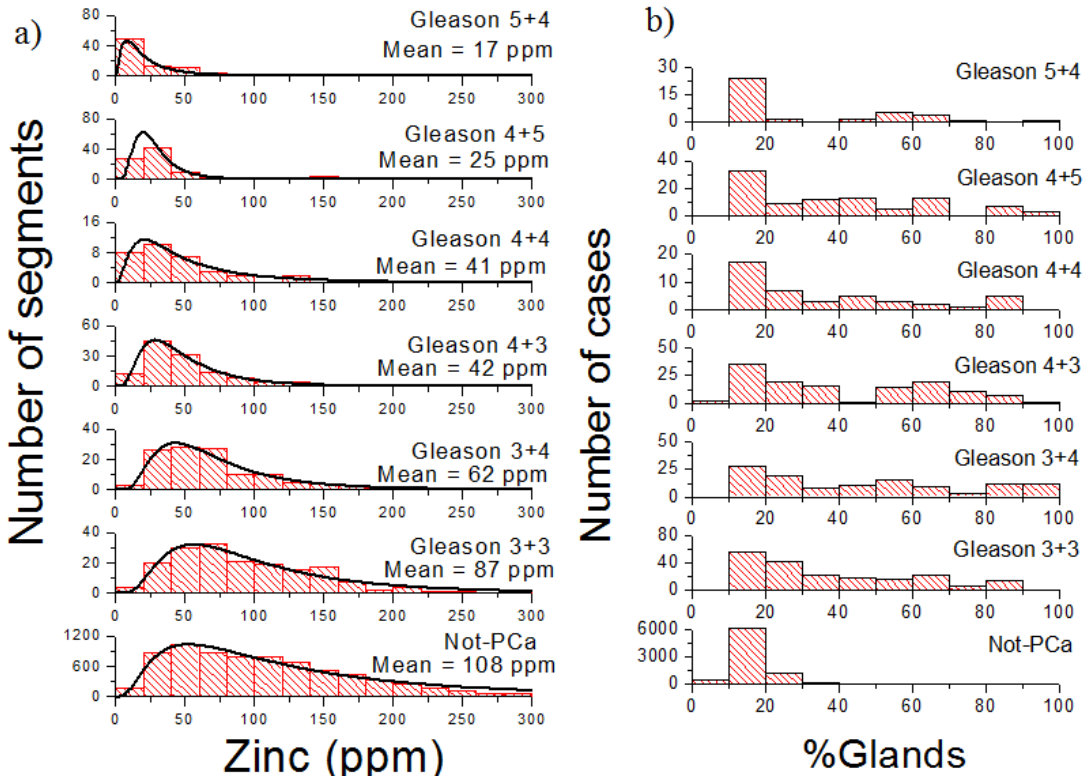

Figure 23. a) Distribution of Zn concentration measured in 1mm^3 prostate-tissue segments, grouped according to the diagnosis and to the assigned Gleason grade. The distributions are fitted with lognormal function; the mean Zn value for each distribution is provided. b) %Gland distributions grouped according to the same criteria.

Because the Zn distributions of figure 23a are based on information accumulated from several PCa patients in each Gleason grade category (31 patients with Gleason grade 3+3, 11 patients with Gleason grade 3+4, 13 patients with Gleason grade 4+3, 2 patients with Gleason grade 4+4, 5 patients with Gleason grade 4+5 and 3 patients with Gleason grade 5+4), they represent a poorer Zn contrast than we expect in a single patient: they contain effects of intra-person variations, which tend to broaden each distribution, as well as effects of person normalization, which may shift the Zn distributions of benign and cancerous tissue in a correlated way. Both effects tend to reduce the contrast between cancerous and non-cancer tissue when the data of several patients are combined. Unfortunately, this is the only reliable data available at the moment. The current work may thus be considered as a ‘worst case scenario’. Further clinical studies are currently designed to provide data from individual PCa patients; they will permit better evaluation in the future.

Finally, figure 23b depicts histograms of the estimated total glandular component (%Gland) for the same groups of tissue segments. In non-cancerous tissue segments the %Gland is sharply concentrated at a mean value of about 15%, while in cancerous tissue the distribution is broad, with a sizeable presence of higher values of %Glands, indicating a sort of gland proliferation effect in the case of PCa tissue.

3.2.4 Most Recurrent Location of PCa Development

As well documented in literature, see for example (Theodorescu 2009), PCa normally develops within the peripheral zone of the prostate gland; according to the present clinical investigation, with only 8 biopsy needles per patient, around 80% of the patients have at least one assessed cancerous needle-biopsy section (out of 8) within a depth range of 0.3-0.75 cm, while around 95% of them have at least one assessed cancerous needle-biopsy section within a depth range of 0.3-1.2 cm (figure 24).

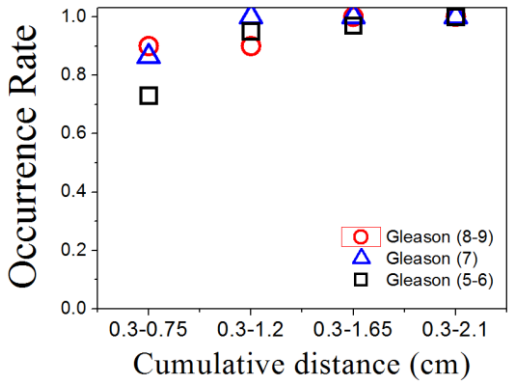

Figure 24. Cancer occurrence rate as function of the cumulative distance from the rectal wall, for different Gleason grades. More than 90% of the tumors detected by the needle biopsy (8 needles per patient) are present within a tissue layer less than 10 mm thick at the back of the gland. A PCa patient has at least one PCa segment within the specific depth range (depth includes 0.3 cm rectal wall thickness).

The PCa occurrence to depth relationship depends actually on the cancer aggressiveness; generally, the more advanced is the cancer the larger is its volume and therefore higher is the probability that it is extended at different depths.

Note that the PCa-occurrence vs. depth results, though very encouraging with relation to a prostatic-probe development, were limited by the small number of samples over the gland; therefore they naturally provide only a lower limit. *In-vivo* Zn-concentration mapping in the posterior part of

the peripheral zone, with a large number of sampling points is expected to effectively detect malignancies within a depth of a few millimeters behind the rectal wall.

4. Monte Carlo simulations of PCa detection and grading by XRF imaging

The present chapter deals with the analysis of prostatic-Zn-concentration images; the goal being the evaluation of the clinically-relevant information of such images. Indeed, though the Gleason-related Zn-distributions show a clear systematic trend (see figure 23a), of increasing Zn depletion with increasing Gleason grade, and their distributions are statistically non-identical, their corresponding variances are rather large and they are significantly overlapping. It implies that a single Zn-value measurement at a single point (e.g. ~1 mm^3 tissue volume) within the lesion, is not sufficient for providing reliable diagnostic data. However, sampling of the Zn-distribution, achieved by mapping the lesion over many pixels, should be adequate for diagnosis purposes.

In the absence of experimental images, synthetic ones were produced from our clinically measured Zn-concentration distributions in histologically-certified benign and cancerous tissue needle-biopsy segments, classified by their lesion grades (Paragraph 3). Image analysis, based on a combination of standard image processing and segmentation tools, was developed and optimized for this particular application. The information on "lowest Zn-value" obtained from the image analysis was then translated to clinical relevance such as tumor presence, location, size and grade.

4.1 Material and methods

4.1.1 Zn-maps generation

Two-dimensional Zn-concentration maps, representing 1 mm thick prostatic tissue layers, of area 3×3 cm^2, with or without cancerous lesion randomly located within it, were generated using Monte Carlo tools. The input probability distribution functions were the experimental data of figure 23a. The maps were defined as matrices of a given pixel number, namely 10×10, 15×15, 20×20 and 30×30 pixels, and they were generated either from the non-cancer data or from both non-cancer and cancer data, assuming a lesion of certain Gleason grade occupying a certain group of pixels randomly located on the map. Each pixel's content was chosen independently, at random, from the corresponding lognormal input distributions by an appropriate random-number generator (figure 25). Optionally, the pixel content could be modified at this point to include fluctuations originating from counting statistics, namely from the fact that the matrix is generated by a real detector (counting statistics).

In the next step, the pixels' content was quantized into an 8-bit grey scale by a process of color quantization, with the grey-scale brightness ranging from 0 to 255; this created a concentration scale of 2 ppm Zn-concentration steps, with the full scale spanning the range of 0 to 510 ppm Zn. The map-generation algorithm and the succeeding image analysis were written with MatLab 7.0 (R14) software tools (The MathWorks Inc., Natick, MA, USA).

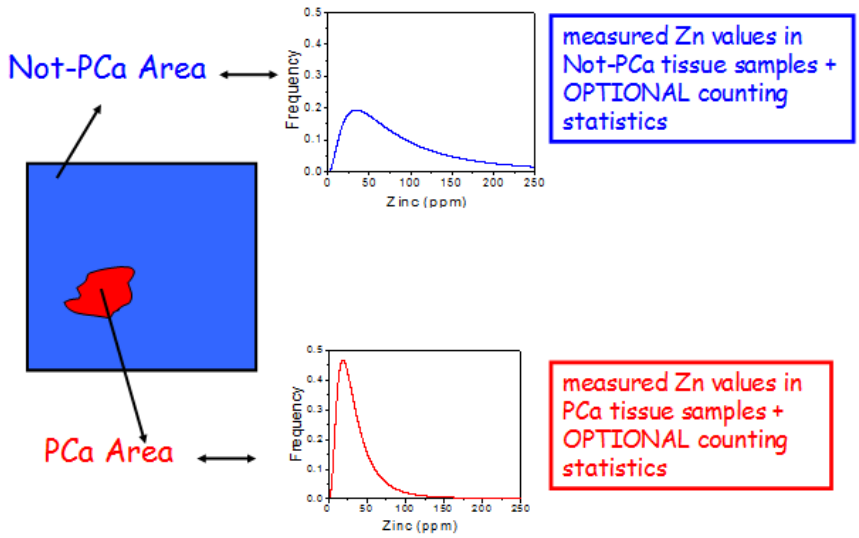

Figure 25. Monte Carlo simulated Zn maps representing benign tissue surrounding a cancer lesion randomly located within it. The experimental Zn-frequency distributions, characteristic of different pathological classifications, were used as input. Optionally, counting-statistics effects could be introduced.

4.1.2 Image analysis

The analysis of the 8-bit images consisted of the following steps:

- Denoising
- Detection and Localization
- Classification
- Grading and staging

In the first step, the image was processed with a median filter, which led to high degree of noise reduction (Denoising) but preserved the edges of the image features. The dimension of the median filter block was optimized by searching for the best lesion detection and best definition of the geometry of the detected cancer lesion. The optimal denoising was achieved with 5×5 median filter.

In the second step we were interested in detection and localization of local Zn-depleted features in the image. This was performed by an image-segmentation process, based on cluster-analysis. Image-segmentation is a low-level image-processing task that aims at partitioning an image into multiple chromatically-homogeneous regions. Various approaches exist to segment images according to different criteria (thresholding, clustering, Markov random fields, etc.) (Pham et al. 2000). In this work we used expectation-maximization (EM) technique (Ramos & Muge 2000). According to this method the digitized Zn-images are partitioned into N homogeneous clusters classified by their average grey-levels. EM is an unsupervised algorithm, which iteratively alternates between segmenting the image into N clusters and characterizing the properties of each cluster in terms of its grey level. The output image of the EM clustering algorithm, the segmented image, is basically a statistical description of the N clusters, providing the number of components in each cluster, the localization of the cluster components within the map, the average grey-level and related variances associated to each cluster. The cluster with the lowest grey-level value is identified as "suspected" cancer-lesion areas (Detection and Localization). The partition size N (number of clusters) was chosen by an optimization process, searching for the N value that yields the best lesion detection performance; indeed a small partition dimension may overestimate the area of the detected lesion, especially for small cancer. On the contrary, large partition dimension may underestimate the geometry of the detected cancer lesion. For the relevant matrix sizes considered in our study, and in consideration of an acceptable lower limit of detectability for the cancer area (arbitrary chosen at 5% of the total image area), the optimized number of cluster for segmentation was found to be N = 6.

Figure 26 shows an example of a Zn-concentration map of 30×30 pixels with a 6×6 pixel lesion of Gleason grade 5+4, and the results of the processing steps applied to this image. Figure 26a shows the computer-simulated map after digitization into a grey-scale image. Figure 26b illustrates the same image after denoising with 5×5 median filter. The dark pattern of Zn depletion is clearly visible and corresponds well to the assumed lesion: in both figure 26a and figure 26b, the site of the computer-simulated cancer lesion is delineated. Figure 26depicts the result of the image segmentation process. The two clusters with lowest grey-level value are shown - the black area is the lowest-Zn cluster while the grey area is the second-lowest one. According to our image analysis protocol, the two lowest-Zn clusters represent the identified Zn-depleted area in the image, namely the area identified as cancer, while the white area represents benign tissue. This completes the step of detection and localization.

The average values of the Zn distribution in the lowest Zn cluster (LC_{Zn}) is also indicated in figure 26c. This value is used for the next steps of the analysis, the classification, namely, the cluster is classified as cancerous or non-cancerous and, if classified as cancerous, it is being classified according to its cancer-aggressiveness grade (Grading). These steps are performed by a single-parameter classification test based on the LC_{Zn} values.

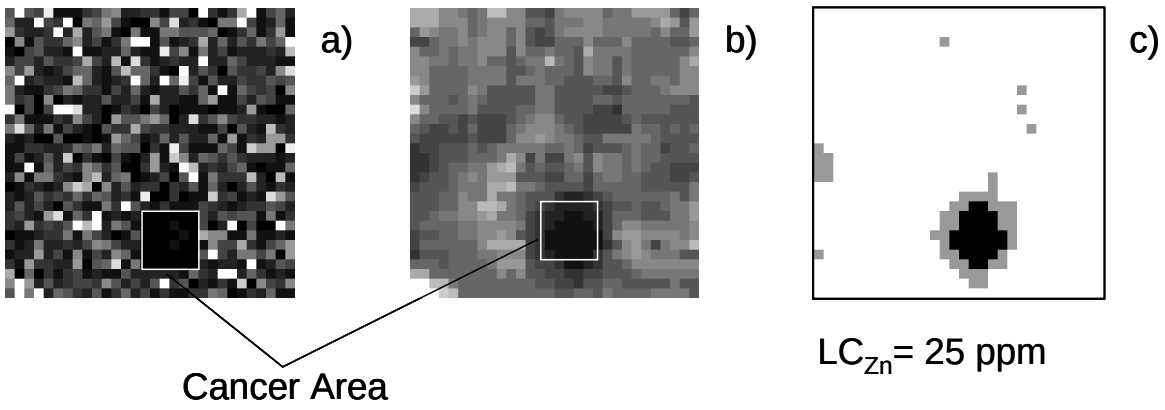

Figure 26. An example of a 30×30 pixels simulated Zn map converted into a grey-scale digital image (a). It contains a 6×6 pixels cancer lesion of high Gleason grade (5+4); (b) is the image after Median Filtering and (c) is the same image after segmentation processing, showing the two identified Lowest-Zn clusters in black and grey. LC_{Zn} is the average value of the Zn in the Lowest-Zn cluster.

4.1.3 Cancer detection and localization evaluation

The performances of the classifier test were computed and evaluated by means of Receiver Operating Characteristic (ROC) analysis, which is a way of presenting the detection quality of a binary classifier test, commonly applied to medical diagnosis problems (Fawcett 2004; Hand & Till 2001). The ROC curve is a two-dimensional graph in which a true-positive rate (sensitivity) is plotted versus the false-positive one (1-specificity), the so called ROC space, for each classifier's cut-off value. An ideal binary classifier test would yield a step-function shape (0,1) in the ROC space, representing a sensitivity of 100% (all true-positives found) and 100% specificity (no false-positives found). A realistic binary classifier test yields a monotonically rising graph, of which the quality is evaluated by the area under the curve (AUC), namely the larger the AUC the better is the classifier quality (figure 27). An AUC close to 1 corresponds to an excellent diagnostic test while an AUC of 0.5 corresponds to a completely random one.

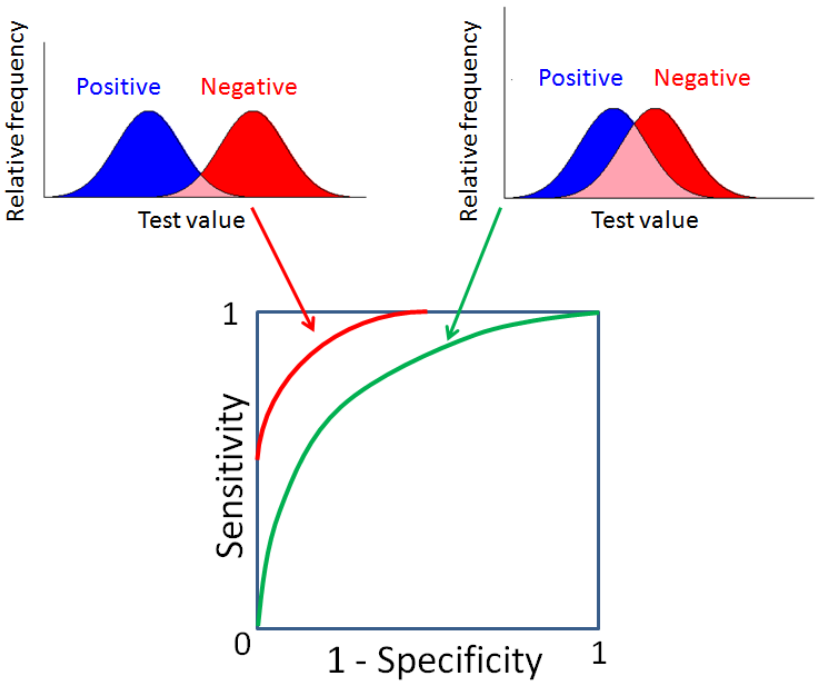

Figure 27. ROC curve is a two-dimensional graph in which a true-positive rate (sensitivity) is plotted versus the false-positive one (1-specificity): the smaller the overlap of two curves, the greater the area under the ROC curve – namely detection performance.

In order to evaluate the binary classifier based on LC_{Zn}, we calculated the ROC curves in the following way: for each set of parameters under investigation (e.g. map size, lesion size, lesion grade, etc.) we generated two sets of 10,000 synthetic maps; one set of maps representing benign tissue and the second set representing benign tissue surrounding a cancer-lesion of the specific size and Gleason grade, randomly located within the map. All the images of both classes were processed according to the steps described above, and for each of the processed images we have computed the value of the classifier LC_{Zn}; we then varied the threshold of the classifier test, LC_{Zn}, and checked automatically, for each threshold, the rate of correctly (sensitivity) and falsely (1-specificity) detected lesions, in order to construct the ROC curve. In addition, the capability of the imaging processing to localize the original simulated cancer lesion was evaluated by comparing the position of the centroid of the detected area (lowest-Zn cluster) with the true lesion location: if the true lesion position did not overlap with the centroid of the detected lesion, this is considered as a false positive; if the true lesion did overlap with the centroid of the detected lesion this is considered as a true positive.

The same process of evaluating the cancer detection and localization performances, based on LC_{Zn} and image segmentation, was repeated for different sets of maps characterized by different

image- and lesion-parameters, namely spatial resolution (total number of pixels), cancer-lesion size and Gleason grade. This approach served to delineate the relation between cancer detection performance and various image-parameters and to outline the kind of diagnostic features we might expect, such as the size of lesion detected for each Gleason grade and its confidence. It may also instruct us on the parameters of the map (e.g. number of pixels) that the probe's imaging system should provide.

4.2 Results

4.2.1 Counting Statistics and PCa Detection Quality

The simulated images and their analysis scheme described in this section provide an opportunity to study the effect of counting statistics on the diagnostic quality of the Zn-based approach.

Counting statistics is related to the radiation dose administered to the patient, which should be kept to minimum. The counting-statistics is related to random fluctuations in the measured number of Zn XRF photons in each image pixel. The fluctuations affect the image quality because they degrade the image contrast, the details of the lesion-edges and the information on the Lowest Zn value; this, in turn, affects the tumor grading and the information on the lesion dimensions. Obviously, there is a trade-off between radiation-dose and image-quality; the optimization of this parameter is crucial for the application of the Zn-based diagnostic approach and for the realization of an *in-vivo* trans-rectal prostatic-Zn probe.

In order to quantitatively evaluate the effects of counting statistics from fluctuations in the XRF photon detection, we performed the image simulation and analysis while varying the relative weight of the fluctuations. We simulated both 15×15 and 30×30 pixels images. Two sets, of 1000 images each, with and without cancer lesions, were computer-simulated using a first random number generator, as described above. Then we have assumed a given sensitivity for the experimental system, namely a given counts/ppm/pixel. Each pixel's content was converted into number-of-counts, by multiplying the corresponding Zn-value by the specified sensitivity. The effects of the sensitivity on cancer area detectability is illustrated in figure 28: the better is the sensitivity the more detailed is the detected Zn distribution, and thus the more precise is the cancer area detection and the calculation of LC_{Zn}. After converting the Zn content to a number of counts,

the statistical fluctuations noise-effect was added namely, a Poisson-distributed noise was folded, with the help of a second random generator, into the simulated number of counts in each pixel. The modified matrices, resulting from this step, were processed as described in section 4.1.

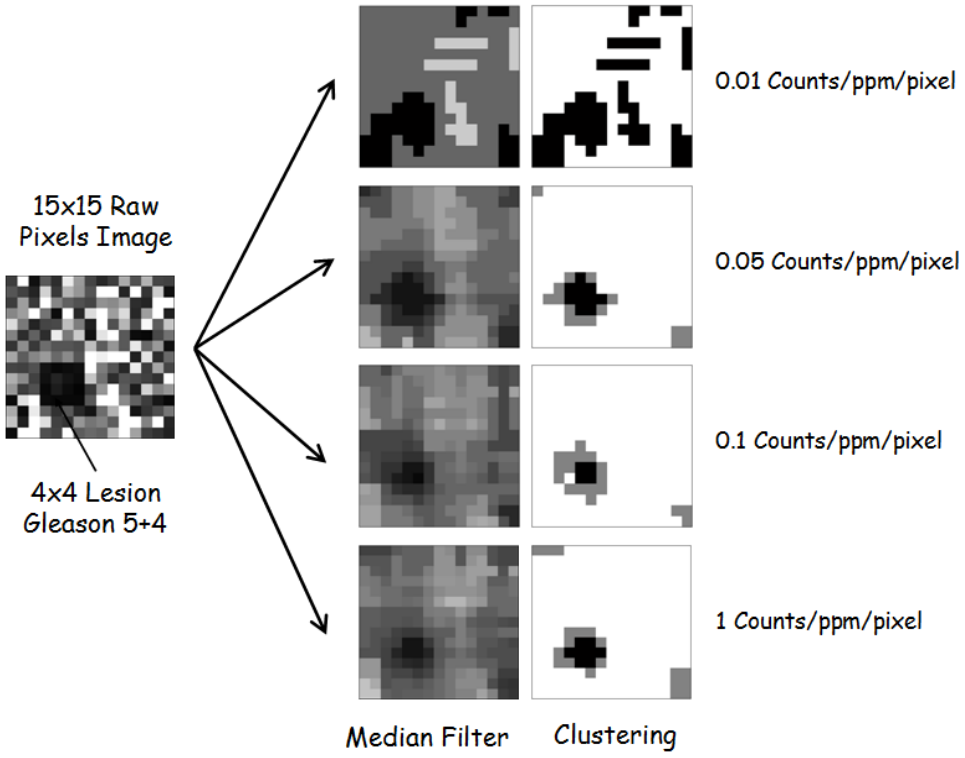

Figure 28. Examples of a simulated 15×15 pixels Zn map containing a 4×4 pixels cancer lesion (Gleason grade 5+4) and the resulting processed images created with different instrumental sensitivities (counts/ppm/pixel) of the imaging system.

Figure 29a shows the results of analysis of 15×15 pixels Zn-map images with 4×4 pixels lesions (occupying 7% of the image area). The figure illustrates the relation between the sensitivity of the detection system and the computed detectability, namely the AUC of the corresponding ROC. Figure 29b depicts the correlation between the system's sensitivity and the classifier test, LC_{Zn}, used for classification and grading.

As expected, the overall effect of counting statistics on lesion detectability and classification depends, non-linearly, on the assumed instrumental sensitivity (total number of detected counts per unit concentration of Zn). As the statistics improves, the detectability and LC_{Zn} asymptotically converge to values which depend only on the Zn contrast between the lesion and its surrounding benign tissue, namely on the Gleason grade of the cancer lesion. From figure 29 it follows that above an instrumental sensitivity of ~0.05 counts/ppm/pixel, the counting-statistics no longer

affects the detectability or the classification of the detected cancer-lesion. This conclusion holds irrespective of the image spatial resolution. We may conclude that there is an optimal irradiation dose above which no further improvement in diagnostic can be gained.

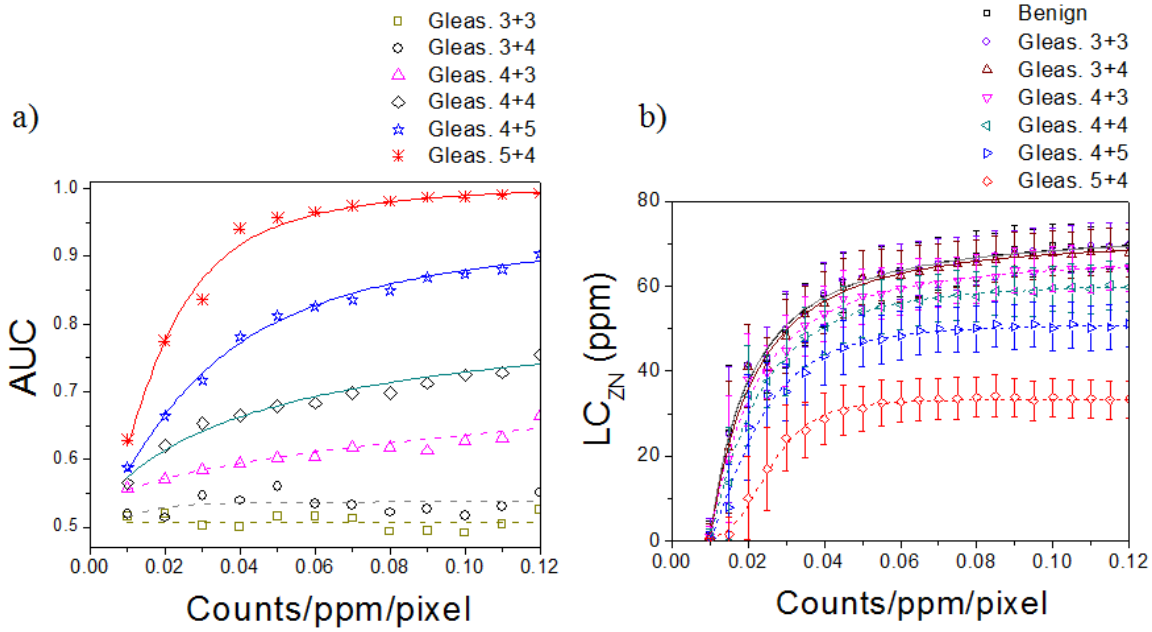

Figure 29. Evaluation of PCa detection performance for 15×15 pixels images, with 4×4 pixels simulated cancer lesion randomly located within the Zn-maps. The evaluation is presented for different Gleason grades, as function of the system sensitivity: (a) by AUC and (b) by LCZn, All the curves were fitted with Hill equation (Hill 1910).

Furthermore, for any image and lesion parameters it is possible to optimize the dose such that the statistical noise contribution is negligible, and therefore we can choose to ignore statistical noise in the following sections.

4.2.2 Prostate-cancer detection, localization, grading and staging

According to current general practice, only tumors larger than 0.5 cm^3 are considered to be of clinical significance, with further refinement claiming that tumor volume adjusted for grade is the appropriate predictor of disease-specific survival (Epstein et al. 1993). Malignancies with a volume of 0.5 cm^3 or less and a Gleason grade of less than 7, are declared clinically-insignificant and may be managed by watchful waiting (Cupp et al. 1995). Following this trend, within the present study we considered as clinically-relevant tumor sizes above 0.5 cm^3 for the more aggressive prostate cancers (above or equal to Gleason grade 4+4) and above 1 cm^3 for the less aggressive ones (below Gleason grade 4+4).

In the following we explore the relations between the map's pixel size/density and the lesion size and grade, on the performance of cancer detection and grading. We assume the maps to represent a typical prostate slice of 3×3 cm^2; the 0.5 cm^3 tumor appear as 0.64 cm^2 in the map.

4.2.3 Pixel-size/density and tumor-grade

Figure 30a corresponds to 15×15 pixels maps incorporating 4×4 pixels cancer-lesions and figure 30b to 30×30 pixels maps incorporating 6×6 pixels cancer lesions. The respective tumor areas are 0.64 cm^2 and 0.36 cm^2, and their respective volumes (assuming a cubic shape) are 0.5 cm^3 and 0.2 cm^3; notice that these values are beneath the diagnostic-relevant cancer-volume taken as references. Figure 30 clearly show that, in both configurations, for a fixed cancer-area the detection performance improves with the increase of Gleason grade.

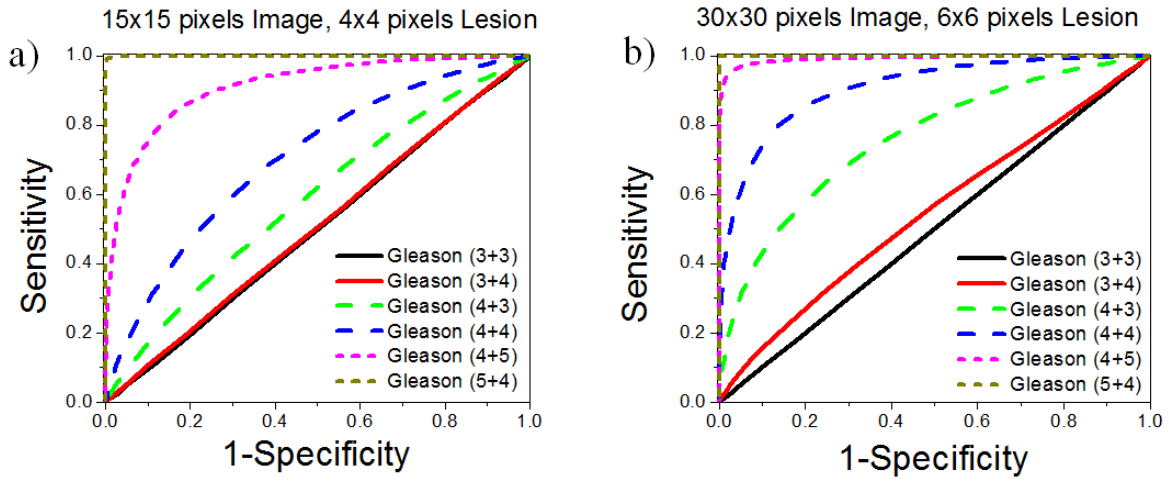

Figure 30. ROC analysis of the classifier detection-performance for different Gleason grades: a) 15×15 pixels image with 4×4 pixels lesion (lesion size 0.64 cm^2), b) 30×30 pixels image with 6×6 pixels lesion (lesion size 0.36 cm^2).

Furthermore, figure 30 makes it clear that the pixel size/density plays an important role in the detection performance: although the data of figure 30b refers to a lesions of smaller area, i.e. 4% of total image area, the performance in its detectability is superior compared to the data depicted in figure 30a, where the simulated cancer area is around 7% of the total image. This is due to the denser sampling of the Zn distribution (4 times more pixels per unit area).

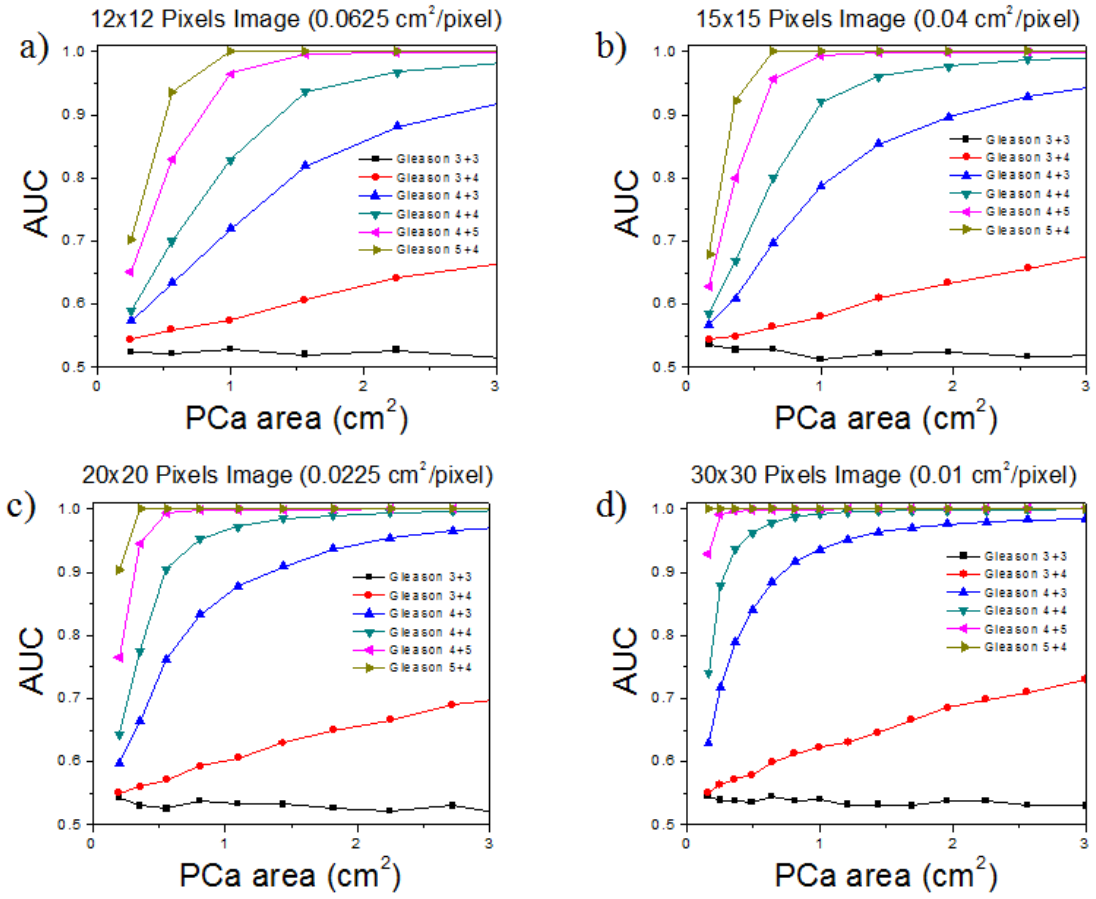

Figure 31. Predicted detection performance, represented by the area under the ROC curves (AUCs), obtained with the proposed classifier for various Gleason grades and lesion areas; they were calculated for different numbers of image pixels: a) 12×12, b) 15×15, c) 20×20 and d) 30×30. The corresponding spatial resolutions in cm^2/pixel are also indicated.

A systematic examination of the effect of pixel size/density is shown in the figure 31; the PCa detectability, expressed in terms of AUCs, is plotted as function of the cancer-lesion's dimension. For each Gleason grade the ROC was computed for various spatial resolutions and cancer-lesion sizes. The 3×3 cm^2 area was divided into either 12×12, 15×15, 20×20 or 30×30 pixels images, with corresponding spatial resolutions of 0.0625, 0.04, 0.0225 or 0.01 cm^2 per pixel. The PCa detection performance is excellent (AUC value close to 1) for high Gleason grades, even for very small lesion-size and relatively poor spatial resolution; e.g. the detectability of the cancer-lesion (expressed in term of AUC) for high Gleason grade (5+4) is 100% (sensitivity = 100%, specificity = 100%) in the case of 30×30 pixels image, no matter what the size of the lesion is. On the contrary, low spatial resolution image, like 12×12 pixels image, reaches 100% of detectability only for cancer lesion area above the threshold of 1 cm^2, which represents a detection limit. The

cancer area detection limit depends on both the Zn-map spatial resolution and the cancer aggressiveness grade.

In general, the results indicate that, under the present analysis scheme, there is an optimal spatial resolution and its further refinement would not provide substantial improvement of PCa detection. For low-grade cancer lesions (i.e. below 4 in the first component of the Gleason grade), the current detection performance is not satisfactory and may require a more efficient functional image processing; this could be for example an improved noise reduction (filtering) process and a more effective image-segmentation algorithm.

4.2.4 PCa grading/staging/localization

The image processing provides information on the average Zn levels and variance of the Zn distribution within each cluster (Section 4.1). This information is used for grading and staging of the detected lesion. This is demonstrated in figure 32, which summarizes the study on the relationship between LC_{Zn} value and the detected cancer area, for various Gleason grades.

The figure presents the average LC_{Zn} and its standard deviation, versus the detected cancer area (the two lowest-Zn cluster) and its standard deviation, for different Gleason grades. The detected area (lowest-Zn cluster area after detection process based on Zn classification) is expressed as fraction of the entire Zn-map area. Each point in the figure was obtained from statistical analysis of a series of 500 computer-simulated 30×30 pixels images, in which a cancer lesion of certain grade and area and random location was included. Each curve is the result of such analysis, with a series of increasing simulated lesion area, from 2×2 up to 14×14 pixels.

In figure 32 a line of "staging/grading limit" is drawn; below this line the curves (with the exception of Gleason 3+3 and 3+4, which are not distinguished, though separated from the higher grades) are separated by more than one standard deviation, thus permitting unambiguous staging and grading of the detected lesion (*decision boundaries*). Above this line the results are ambiguous due to the overlap and the convergence of all curves to a single point (the "ambivalent point" in figure 32). The staging/grading limit line cuts the various curves, at detected lesion area values, that depend on the grade. For example, for Gleason (5+4) it corresponds to a detected lesion area threshold of less than 0.16 cm^2, or detected lesion volume threshold of less than 0.064 cm^3. For a lower Gleason, of (4+3) for example, it corresponds to a detected lesion area threshold area of ~0.5 cm^2 or detected lesion volume threshold of 0.35 cm^3.

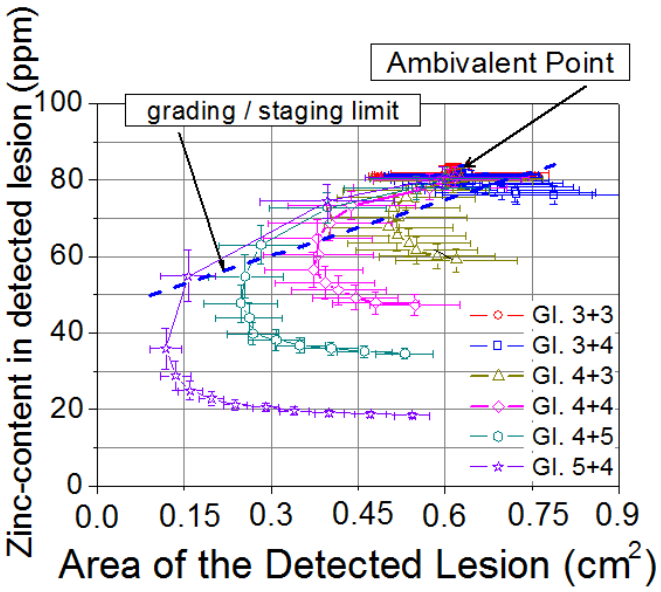

Figure 32. Lowest Zn value versus the detected cancer area (cm^2), for different Gleason grades. Each point in the figure correspond to the analysis of a set of 500 simulated images of 30×30 pixels; in each set a computer-simulated PCa area has been included, of dimensions ranging from 2×2 to 14×14 pixels, and location randomly chosen within the map.

The grading and staging of a detected lesion may be done on the basis of its correspondence to the curves of figure 32. In particular, the results illustrated in figure 32 may be used as training data for multi-classification problem (Gleason grading), by means of supervised learning approach (Kotsiantis et al. 2006), and one may design a learning algorithm in which predicted probability to belong to one of the different Gleason grade classification is calculated in terms of the normalized distances to the various decision boundaries of figure 32. For example, if a lesion with area 0.3 cm^2 and LC_{Zn} value of 25 ppm is detected, the normal distance between the measured point and the 5+4 decision boundary is very short while its normal distances to all the other decision boundaries are longer. This indicates that there is high probability that the detected lesion has a Gleason grade of 5+4.

We found that when using the present algorithm the "detected"-lesion area systematically deviates from the simulated one by an amount depending on the grade, as depicted in figure 33. In this case the "detected" area can be easily corrected to obtain the "true" area. In addition, we found that the performance of the image processing in localizing the cancer area depends largely on its Gleason grade and the size assigned to the simulated area. For moderately and poorly differentiated cancer (Gleason grade 4+3 and above) and for simulated cancer size > 0.5 cm^3, the false positive is below 5%; in the case of simulated cancer area with a well differentiated-Zn distribution (Gleason

grade 3+4 and 3+3) the false positive increases and, depending on the size, might be as high as 50%. This is because the precision at which the detected area can be defined depends on the contrast between cancer and benign Zn distributions and it improves with grade. Therefore, an iterative approach is needed: the grade is assigned on the basis of the information on detected area in combination with LC_{Zn}, as for example proposed above; then, the detected area is corrected to provide a more precise estimate on the true lesion area, etc. If the iterations converge, they will define an area value that is the basis for the staging assignment.

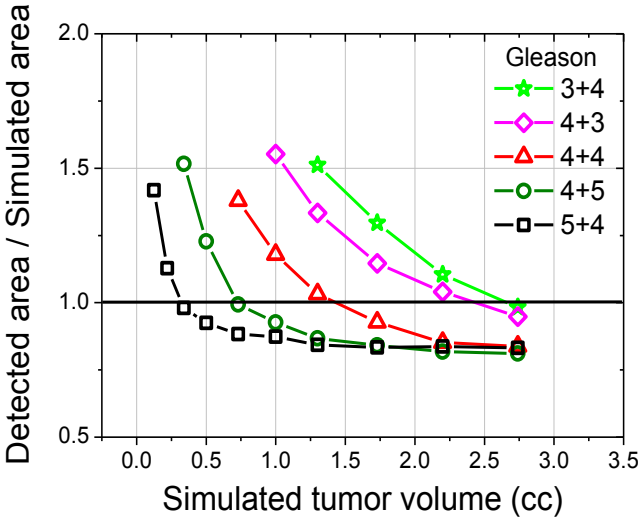

Figure 33. Using the present image processing algorithm, the "detected" lesion area is under-estimated by ~20% for the higher Gleason-grade combinations and overestimated by up to ~50% for the lower Gleason-grade combinations, for the clinically relevant tumor volumes.

In the case of low-grade cancers (3+3 and 3+4), the measured (figure 23) Zn concentration distributions are very similar to the non-PCa tissues; thus, their detection, based on the Zn-map and its analysis, is of low sensitivity and accuracy, and presently has little clinical diagnostic value. If a better contrast to the benign background will be revealed, the present method might be useful and of clinical value also for the low-grade cases.

A more comprehensive criterion for detection, grading and staging of the cancer lesion may be developed using supervised machine-learning approaches, using a probability measure and related confidence level to indicate that a certain detected low-Zn pattern belongs to a given Gleason grade class. In that case, it will provide an inclusive detection and grading probability for the examined prostatic tissue image, which constitute critical information for diagnosis and disease management.

5. Conceptual Design of the trans-rectal XRF probe

Our non-invasive *in-vivo* PCa detection concept involves determination of Zn distributions in the peripheral zone of the prostate aims at detecting Zn-depleted area - potentially indicative of clinically-relevant adenocarcinoma. The method is based on X-ray fluorescence (XRF) tomography; Figure 34 schematically illustrates a conceptual design of a trans-rectal XRF Zn-probe.

The 3D-XRF analysis is realized by irradiation of the gland, through the rectal wall, with a narrow X-ray beam (~1mm diameter) followed by the measurement of the characteristic Zn emission. The method requires a confocal arrangement consisting of X-ray optics, in both the excitation as well as in the detection channel. The overlap of the foci of the X-ray optics defines a small target-volume within the tissue (figure 35b). A displacement of the probe and the collimator displaces the target-volume within the gland; this provides a three-dimensional Zn-concentration image (Zn-map) of the probed tissue volume, pointing at Zn-depleted regions that are suspicious of the malignant process.

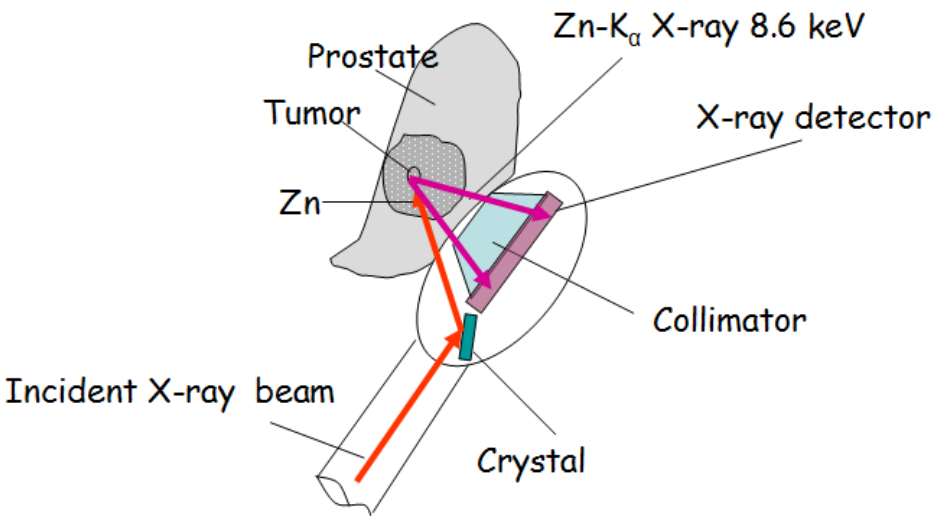

Figure 34. Schematic drawing illustrating conceptual design of the XRF probe.

Similar confocal configurations have been previously suggested by other groups (Kumakhov 2000b; Ding et al. 2000; C. Fiorini et al. 2001), as for instance in application of XRF to geochemical analysis of archeological specimens surface. These systems use exciting X-ray micro-beams (μ-XRF) that create micron-size target-volumes and offer excellent spatial resolutions. Differently, a diagnostic application of the XRF technique, such as our *in-vivo* Zn-content analysis

of the prostate, requires minimizing the radiation dose delivered to the patient and irradiation times, while ensuring reasonable detection limits (elemental concentrations). In our concept, the XRF probe necessitates of a large exciting beam (mm-size) and a large-area detector paired with a suitable dedicated collimator. In addition, an appropriate tuning of the energy spectrum of the exciting beam allows to achieve an optimal radiation exposure.

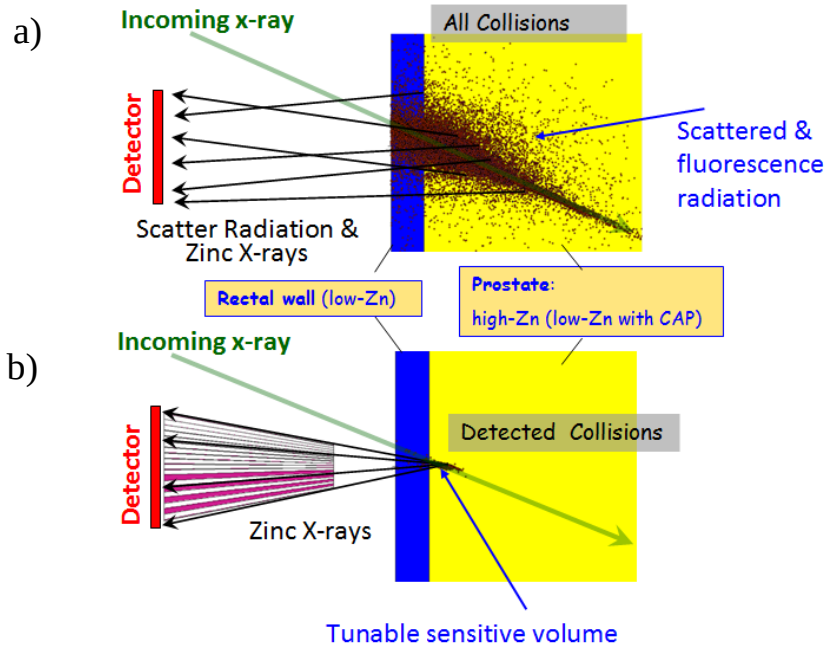

Figure 35. Computer-simulations, illustrating similar irradiation conditions of a prostate phantom but different detection conditions; a) without collimator a detector captures both Zn-fluorescence X-rays induced by the beam and by scattered radiation; b) with a collimator of a focal spot located at a depth of 4.5 mm inside the phantom (including 3 mm rectal wall); the detector captures only event from a small target-volume.

This chapter discusses the initial outline of the conceptual design of the XRF zinc-probe and its components, established by means of theoretical calculations and computer-simulations. Particular attention has been devoted to the design of the probe's key-element, namely the collimator placed between the spectroscopic planar X-ray detector and the examined object (a gland or its phantom); as shown in figure 35, without collimator the spectroscopic detector would be flooded by scattered radiation. The collimator dictates the overall quality of the XRF analysis, and affects the size of the inspected target-volume, zinc quantification limit (detection threshold, contrast), irradiation time, absorbed-dose delivered to the organs during the examination as well as the background originating from scattering of the incident radiation within the region surrounding the inspected volume (setting the detection limits).

Collimator parameters to be optimized are: geometry, holes-diameter and material. Calculations carried out for a simple conceptual design of a Table-Top experimental XRF system, with discrete elements, were the basis for the more complex design of laboratory and medical zinc-probe configurations; their expected performance were evaluated.

5.1 Optimum energy spectrum of the exciting beam

Let us consider the slab geometry schematically drawn in figure 36, in which the sample is irradiated by a mono-energetic and parallel exciting-photon beam, at an angles φ with respect to the surface normal.

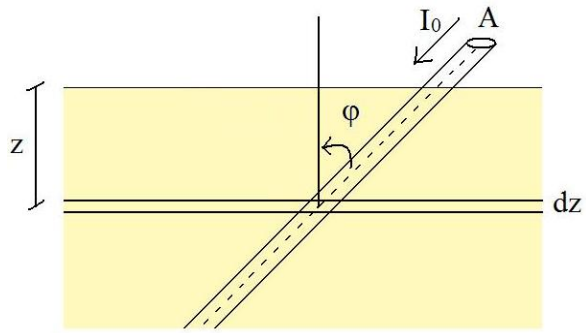

Figure 36. Schematic drawing of the XRF slab geometry

According Eq. 2.8, the number dN_z of Zn-K_α fluorescence photons, created within the volume element dV = A dz cos(φ), at depth z per unit time, is given by the formula:

$$dN_z = I_z\, \rho^{Zn}\, \omega_K\, \tau(\varepsilon)\, B\, A\, dz = I_0\, \rho^{Zn}\, \omega_K\, \tau(\varepsilon)\, B\, A \exp\left(-\mu(\varepsilon)\frac{z}{\cos(\varphi)}\right) dz \qquad (5.1)$$

where μ(ε) and τ(ε) are, respectively, the total linear attenuation coefficient (cm^{-1}) and the photoelectric mass attenuation coefficient (cm^2/g) for the Zn at energy ε (keV), I_0 is the exciting beam fluence rate (photons/cm^2/s) at the sample's surface, ω_K is the K-shell fluorescence yield (dimensionless), A is the area of the incident beam (cm^2), ρ^{Zn} is the density of the Zn in the sample (assuming for instance a Zn concentration in tissue of around 1000 ppm = 1000 μg/g, the corresponding Zn density is around 10^{-3} g/cm^3), and B is the branching ratio for Zn-K_α line (dimensionless). Notice that dN_z has the dimension of number of produced fluorescence photons per unit time (photons/s); they are emitted isotropically over 4π.

We may now introduce the efficiency of the X-ray production rate at depth z (fluorescence yield rate), denoted as $E_z(\varepsilon)$, representing the number of K_α fluorescence photons (8.6 keV for Zn) produced per unit time at depth z, normalized by the number of exciting photons impinging on the sample surface per unit time (I_0 A):

$$E_z(\varepsilon) = \frac{dN_z}{A\, I_0} = \rho^{Zn}\, \omega_K\, \tau(\varepsilon)\, B \exp\left(-\mu(\varepsilon)\frac{z}{\cos(\varphi)}\right) dz \approx \sigma_{PE}(\varepsilon) \exp\left(-\mu(\varepsilon)\frac{z}{\cos(\varphi)}\right) = F_z(\varepsilon) \qquad (5.2)$$

Notice that, according to Eq. 5.2, the fluorescence yield rate is a dimensionless quantity. Up to some irrelevant constants, $E_z(\varepsilon)$ depends solely on the product of two terms: the primary beam exponential attenuation factor $\exp\left(-\mu(\varepsilon)\, z / \cos(\varphi)\right)$ and the Zn photoelectric cross section σ_{PE}; both terms are function of the energy of the exciting photons beam ε. An ideal spectrum, optimized in terms of fluorescent yield, is then selected by maximizing the product of the two above terms (in Eq. 5.2 this product is symbolically denoted as $F_z(\varepsilon)$) with respect to the energy of the incident photons ε.

The equation describing the energy-dependent photoelectric cross section for the Zn element, $\sigma_{PE}(\varepsilon)$, and the linear attenuation coefficient for the prostatic tissue, $\mu(\varepsilon)$, have been obtained by fitting data taken from NIST database (Hubbell and Berger 1968) in the relevant energy range between 10-50 keV (figure 37). The ICRU 44 soft tissue (ICRU 1989) was assumed as reference model of prostatic tissue. The NIST data for $\sigma_{PE}(\varepsilon)$ and $\mu(\varepsilon)$ were fitted with an allometric and a logistic function, respectively.

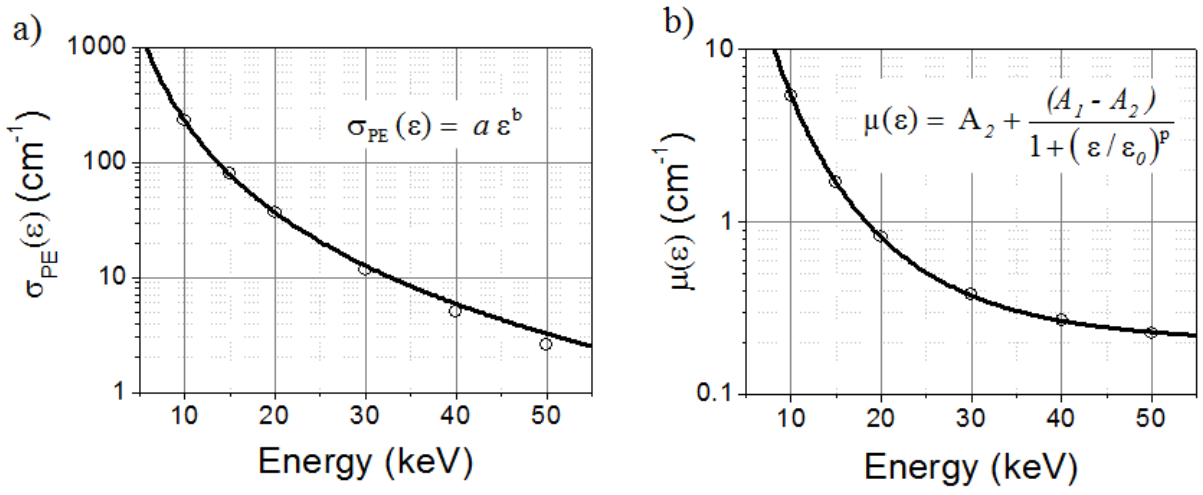

Figure 37. Fitting of the NIST data for Zn-line photoelectric cross section $\sigma_{PE}(\varepsilon)$ and for the linear mass attenuation coefficient $\mu(\varepsilon)$, in the incident energy range 10-50 keV. In the two graphs are also shown the fitting model functions.

Combining the resulting fits of $\sigma_{PE}(\varepsilon)$ and $\mu(\varepsilon)$ functions with equation Eq. 5.2, we obtained the plots of $F_z(\varepsilon)$ as function of the exciting photons' energy at various irradiation depths z (figure 38); the plots corresponding to different irradiation depths (z) are shown in different colours.

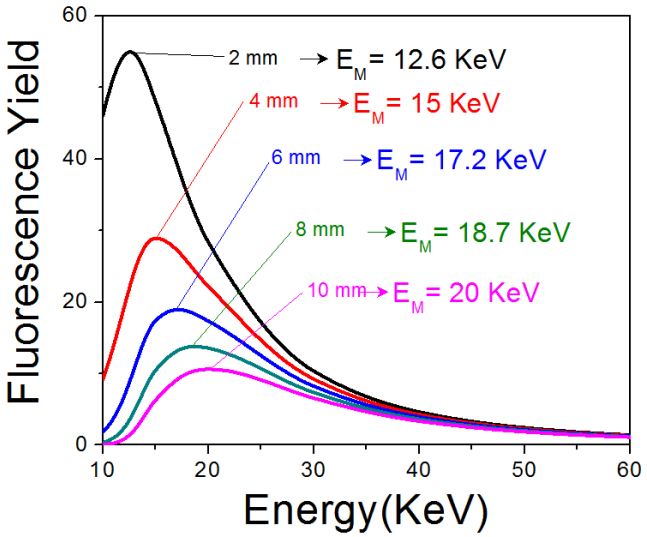

Figure 38. Zn Fluorescence yield $F_z(\varepsilon)$ at different depth as function of the exciting beam energy.

Notice that, the "irradiation depth" is always defined as the distance from the rectal-wall surface (it includes 0.3 cm thick rectal wall tissue), and thus, we will consider an irradiation range in the gland between 0.3-1 cm as relevant depth in terms of PCa detection. As shown in figure 38, for these relevant irradiation depths, the most efficient energies are within the range of 14-20 keV.

In the same fashion, the optimization of the fluorescence yield may be carried out with respect to the absorbed dose delivered to the patients. The absorbed dose for a mono-energetic photon beam is defined as

$$D(\varepsilon) = \Psi_\varepsilon \left(\frac{\mu_{en}}{\rho}(\varepsilon) \right) = \Phi\, \varepsilon \left(\frac{\mu_{en}}{\rho}(\varepsilon) \right) = \frac{N}{A}\, \varepsilon \left(\frac{\mu_{en}}{\rho}(\varepsilon) \right) \qquad (5.3)$$

where μ_{en}/ρ is the mass energy-absorption coefficient and Ψ_ε is the photon energy fluence (note that $\Psi_\varepsilon = \Phi\, \varepsilon$, where Φ is the photon fluence (photons/cm^2) and ε the exciting-photon energy). Again, the equation describing the mass energy-absorption coefficient for ICRU 44 soft tissue model, as function of the exciting-photon energy, has been obtained by fitting NIST data (figure 39 – the fitting function model is also shown).

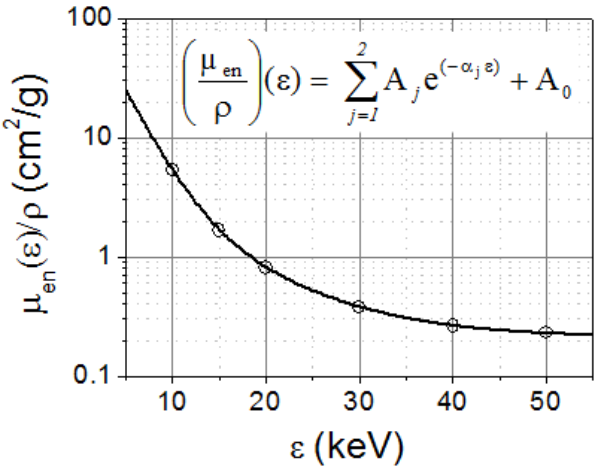

Figure 39. Fitting of the NIST data for mass energy-absorption coefficient $\mu_{en}(\varepsilon)$, in the energy range 10-50 keV. The fitting model function is also shown.

As reference quantity we may consider the Entrance Surface Dose (ESD) per number of absorbed exciting photons (Edwards 1999). ESD is mathematically defined as

$$\frac{ESD}{photons} = \frac{D(\varepsilon)}{N} = \frac{\varepsilon}{A}\left(\frac{\mu_{en}}{\rho}(\varepsilon)\right) \tag{5.4}$$

where N is the total number of exciting photons at the patient's rectal surface. The mean entrance surface dose per exciting photon has the dimension of keV/g/exciting-photon.

In order to evaluate the optimal energy spectrum for the exciting beam in terms of absorbed dose, let us define an appropriate figure of merit (FOM) which, for each value of the exciting-photon energy, takes into account the proper fluorescence yield and the mean entrance dose. The FOM is formally defined as:

$$FOM(\varepsilon) = \frac{1}{F_z(\varepsilon)}\frac{D(\varepsilon)}{N} = \frac{exp\left(\mu(\varepsilon)\frac{z}{\cos(\varphi)}\right)}{\sigma_{PE}(\varepsilon)}\frac{\varepsilon}{A}\left(\frac{\mu_{en}}{\rho}(\varepsilon)\right) \tag{5.5}$$

Notice that, the first term of the above expression ($F_Z^{-1}(\varepsilon)$) is equivalent to the number of exciting photons needed to yield a certain amount of counts in the Zn peak; indeed, the higher is the fluorescence yield the lower exciting fluence beam is needed to detect a specific number of photons. So, the defined FOM is equivalent to the total absorbed dose as function of the exciting beam energy, having required a specific confidence level for the XRF measurements (figure 40).

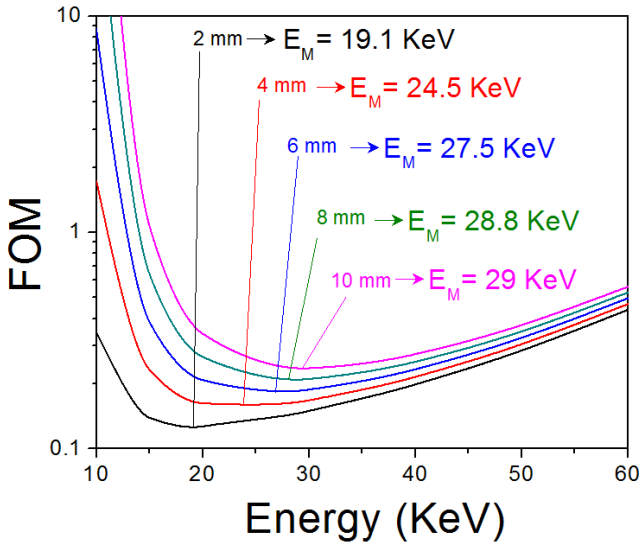

Figure 40. Figure of Merit (FOM), (Eq. 5.6), as function of the energy of the exciting photons' beam at different depths. The optimal energy values of the exciting beam, at which minimal absorbed doses are delivered, are also indicated.

The graphs in figure 40 reveal that, in terms of absorbed dose, the most efficient energies are within the range of 20-30 keV, according to the different irradiation depths, in the relevant range between 0.3-1 cm.

5.2 Fluorescence Yield and detection sensitivity

As already introduced in the previous section (see Eq. 5.2), the number of fluorescent X-ray photons dN_z, produced in a volume element dV at a depth z, is given by the following equation:

$$dN_z = I_0\, \rho^{Zn}\, \omega_K\, \tau(\varepsilon_1)\, B \exp\left(-\mu(\varepsilon_1)\frac{z}{\cos(\varphi)}\right) A\, dz \qquad (5.6)$$

where we have indicated as ε_1 the energy of the exciting photons.

The number of fluorescence radiation photons, detected within a specific solid angle ($d\omega = \sin(\theta)\, dz\, d\varphi\, d\theta$) along the direction θ (figure 41), may be computed as

$$dN_z(\theta) = \frac{I_0}{4\pi}\rho^{Zn}\, \omega\, \tau(\varepsilon_1)\, B \exp\left(-\mu(\varepsilon_1)\frac{z}{\cos(\varphi)}\right) \exp\left(-\mu(\varepsilon_2)\frac{z}{\cos(\theta)}\right) A \sin(\theta)\, dz\, d\varphi\, d\theta \qquad (5.7)$$

Notice that another exponential factor was introduced to take into account the attenuation of emitted fluorescence photons of energy ε_2 (the emitted Zn-K_α fluorescence photons have an energy

of 8.6 keV). The normalization factor $1/4\pi$ was introduced in order to take into account that the characteristic Zn fluorescence is emitted isotropically.

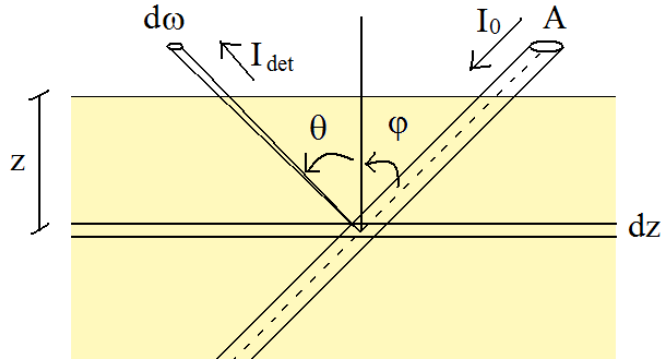

Figure 41. General XRF slab geometry.

The total number of detected Zn fluorescence photons is then calculated by integration of the above Eq. 5.7, over the entire solid angle seen by the detector surface and over the whole target-volume.

The sensitivity of the XRF detection system may be defined as the number of recorded Zn-fluorescence counts (K_α peak), per number of impinging excitation photons and per average concentration of Zn in the target volume (ppm):

$$\text{Sensitivity} = \frac{\text{Detected Zn Fluorescence}}{(\text{ppm of Zn})(\#\text{ of exciting photons})} = \frac{\text{Counts}}{\text{ppm photons}} \tag{5.8}$$

The sensitivity is a crucial quantity characterizing the overall quality of the XRF analysis as well as many other important parameters, like the limit of detection (LOD), measurement precision, irradiation time and absorbed dose delivered to the patient. The detection sensitivity depends on:

-) the collimator design and its capability in defining a directional correspondence between a small point of emission (target volume) and the detector;

-) the energy spectrum of the incident radiation

-) energy resolution and efficiency of the spectroscopic X-rays detector

-) radiation background resulting from scattering of the incident radiation or from regions surrounding the target volume.

The integration of Eq. 5.7 has no simple solution due to the complexity of structure and location of the target-volume, even for a rudimental collimator design. In order to overcome this problem and in order to be able to evaluate and to characterize the performances of some different detection system designs, we calculated the sensitivity by extensive Monte Carlo simulations. The

latter were carried out using Monte Carlo N-Particle transport code (MCNP), (Forster et al. 2004), a well-established packaged for modeling the radiation absorption, X-ray fluorescence and radiation scattering within the prostate phantoms and the probe components. The Monte Carlo simulation approach provided a simple and powerful tool for testing the different collimator system configurations that have been designed, providing the estimation of some relevant parameters concerning the overall detection performances. The simulations were carried out using MCNP Ver. 5, available at the FriXy lab at the University of Milan (Italy). Laboratory phantom investigations with an XRF table-top system, which design is based on these simulations, are discussed in chapter 6.

5.2.1 Collimator Design

The computer-simulated collimator structure, conceived and optimized by a systematic feasibility study reported here, consists of an array of 307 con-focal conical capillaries fused to form a 1.5 cm thick X-ray absorber (figure 42) – its focus is at 1 cm away from the small face. For simplicity, the simulation assumed the collimator to be made by a perfectly absorbing material – this assumption is not far from reality, as for low energy photons the scattering cross section is negligible compared to the photoelectric one. Each single conical capillary has a diameter of 0.1 cm at the large face and a diameter of about 0.02 cm the on the small one. The total area of the collimator facing the detector surface is of ~3.5 cm^2; however, the fraction of open area of the collimator, defined as the sum of the open area of individual channels divided by the total cross section area, is around 0.7, corresponding to an effective area of ~ 2.4 cm^2.

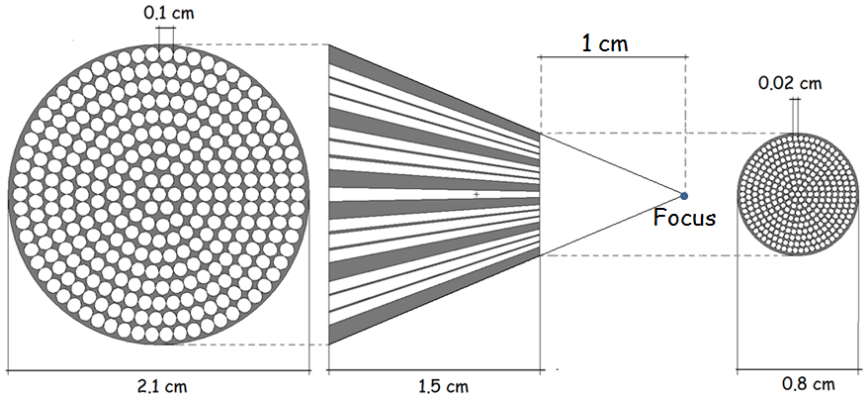

Figure 42. Schematic view of the confocal collimator. The detector is placed on the larger face, which has a total area of ~3.5 cm^2 and an effective open-area of ~70%. The middle drawing illustrates the holes disposal across the vertical cross section.

This collimator is placed between the circular detector, located at its larger surface and the irradiated tissue, facing the smaller face (figure 42). The conical convergence permits restricting the detection sensitivity to a small irradiated voxel, thus getting depth information and minimizing the sensitivity to scattering-induced fluorescence.

This proposed geometrical configuration is conceptually different than the ones considered and described in previous works; in reference (Shilstein et al. 2006), for instance, the system geometry comprised a primary beam passing through a central aperture in a multi-collimator plate and through a corresponding opening in an annular-shaped X-ray detector (backscattering configuration). In such a geometry the effective area of the detector and the target-volume can be kept reasonably small (target-volume should not exceed a mm^3 scale) only if one employs a micro-focus primary beam; the latter causes serious absorbed-dose limitations and low detection efficiency in spite of the high irradiation dose, and has large sensitivity to scattered radiation. According to our estimates, presented in details in the next paragraphs, the new design is expected to provide good counting statistics, with reasonable sensitivity, within permissible dose limits and irradiation times.

5.2.2 MCNP simulations and computation of sensitivity

The sensitivity of the collimator system described above has been evaluated by MNCP simulations, based on the following assumptions:

1. We considered a “far-field geometry” (non-divergent primary beam) and assumed the prostate to be approximated by a cylinder with two uniform compartments: a 0.3 cm thick “rectal compartment” with no Zn, and a "prostatic compartment" with a certain Zn concentration (figure 43); to speed up the Monte Carlo simulations a “nominal” Zn concentration of 1000 ppm was used in the "prostatic compartment". We estimated that, even at such relative high Zn concentration, the matrix effect (self adsorption of Zn-fluorescence photons) is negligible.

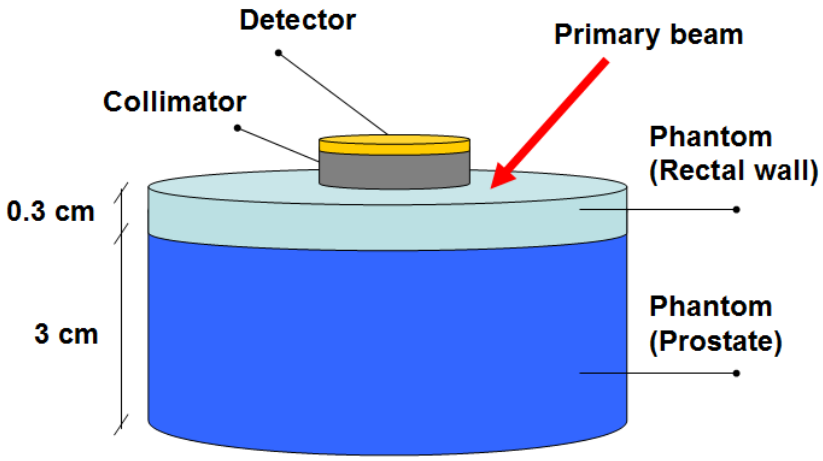

Figure 43. Schematic view of the simulation configuration. The phantom is composed of two compartments: a 0.3 cm thick rectal wall (no Zn), and 3 cm thick prostatic compartment (1000 ppm of Zn).

2. The source is mounted such that the collimated photon-beam has an angle of ~45° with respect to the normal of the phantom surface. The incident beam is composed of parallel and mono-energetic, 18 keV X-rays.

3. In the following calculations we will assume that the prostatic-tissue background is well represented by the ICRU 44 soft tissue model (Goldstone 1990), with density of 1.06 g/cm^3 and the following composition:

   Hydrogen (H=10.2%), Carbon (C=14.3%), Nitrogen (N=3.4%), Oxigen (O=70.8%), Sodium (Na=0.2%), Phosphorus (P = 0.3%), Sulfur (S = 0.3%), Chlorine (Cl=0.2%) and Potassium (K = 0.3%).

4. The XRF detector is assumed to have the efficiency response shown in figure 44, which is the same as the efficiency response shown by the AXAS-P-detector system (KETEK X-rays Detector) mounted on the table-top XRF system used in our previous experiments (Cortesi et al. 2008). The energy resolution of the computer-simulated detector was set at a value of 2.5% (150 eV FWHM) at the reference energy of 5.9 keV (as in the AXAS-P-detector system).

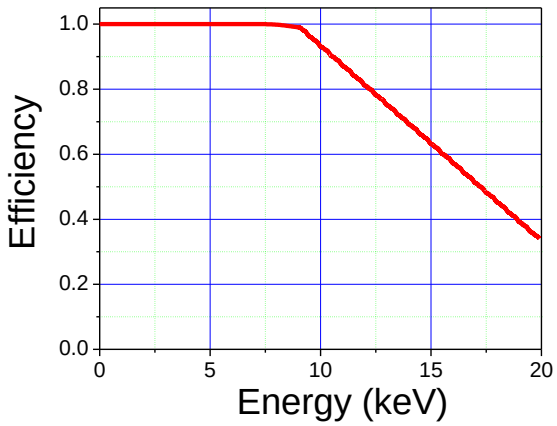

Figure 44. Detector efficiency response function versus energy, of the detected photons, for the simulated X-ray detector (KETEK X-rays Detector).

figure 45 shows an example of a recorded X-ray spectrum obtained from the simulated probe system described above. The absolute amount of Zn in the scanned sensitive volume is assumed to be proportional to the intensity of the Zn-K lines (area under the characteristic peaks). The broad peak in the spectrum is due to the scattering (coherent and incoherent) of the monochromatic (18 keV) exciting radiation. It is used for normalization purposes of the absolute Zn-content in the irradiated tissue (see chapter 3). The area under the two Zn-peaks, K_α and K_β, corresponds to $1.44 \cdot 10^{-4}$ counts (here for 1000 ppm Zn and a target volume of ~1.5 mm^3).

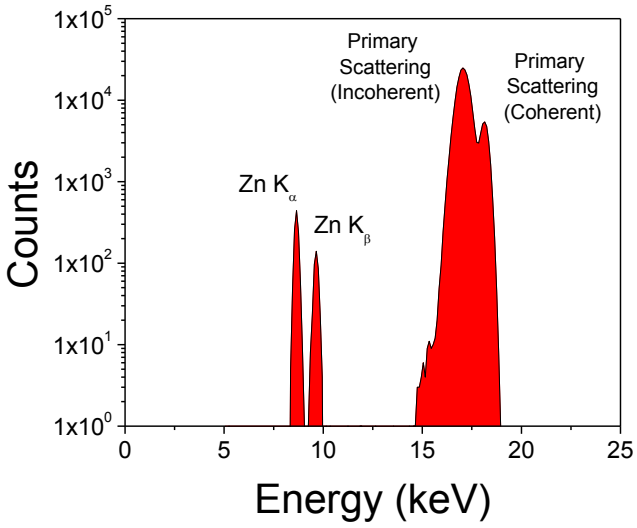

Figure 45. MCNP5-simulated energy spectrum obtained by a scanned "prostatic compartment" of a phantom, with 1000 ppm of Zn (shown in Fig. 42).

The dependence of the simulated sensitivity of the detection system versus voxel depth is illustrated in figure 46. The computation of the sensitivity has been performed for several

irradiation conditions, namely, three different primary beam diameters (1, 1.5 and 2 mm) and different scanning depths; the latter are the distances between the phantom surface and the focal spot of the collimator system, around which the detectable X-ray fluorescence is emitted. The number of counts used to compute the sensitivity was obtained by integrating the detected Zn characteristic K_α-line intensity; however, better sensitivity and statistics can be obtained integrating both K_α and K_β-lines; K_α emission is larger than the K_β one in a ratio of around 10:3. It is important to notice that, for the time being, we assumed homogeneous compartments, and thus for the sake of the Zn concentration computation, we considered the absolute Zn-K_α peak intensity (the ration K_α/K_β is function of the irradiation depth); for inhomogeneous compartment one may design a normalization procedure involving the Compton peak (peak of incoherent scattered radiation), of which the area is proportional to the mass density of the irradiated sample (Shilstein et al. 2006).

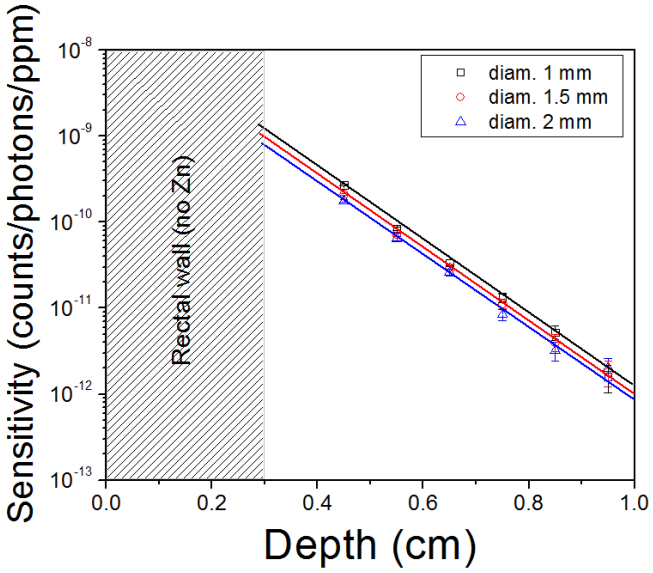

Figure 46. Sensitivity (counts/photons/ppm) versus voxel-depth in the phantom, for different primary-beam diameters: 1, 1.5 and 2 mm.

From the above results it follows that the sensitivity decays exponentially with depth and it slightly decreases for larger exciting-beam diameters. As shown by figure 46, the enlargement of the exciting beam diameter is not effective since by enlarging the beam one irradiates more and more tissue that is not visible through the collimator; eventually this leads to the decrease of sensitivity. Indeed, maximum sensitivity is achieved when the exciting beam illuminates the entire target-volume "seen" by each single conical capillary. The geometrical structure of the conical capillaries is therefore tailored to match the target volume size, in order to collect all radiation emitted by the target-volume at the focal spot.

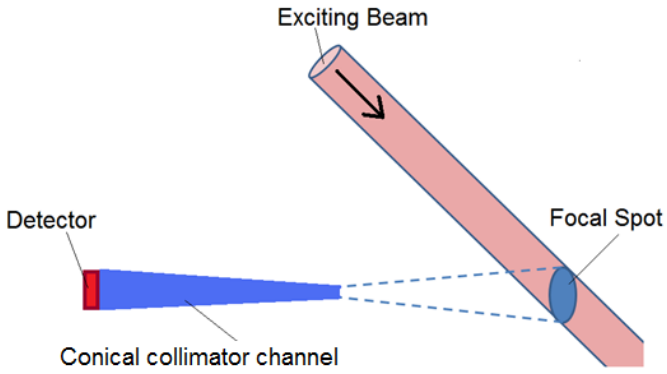

Figure 47. For maximum sensitivity the exciting beam diameter needs to match with the focal spot size seen by each conical collimator channel.

5.2.3 Scattering contribution to the detected XRF intensity

The scattering contribution to the sensitivity has been calculated through a series of simulations using the following approach: we have considered a sample composed of two tissue-equivalent (TE) compartments, namely a thin layer (1 mm thick) with homogeneous Zn concentration (1000 ppm) immersed within a homogeneous compartment with no Zn. Then, we have counted the number of detected fluorescence photons when the Zn-enriched TE layer was placed at different depths (figure 48); in this way we were able to evaluated the contribution to the sensitivity from irradiated volume out of the target volume, namely a contribution through scattering.

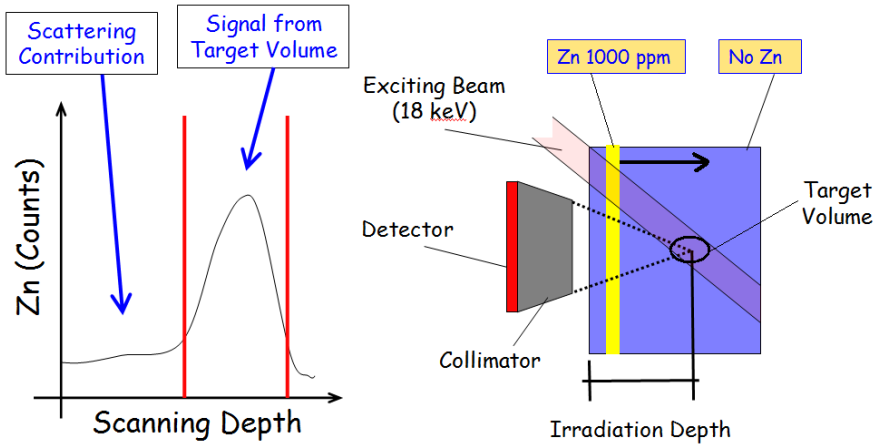

Figure 48. Methodology adopted in the simulations performed for scattering contribution assessment. A thin Zn-enriched TE layer is placed at different depths within a homogeneous TE compartment with no Zn, such that it is possible to determine the contribution of the detected fluorescence from different depths, originating from points out of the target volume.

We expect that the main contribution to the sensitivity would come from the target volume, defined by the intersection between the solid angle seen by the detector through the collimator and the sample tissue directly irradiated by the exciting beam; the number of counts from the target volume is the proper quantity to be used for the computation of Zn concentration in the examined voxel. The detected fluorescence created between the sample surface and the target volume causes enhancement of the Zn peak due to scattering contribution, an enhancement which increases with scan depth. The scattering reduces the quality of the scanned image and affects the XRF limit of detection, namely the threshold for Zn concentration that the instrument can resolve.

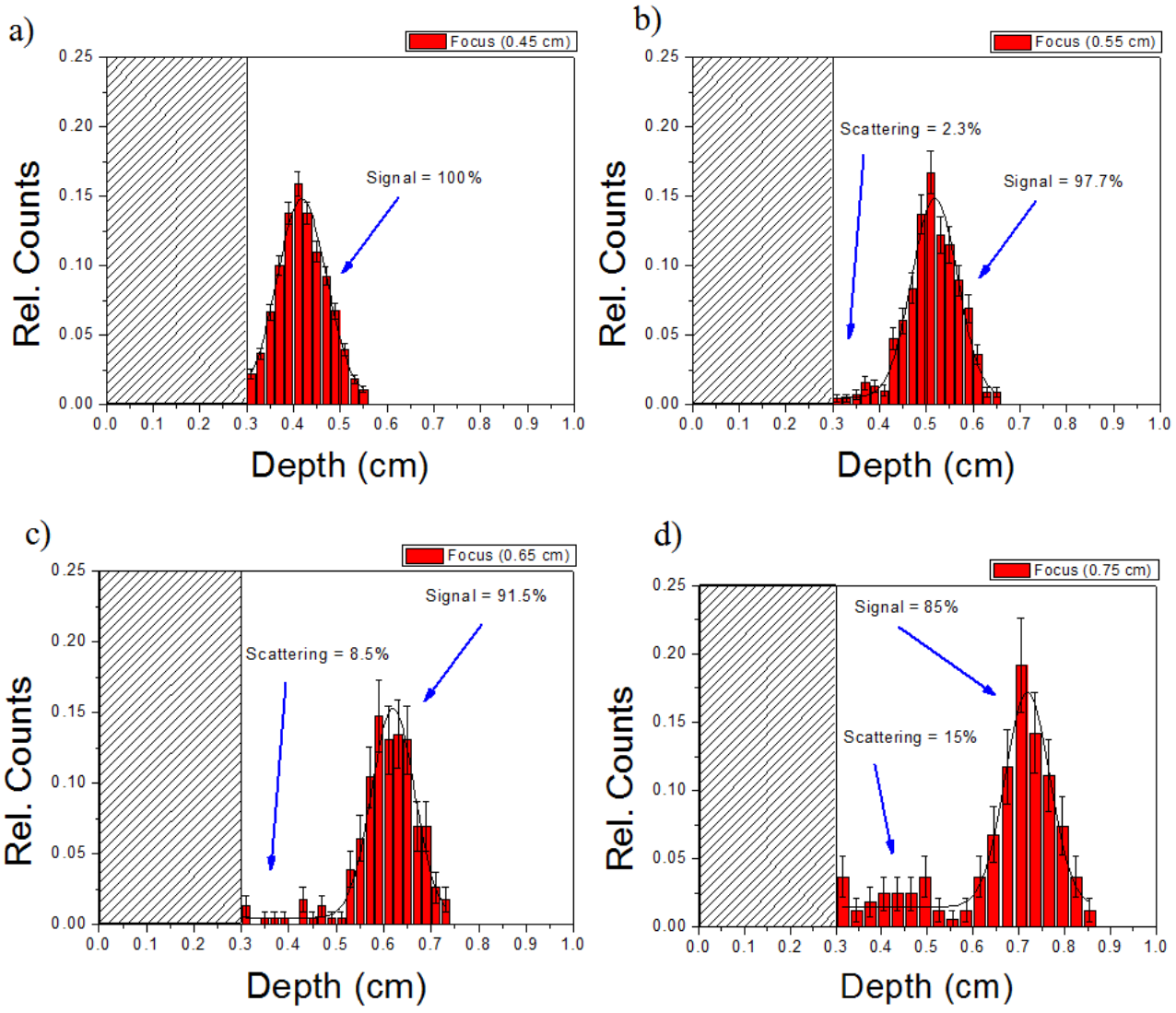

Figure 49. Evaluation of the scattering contribution for different irradiation depths: a) at 0.45 cm, b) at 0.55 cm, c) at 0.65 cm and d) at 0.75 cm. The computation of the scattering contribution to the sensitivity does not include fluorescence originated from the 0.3 cm rectal wall.

The graphs in figure 49 summarize the results of the simulations for different irradiation depths. The Gaussian centred at the irradiated depth (focus) in each graph represents the signal originated from the target volume; the "background" originating from the tissue existing between the sample's surface and the target volume constitutes the scattering contribution.

Notice that in these simulations we assumed that the Zn concentration in the 0.3 cm rectal wall is negligible, as well as the scattering contribution originating from it; the contribution of the rectal wall to the detected Zn fluorescence will be discussed in the next section. Figure 50 illustrates the scattering contribution as function of the irradiation depth, excluding the rectal wall; for the deepest irradiation depth of 0.95 cm the scattering contribution is about 20%.

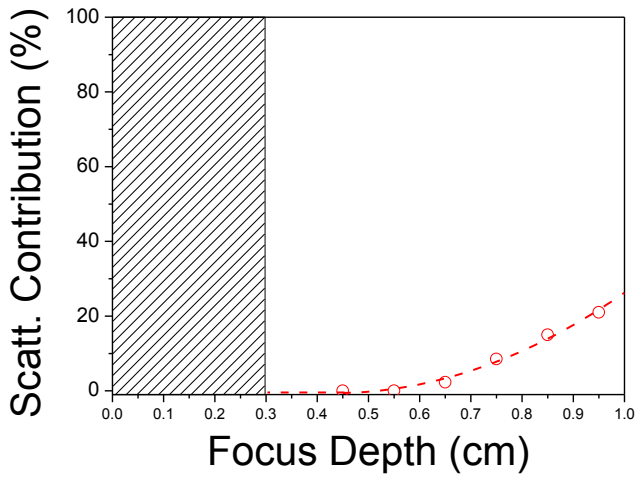

Figure 50. Scattering contribution to the sensitivity as function of the irradiation depth; the rectal wall is 0.3 cm thick and assumed to have 0 Zn.

6. Table-Top XRF experiments

The calculations and the computer-simulations, presented and discussed in the chapter 5, indicated at the critical parameters of a trans-rectal probe design; these necessitated careful experimental validation.

The general set-up of the experimental table-top XRF system (see photograph and scheme in figure 51) may be considered as an expanded version of the future trans-rectal probe; it comprises an exciting channel (X-ray source and focusing system), and a detection channel (collimator and detector). The exciting channel provides a quasi-parallel narrow monochromatic (~18 keV) photon beam, while the detection channel defines a small inspected volume-element (target-volume) from which the detected fluorescence is originated, with the aim to permit scanning the elemental distribution within the prostate/prostate-like phantom volume.

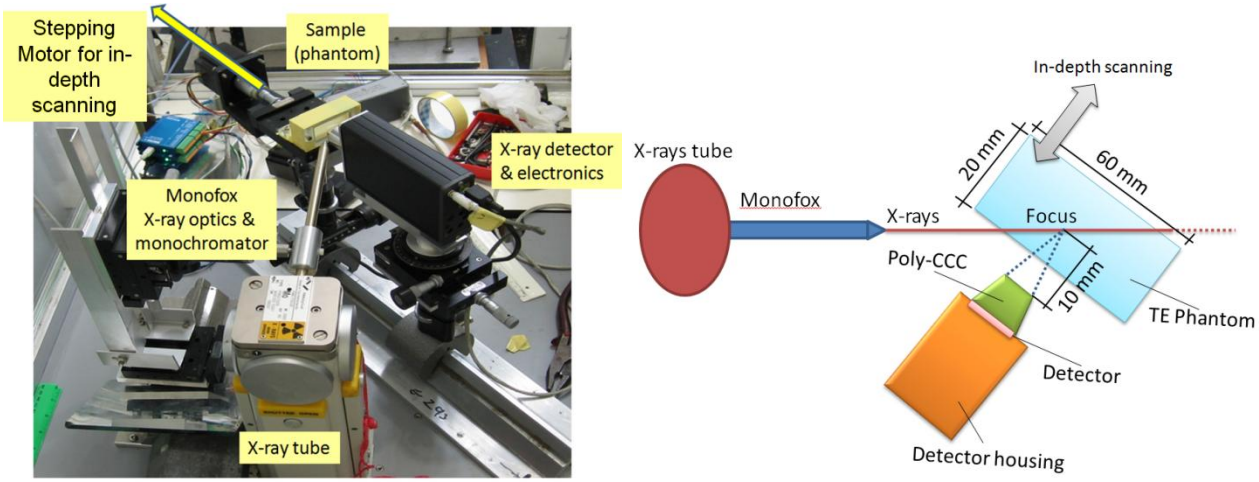

Figure 51. Photograph (a) and Schematic view (b) of the table-top XRF experimental set-up.

The measurements with the table-top XRF system were carried out with phantoms made of TE materials that mimic, as closely as possible, the prostatic tissue (i.e. materials equivalent to soft tissue). More specifically, these materials have mass attenuation coefficients, mass energy-absorption coefficients and densities similar to that of soft tissue, over the relevant XRF (incident and fluorescent) energy range (typically 8-20 keV).

The prostatic-like phantoms were mounted on a computer-controlled movable table. This allowed depth-profile scanning and 2D Zn-map imaging by an accurate displacement of the target-volume within the sample. Phantom 3D-displacement, acquisition and storage of the spectroscopic data were automatically controlled by dedicated software written using NI-LabVIEW (Blume 2007).

In more details, the following relevant quantities and items have been determined:

-) lateral dimensions of the target volume and its profile along the in-depth direction (sensitivity profile). The target-volume is the result of the overlap between the X-ray exciting beam and the foci of the detection-channel optics. Its displacement across the relevant prostatic (phantom) region permits to resolve in-situ the Zn concentration. It defines the in-depth resolution of the XRF scanning procedure.

-) the sensitivity of the XRF detection system (namely the fluorescence yield versus beam intensity and zinc concentration). It is a crucial parameter characterizing the overall quality of the XRF analysis as well as many other important factors, like the limit of detection (LOD), measurement precision, irradiation time and absorbed dose delivered to the patient.

-) contribution of the surrounding-tissue scattering, which affects the XRF limit of detection (i.e. the threshold of Zn concentration that the instrument can resolve with an acceptable precision).

The results of these experiments provided tools for a comprehensive characterization of various XRF probe components and features. It was possible to draw some conclusions about the expected overall detection performances (detection sensitivity, accuracy, limit of detection, etc.), identifying the number of pixels required per scanned image, maximizing the detection depth and depth resolution, adjusting the inspected target-volume size and shape enhancing the detection of low Zn levels.

6.1 Material and methods

6.1.1 Exciting channel - X-rays Source

The exciting monochromatic photon beam was provided by a fine focus (FF - 0.4×0.8 mm^2) XRD glass tube (2 kW, Mo target, PANalytical PW2215/20), coupled to a Mono-XG X-rays guide (IFG - Institute for Scientific Instruments GmbH, Germany) – see figure 52. The latter is a device consisting of a cylindrical capillary optics combined with a highly orientated pyrolytic graphite monochromatizing crystal (HOPG) with a mosaic structure (Bzhaumikhov 1998; Beckhoff et al. 2006).

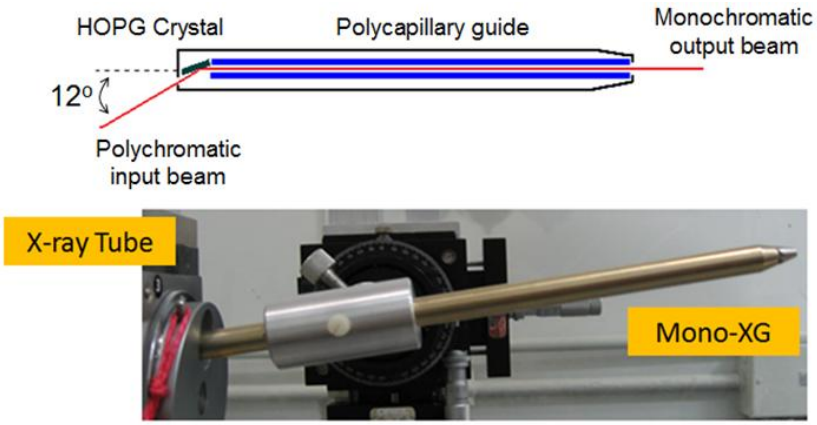

Figure 52. Assembly of the exciting channels, comprising an X-ray tube and a Mono-XG device (monochromatizer element paired with a capillary guide).

At an optimal HOPG crystal location, the monochromatized output photon beam has a circular section (1 mm in diameter) and a divergence smaller than 5 mrad; the photon beam spectrum is characterized by a sharp peak (figure 53) with mean energy of around 17.5 KeV (Mo-K_α line) and intrinsic energy resolution (FWHM) of 180 eV. The resulting output photon fluence rate at 2kW power of the tube was of the order of 10^8 photons/mm^2/sec.

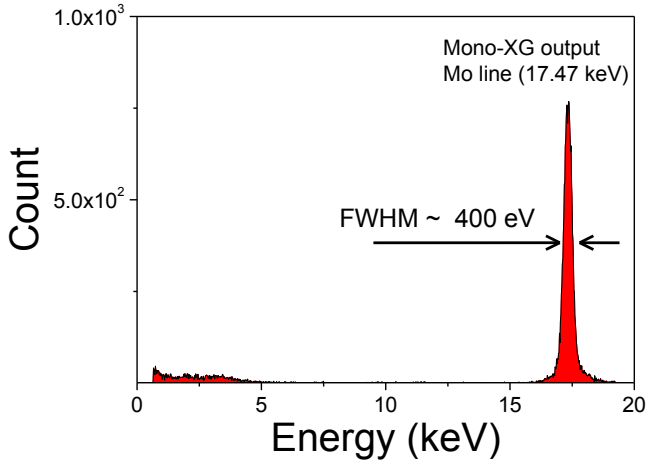

Figure 53. Typical output photon beam spectrum emerging from the Mono-XG; the output radiation has a main peak centered at energy of ~17.5 keV (Mo-K_α line).

Note that the spectrum depicted in figure 53 was acquired with the Si-PIN diode detector at a distance of ~5 mm, over 10 seconds. The recorded Mo-K_α peak (17.5 KeV) has a full width at half maximum ($FWHM_{Peak}$) of ~400 eV. This value results from the combination of the intrinsic resolution of the detector (ΔE_{Det} ~360 eV) and the actual energy spread of the Mono-XG output beam (ΔE_{Mono} ~180 eV), according the following equation

$$\mathrm{FWHM}^2_{\mathrm{Peak}} = \Delta\mathrm{E}^2_{\mathrm{Det}} \times \Delta\mathrm{E}^2_{\mathrm{Mono}} \quad (6.1)$$

6.1.2 Detection Channel - Spectroscopic X-rays detectors and Collimators

The detection channel defines a small inspected volume-element (target-volume or sensitive-volume) from which the detected fluorescence originates; its displacement within the scanned phantom permits 3D imaging of the elemental distribution within its volume.

As indicated by computer-simulation study (see chapter 5), the optimum design of the detection system comprises of a large area spectroscopic detector preceded by a poly-capillary conical collimator structure (Poly-CCC).

The Poly-CCC is a monolithic system made of micro structured anti-reflecting (AR) glass consisting of a large number of capillary channels oriented to one point. The divergent fluorescent radiation, emitted in the target-volume, is captured by the capillaries and transmitted to the detector by means of multiple reflections (Bjeoumikhov, Langhoff et al. 2005; De Samber et al. 2008; Vincze 2004). This allows scanning selected voxels of interest within the gland, getting additional depth resolution within the limits of the emission depth for the secondary fluorescence radiation, and therefore to enhance the sensibility of the detection system. Polycapillary lenses were introduced for the first time by Kumakhov (Kumakhov 2000a), and have been largely developed for 3D micro XRF applications, based on the principle of a selective depth-resolved detection of secondary fluorescence radiation (Bronk et al. 2001; Gao et al. 1997; Dhez et al. 1999).

Few Poly-CCC prototypes, of which the designs, dimensions and structures were tailored and refined according to the results of our systematic MCNP simulation studies, were manufactured by IfG (Germany) – figure 54 illustrates an example of Poly-CCC prototype.

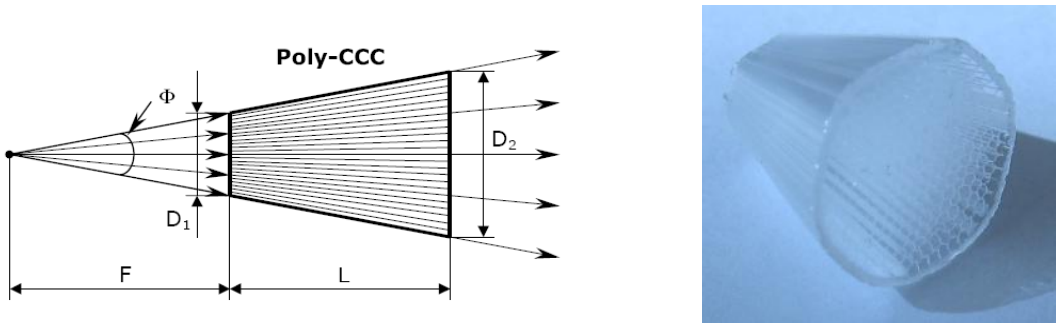

Figure 54. Schematic design and photograph of a Poly-CCC prototype structure used for table-top experiments in this study: focal length F = 11 mm, Poly-CCC length L = 12 mm, entrance aperture D1 = 5.3 mm (phantom side), exit aperture D2 = 10.5 mm (detector side), acceptance angle Φ = 25.5^{O}.

The XRF table-top system was set up with three different detectors: a low-resolution thermo-electrically cooled Si-PIN photodiode (XR-100CR from Amptek Inc, USA), with active area of 25 mm^2, and two Silicon Drift Detectors - one droplet SD^3 and one circular SDD, with active areas of about 3.5 mm^2 and 25 mm^2, respectively (C. Fiorini & A. Longoni 2008). The two SDD sensors investigated here were fabricated by the Semiconductor Laboratory of the MPI (Max Planck Institute MPI-Halbleiterlabor, Germany), in cooperation with PNsensor (PNsensor GmbH, Germany).

The Si-PIN detector included an integrated input FET and feedback elements. The internal components were kept at approximately -30 ºC, monitored by an internal temperature sensor. The XR-100CR detector was connected to a digital pulse processor (Amptek PX2), comprising a shaping amplifier (typical shaping time of 20 μs) and power supply. The shaped signals were directly fed into a multi-channel analyzer (Amptek MCA-8000A) and transferred onto a computer for spectroscopic analysis.

The SDD is a relatively new X-ray detector technology, characterized by a very low capacitance of the electrode collecting the signal, resulting in low electronic noise and good energy resolution (typically FWHM ~ 130 eV @ 5.9 KeV against 360 eV of the Si-PIN diode, both measured under same experimental conditions); figure 55 show a schematic diagram of an SDD sensor and a photograph of 5 mm^2 droplet SD^3 detector.

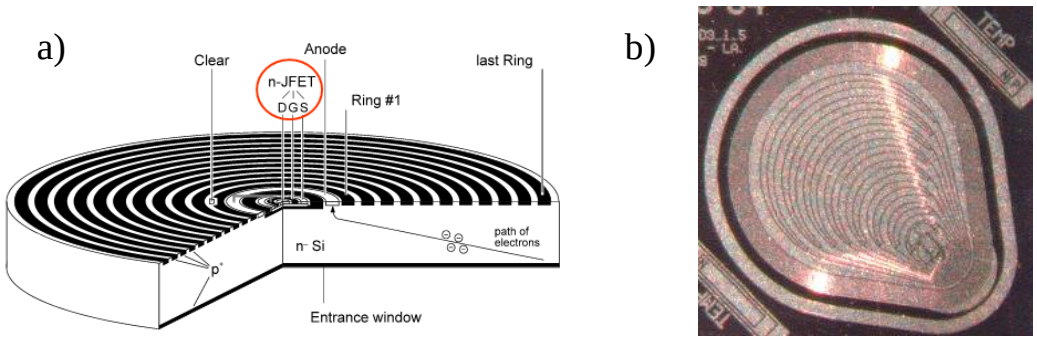

Figure 55. a) Schematic diagram of the SDD for X-ray spectroscopy with integrated n-channel JFET (Beckhoff et al. 2006). b) Photograph of the 5 mm^2 droplet Silicon Drift Detector (SD^3) with sideward positioned JFET.

The two SDD detectors have a JFET integrated directly on the detector chips and both are mounted and bonded into T08 housings. Cooling is performed with a Pelletier element (down to − 20 °C); the temperature is monitored with a sensor mounted on the chip (the Pelletier is biased with an external power supply with temperature set by the operator). The detector signal is analyzed by a hybrid CR-RC shaper, with the possibility to adjust pole-zero cancellation, shaping time (250 ns or 1 μs) and gain. Eventually, the differential shaper output is connected to a MCA

(Amptek MCA-8000A). The front-end and shaping electronics was designed and arranged by the group of Prof. Longoni of the Department of Electronics at Politecnico di Milano, in cooperation with XG-Lab (X and Gamma Ray Electronics XG-Lab, Italy).

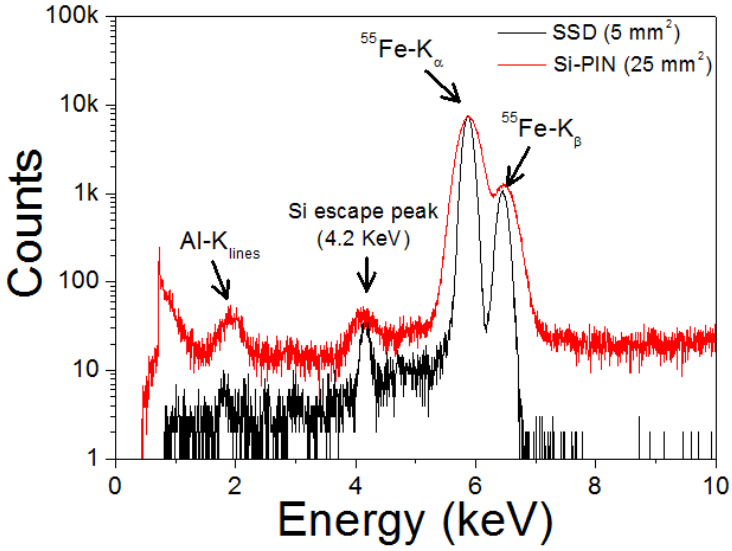

Figure 56. Example of ^{55}Fe spectra acquired with the Si-PIN diode (red line) and the SDD (black line). In both spectra the Si escape peaks are visible (at 4.2 KeV). The characteristic aluminum K_α peak corresponds to the fluorescence emissions originating from the detector housing.

Figure 56 shows a comparison between ^{55}Fe spectra, recorded with the two spectroscopic detectors under same counting rates (~1 Kcps). The SDD was operating at room temperature and with shorter shaping time (250 ns compared to 20 μs), particularly useful at high count rates; it had superior performances compared to the cooled Si-PIN diode. The energy resolutions of the SDD and the SI-PIN detector are respectively of the order of 180 eV and 360 eV (FWHM).

Notice that both spectra (figure 56), show typical low-energy tails for each characteristic emission line (in our case the 5.9 KeV ^{55}Fe-K_α line). The tail is the result of incomplete charge collection events (ICC), namely events that occur in peripheral regions of the detector where part of the created electron-hole pairs are recombined before collection at the electrodes (e.g. entrance window effect, anode effect, distorted electric field on the edge of the detector volume). The Si-PIN diode spectrum was recorded at relatively high counting rate and it shows a continuum also on the right side of the characteristic peaks - caused by pile-up.

In the case of the SDD, a continuous p+ junction implanted on the rear side of the detector acts as radiation entrance window: it follows that the effective ‘dead’ layer, at the entrance window, is below 15 nm, reducing the incomplete charge collection effect. In addition, the integrated JFET

in the droplet SD^3 configuration and the edge of the detector active area have been shielded from direct irradiation by an internal collimator made of Zirconium. In the case of the 5 mm^2 SDD, the resulting effective area of the sensor was reduced to 3.14 mm^2. Due to the shielded detector border, at room temperature the peak-to-background ratio (P/B) of this SDD was of the order 3300; this value remarkably increased to 12,000 at the optimal temperature of −20 °C; for comparison, under the same operating conditions (around −20 °C), the P/B of the Si-PIN diode was about 500 only.

The study of the two radiation detector types points at the superiority of the SDD type detector, leading to a much better sensitivity of the XRF probe per unit area of the radiation detector.

6.1.3 Prostatic phantoms

The prostatic phantoms used thought-out the entire XRF experiments consist either of:

-) a series of flat 1 mm thick foils of commercial synthetic polymer material (urethane-base resin, SZ-50 (Kyotokagaku Co., Ltd., Japan) with a mass density of 1.061 g/cm^3), containing certified Zn concentrations (0, 500, 1000 or 2000 ppm).

-) Zn-enriched water (mass density of 1 g/cm^3).

-) TE water-based solution (mass density of 1.052 g/cm^3), with composition of elements for reference man (ICRP 1975) – for details see table 4.

Table 4. Composition of the TE liquid.

Component	Canonical formula	Fraction in solution (%)
Water	H_2O	63.7
Glycerol	$C_3H_2(H_2O)_3$	28.2
Potassium Persulfate	$K_2S_2O_8$	0.3
Sodium chloride	NaCl	0.7
Urea	$CH_2N_2(H_2O)$	7.1

The urethane-based resin (SZ-50) was considered a good choice for modeling prostatic tissue, with its advantage of being stable, non-aqueous material, and largely utilized for dosimetric

applications in both planar radiography and CT scanning. Its solidity allows constructing phantoms composed of different compartments. As an example, it allows to construct multi-compartment phantoms consisting of a rectal wall (typically 3 mm thick), and a benign prostate section with high Zn in which a small region with low Zn is included, modeling the cancerous malignant lesion.

In order to speed up the measurements but avoiding significant self absorption, the benign prostate compartment was generally chosen to have high Zn content, of 2000 ppm. However, the urethane-based resin is tissue-equivalent material only for relatively high photon energy (>50 keV), where the Compton scattering effect is the dominant form of interaction. Indeed, since the Compton interaction involves essentially free electrons in the absorbing material, the Compton mass attenuation coefficient basically depends only on the number of electrons per gram (electron density). It follows that, although the electron density of elements decreases slowly but systematically with Z, most materials except hydrogen can be considered as having approximately the same electrons density and thus the Compton mass attenuation coefficient is the same for all dosimetric materials (water, soft tissue, SZ-50 - see Tab. 5). Differently, in the range of "low" photon energy (< 50 keV), where the photoelectric effect is dominant, the mass attenuation coefficient (μ/ρ) strongly depends on the atomic number of the absorbing material (namely it depends specifically on the chemical composition of the material). As shown in Tab. 6, the urethane-based resin, rich of Carbon, have smaller Z_{eff} compared to the prostatic tissue (Soft Tissue), rich of Oxygen, and it cannot be considered as tissue-equivalent in the low X-ray energy range. The photon attenuation (and similarly dose absorption) in the urethane-based resin at the low energy range (<20 keV) is definitely smaller than the one occurring in tissue-equivalent material.

Table 5. Compositions and specifications of the various materials used in the table-top experiments in comparison with the prostatic tissue.

Z_{eff} = effective photoelectric atomic number (Khan 2003)

Material	Mass density	Effective photoelectric Atomic Number	Electron Density (10^{23} e-/g)	Composition (wt%)				
				H	C	N	O	Other
Water	1	7.42	3.34	11.2			88.8	
SZ-50	1.06	6.14	3.26	8.4	72.3	4.6	14.7	
Soft Tissue	1.06	7.5	3.36	10	11.1	2.6	76.3	
Prostate	0.98	7.52	3.26	10.5	8.9	2.5	77.4	0.7

For this reason the urethane-base resin phantoms have been exclusively employed to develop and test algorithm for the reconstruction of the in-depth Zn-distribution and for acquisition and data analysis of 2D Zn-map images. Measurements on detection sensitivity, leading to the crucial computation of absorbed dose, and consequently the estimation of the radiation induced-cancer risk, were specifically and exclusively performed with tissue-equivalent phantoms made from water-based solution, to which various definite amounts of Zn have been added.

6.2. Results

6.2.1 Determination of the target-volume geometry (Sensitivity profile)

For the sake of simplicity, the shape of the target-volume has been approximated by a cylinder (see figure 57), whose base equals to the cross section of the exciting photon beam (πR^2) and its length is dictated by the sensitivity profile and the incident angle of the primary photon beam (θ). The dimensions of the target-volume can then be computed as:

$$V_{T\text{-}V} = \frac{L}{Cos(\theta)} \pi R^2 \qquad (6.2)$$

where L is the in-depth length of the sensitivity profile.

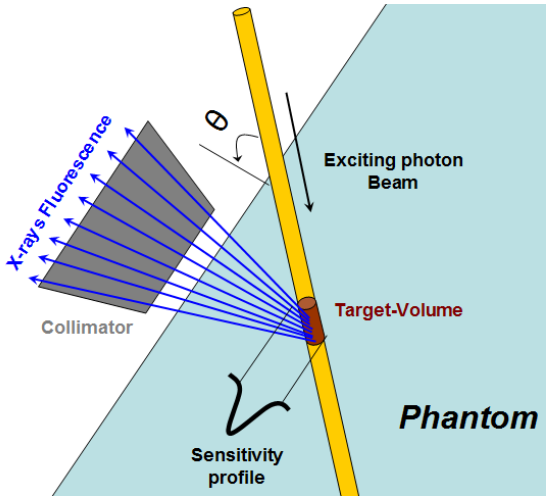

Figure 57. Schematic drawings of the target-volume geometry resulting from the overlap of the primary photon beam and the solid angle given by the collimator.

The sensitivity profile is the intensity curve of the recorded fluorescence radiation emitted by a thin (100 μm) Cu foil moved through the beam; its displacement through the target-volume results in a Gaussian distribution of the fluorescence-line intensity, corresponding to the extension of the target-volume along the depth direction. Notice that, for fluorescence emitted by a thin Cu foil, the self-absorption may be indeed considered negligible and the Cu-K_α fluorescence count profile $\Phi(z)$ can be formally computed as:

$$\Phi(z) = T\, I_0\, \sigma_F\, Q\, \eta(z) \tag{6.3}$$

where T is the irradiation time (sec), I_0 is the flux of the impinging excitation radiation (phot/sec), σ_F is the production cross section (cm^2/g) for the Cu-K_α emission (defined as the product of the photoelectron cross section for Cu, calculated at the exciting photon beam energy of 18 keV, and the fluorescence yield for Cu-K_α line emission), Q is the mass concentration of the element under study in the sample (g/cm^2) and $\eta(z)$ is the dimensionless sensitivity profile we wish to measure.

Figure 58 depicts the sensitivity profiles measured with the Poly-CCC paired with the 30 mm^2 Si-PIN diode (similar profile was obtained with the 25 mm^2 SDD) and with the 3.5 mm^2 SD^3 detector. The distributions were obtained by recording the Cu-K_α peak intensity at each location, in 0.2 mm steps and the experimental data were fitted with asymmetric double sigmoidal function. The sensitivity profile was characterized by a FWHM of the order of 1.7 mm and 1.45 mm respectively for the 30 mm^2 Si-PIN detector and the 3.5 mm^2 SD^3 detector. As a result, according to Eq. 1, the sizes of the inspected volume are 1.34 mm^3 and 1.2 mm^3, respectively.

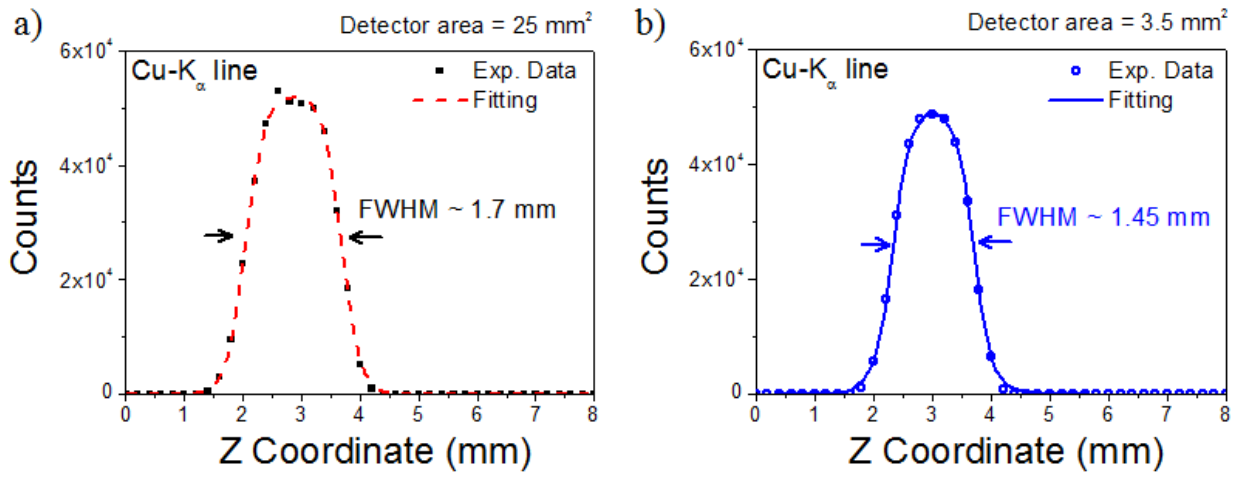

Figure 58. Sensitivity profiles obtained by moving a 100 μm thick Cu foil along the detector axis coordinate (Z Coordinate). In part a) the Poly-CCC was paired with 25 mm^2 (Si-PIN/SDD) X-rays detector while in part b) with 3.5 mm^2 SD^3. The experimental data were fitted with asymmetric double sigmoidal function.

6.2.2 Sensitivity

The sensitivity of the XRF detection system is defined as the number of recorded Zn-fluorescence counts (K_α peak), per number of impinging excitation photons and per average concentration of Zn in the target volume (ppm):

$$\text{Sensitivity} = \frac{\text{Detected Zn Fluorescence}}{(\text{ppm of Zn})(\#\text{ of exciting photons})} = \frac{\text{Counts}}{\text{ppm photons}} \tag{6.4}$$

The detection sensitivity depends on:

-) the collimator design and the resulting quality (size, sharpness) of the target volume;

-) the energy spectrum of the incident radiation;

-) the active area of the spectroscopic X-ray detector;

-) the energy resolution, efficiency and signal-to-noise ratio (SNR) of the spectroscopic X-rays detector;

-) the background produced from scattering of the incident radiation or from regions surrounding the target volume;

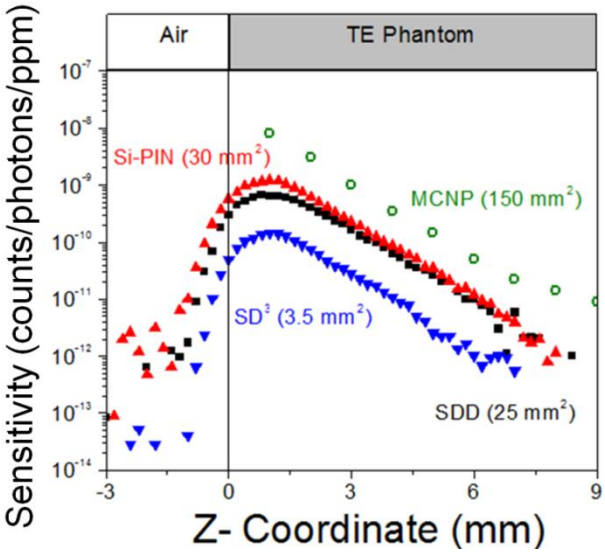

Figure 59. Detection sensitivities (counts/ppm/photons) as function of irradiation depth measured in TE phantoms (water solution with 620 ppm of Zn) with Poly-CCC paired with detectors of various effective area: 3.5 mm² SD³ (blue curve), 25 mm² SDD (black curve) and 30 mm² SDD (red curve). Measurements were performed with the XRF set-up of figure 51, with irradiation times of 3000 sec. The experimental results are compared to calculations made with simulation with a large area (150 mm²) detector (green symbols).

The experimental assessment of the detection sensitivity as function of the irradiation depth (sensitivity profile) was performed by recording the number of Zn-K_α counts (integration of Zn-K_α peak) during an in-depth scanning of homogenous TE phantoms; the latter consisted of water solution containing 620 ppm of Zn. The resulting count profiles were used as input for Eq. 4, after background subtraction, from which the sensitivity profile was derived (see figure 59). Figure 59 also depicts simulated sensitivity vs irradiation depth projected for a 150 mm^2 spectroscopic detector preceded by a Poly-CCC; this system could fit in a future prostatic probe.

In all the graphs in figure 59, the irradiation depth is defined as the distance between the centroid of the sensitivity profile (namely the profile of the target-volume along the in-depth direction – see paragraph 6.2.1) and the surface of the inspected phantom.

Figure 60 illustrates examples of spectra obtained with the three different detectors - 5 mm^2 SD^3 (blue curve), 25 mm^2 SDD (black curve) and 30 mm^2 Si-PIN diode (red curve), at an irradiation depth of 2 mm and under the same experimental conditions as in figure 59. It is evident from these spectra that the background recorded in the region of the Zn-K_α peak is due to a tail from the elastic scattering peak; it originates from incomplete charge collection (ICC) in the detector and it represents the principal limitation of Zn detectability in the analyzed matrix.

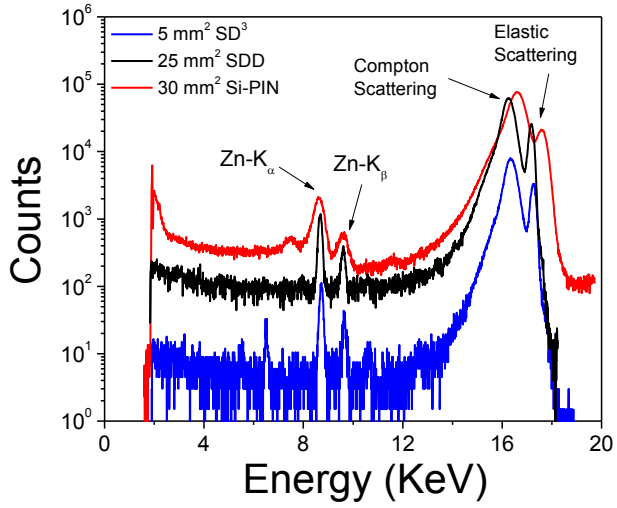

Figure 60. Example of spectra obtained by scanning a water phantom (620 ppm of Zn) at irradiation depth of 2 mm with Poly-CCC and various effective area detectors: 5 mm^2 SD^3 (black curve), 25 mm^2 SDD (blue curve) and 30 mm^2 Si-PIN (red curve).

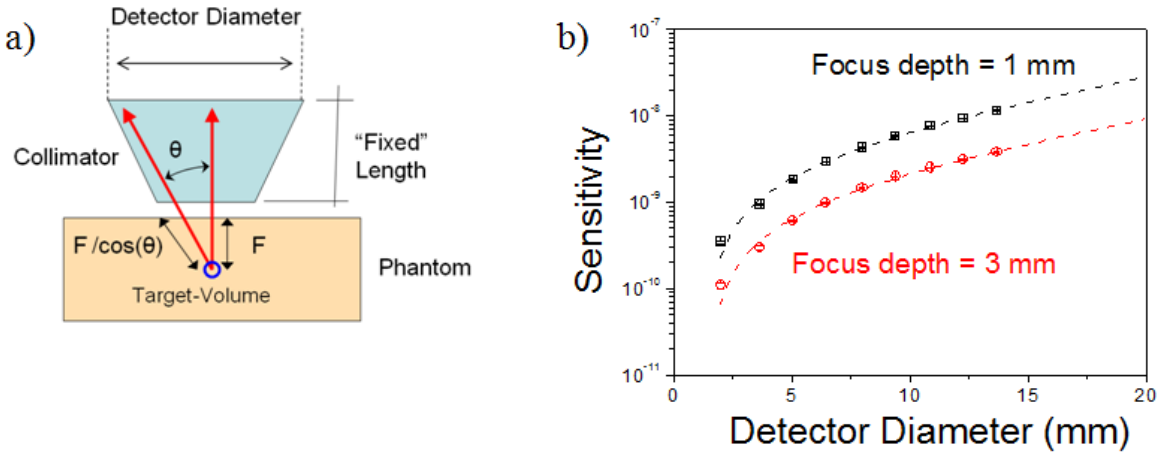

Figure 61. Part a): Simulation geometry: fluorescence radiation generated in the target-volume and emitted at an angle θ relative to the collimator axis has a longer path within the phantom and suffers more attenuation. Part b): sensitivity (counts/ppm/photons) of the detection system as function of the detector diameter computed by MNCP simulations, assuming irradiation at two different focal depths.

Note that radiation emitted from the target volume and directed at an angle θ towards the edge of the detector has a longer path inside the sample, and thus larger attenuation compared to the radiation travelling along the detector axis (see Figure 61a). As a result, the detection sensitivity in not uniform across the detector area but it has a maximum at its center, and decreases towards the edges. It may also result in a non linear increase of the sensitivity with the detector surface. This was demonstrated by a series of MCNP simulations of detection sensitivity as function of the diameter of the detector (figure 61b). The simulations assumed a conical collimator (figure 61a), with a fixed length (10 mm) and a fixed focus (10 mm); sensitivity was computed for various detector diameters at two different focal depths (F=1 mm and 3 mm). It follows that, for small detector area (< 20 mm^2) the sensitivity increases rapidly with the detector diameter, and for larger detector diameter the increase is proportional to the surface.

Figure 62 shows the sensitivity (MCNP simulations), calculated at an irradiation depth of 3 mm, as function of the detector effective area. The computer-simulated detector is preceded by a poly-capillary conical collimator (10 mm length); experimental data measured with our present systems were added as well.

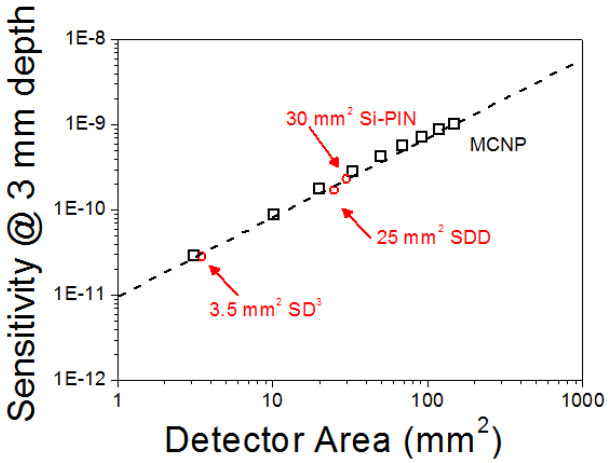

Figure 62. Sensitivity (counts/ppm/photons)computed by MCNP at 3 mm irradiation depth, vs. effective area of the spectroscopic detector, preceded by a 10 mm long poly-CCC. Measured data with present Poly-CCC coupled to the 30 mm^2 Si-PIN diode, 25 mm^2 and the 3.5 mm^2 SD^3 sensors are provided as well.

Note that in our application, the detector area is limited by the dimensions of the probe housing (maximum probe's external diameter is 3 cm). Considering also the structure and dimensions of commercial SDD sensors, best suitable for this application on the basis of requests and performances, we estimated that we can accommodate a detector of maximal size of ~150 mm^2. Therefore, the simulations permitted assessing the expected sensitivity of a practical detector system for a prostatic probe (figure 59).

6.2.3 Limit of Detection (LOD)

The spectroscopic accuracy and the capability to measure small concentration of Zn in TE sample, based on analysis of XRF spectrum, may be formally characterized by the introduction of the limit of detection (LOD). The LOD is commonly defined as the lowest quantity of a substance (expressed in concentration C_L) that can be distinguished from the absence of that substance (a blank value) within a stated confidence limit, under given experimental conditions (sample geometry, sample matrix, irradiation time, etc.). According to the International Union of Pure and Applied Chemistry (IUPAC) recommendations (Currie 1995), the LOD has been defined using the following formula:

$$LOD = k \frac{C}{I_{Zn}} \sqrt{\frac{I_{BK}}{T}} = \frac{k}{m} \sqrt{N_{BK}} \qquad (6.5)$$

where k is a constant known as "k-value"; T is the irradiation time; $I_{BK} = N_{BK}/T$ is the average background count rate and correspondingly N_{BK} is the total count of the background; $I_{Zn} = N_{BK}/T$ is the net count rate of the characteristic Zn-K_α line emission and correspondingly N_{Zn} the total net Zn-K_α counts; C is Zn concentration (in ppm) of the sample. It follows that $m = N_{ZN}/C$ is the slope of the net Zn-K_α counts/concentrations curve (expressed as counts/ppm). The IUPAC recommends that the k-value should be 3, corresponding to a confidence level of about 95% (Currie 1995; Jenkins & Gilfrich 1992).

As the LOD depends mainly on two instrumental parameters, namely the background intensity I_{BK} and the net intensity per unit analyzed mass (namely sensitivity), it follows that, given a specific instrumental sensitivity and a spectroscopic detector with a characteristic peak-to-background ratio (P/B), the optimization of the XRF measurement is accomplished by a tradeoff between the irradiation time and LOD. Indeed, long irradiation time improves the accuracy of the Zn value determination (small LOD value and better precision) but it induces a higher absorbed dose delivered to the patient. Following the same arguments, with a fixed irradiation time and defined collimator structure (which gives the sensitivity of the method), a better detector with higher SNR allows to reach lower LOD value.

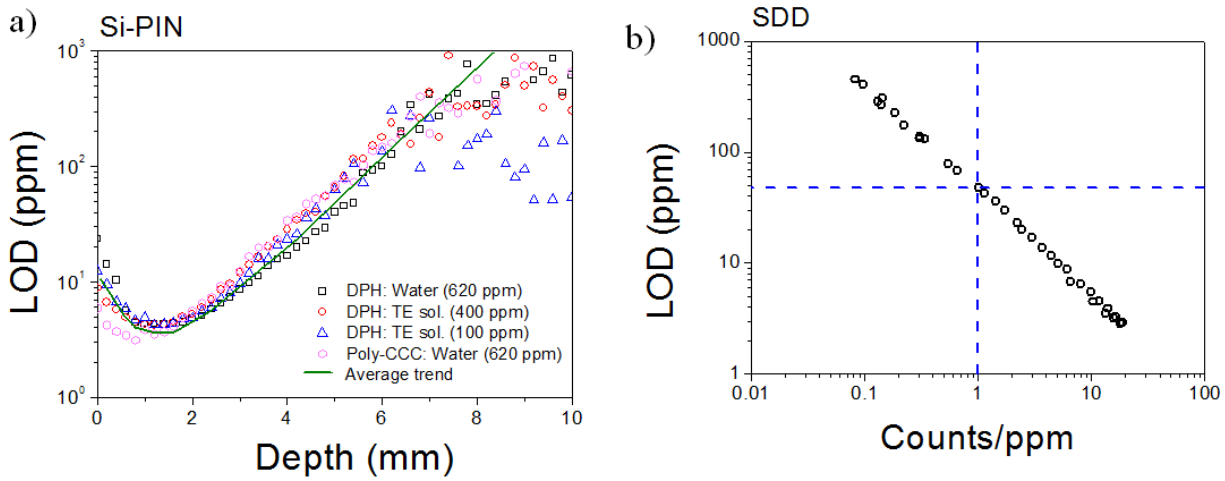

Figure 63. Part a) LOD as function of depth of the target volume in TE phantoms with irradiation time of 6000 seconds, obtained with the double pin-holes (DPH) and Poly-CCC experimental set-up. The average trend (green line) is also shown. Part b) depicts LOD as function of counts/ppm.

Figure 63a illustrates the LOD obtained from the analysis of spectra recorded at different depth, irradiating TE phantoms (water and TE solution containing 620 ppm, 400 and 100 ppm of Zn respectively), with the double pin-holes and the Poly-CCC experimental arrangements, both coupled to a 25 mm^2 Si-PIN detector. The LOD increases exponentially with the irradiation depth;

the measurement's precision deteriorates with depth as a result of a significant increase of LOD and counting error.

For a given detection system with known sensitivity profile, we can calculate the total number of exciting photons ($N_{Ex\text{-}Pho}$) required to achieve a certain level of accuracy (LOD), using the following expression:

$$N_{Ex\text{-}Pho}(x) = \frac{m}{Sensitivity(x)} \tag{6.6}$$

While the sensitivity depends predominantly on the collimator design, the level of accuracy requested for the determination of Zn concentration is dictated by the factor m, which is the number of Zn net counts per ppm of Zn in the target volume, and by the performance of the spectroscopic detector. It should be stressed that the background under the Zn characteristic emission line, which is a property of the detector, is a major factor influencing the precision with which the peak net counts are evaluated. Figure 63b shows the relation between the LOD and the factor m (counts/ppm), computed as based on the sensitivity profile of a detection system comprising of Poly-CCC paired with the 5 mm^2 SDD sensor. For example, it turned out that for 1 count/ppm of net Zn-K_α the LOD is around 50 ppm at a depth of 5 mm. Notice that this level of accuracy is achieved with a small collimator and a small area detector. With equal irradiation time, a larger SDD sensor, preceded by a suitable Poly-CCC, will increase the sensitivity in proportion to the sensor's surface increase, with a foreseen better background. This will permit to reduce the total amount of irradiation to a reasonable level (within permissible dose and reasonable irradiation time) allowing to reach an acceptable level of measurement accuracy.

6.2.4 Algorithm for the reconstruction of the elemental distribution in a phantom

XRF-based tomography is capable of delivering three-dimensional images of the elemental distribution in a sample, but it requires a suitable calibration algorithm for converting the detected fluorescence counts rate into the elemental concentration.

A mathematical model and a suitable algorithm for the reconstruction of the elemental composition of a multi-compartments phantom have been developed and presented in this section. The approach is based on the theoretical expression for the primary X-rays fluorescence intensity emitted in the target-volume as function of the probing depth. It includes parameters characterizing

the target-volume, the properties of the irradiated specimen and the thickness of the specimen strata. However, the approach neglects scattering effects and possible secondary fluorescence.

In the case of the target-volume moving through a thick sample, the attenuation of both exciting f_{Att}^{E} and fluorescent radiation f_{Att}^{F} has to be included, via the factor $\left[f_{Att} = f_{Att}^{E} + f_{Att}^{F}\right]$. The Eq. 6.3, describing the intensity profile in thin sample (see paragraph 6.2.1), may be rewritten as:

$$\Phi(z) = T\, I_0\, \sigma_F \int_{-\infty}^{+\infty} \eta(z-y)\, \rho(y)\, f_{Att}(y)\, dy \tag{6.7}$$

where the quantity $\rho(y)$ is the mass density (g/cm^3) of the fluorescence trace elements whose weight fraction in the bulk sample we aim to evaluate, $\eta(z)$ is the sensitivity profile provided by the collimator system (defined in paragraph 6.2.1).

The mathematical expression of f_{Att} is extremely problematic, since it specifically depends on the complex geometrical structure of the target-volume and its depth in the analyzed sample, on the radiation energies and direction of the exciting and fluorescent beam, on the phantom density and on the solid angles seen by the detector through the collimator structure. However, one may describe the attenuation of the primary and fluorescence radiation in a compact and simple expression, using an exponential function model containing an effective linear attenuation coefficient $\left(\overline{\mu}_{lin}\right)$.

$$f_{Att} = \exp\left(-\overline{\mu}_{lin}\, z\right) \tag{6.8}$$

The effective linear attenuation may be computed either from a calibration depth profile obtained by scanning a homogeneous phantom, taken as calibration sample, and with known elemental composition (alpha-coefficient method), or from Monte Carlo simulation. We assume that the effective linear attenuation coefficient depends only on the chemical composition of the bulk (soft-tissue model) and it is not affected by variation of the fluorescent element under investigation (whose weight fraction is considered to be negligible). Eventually, Eq. 6.7 may be rewritten as:

$$\Phi(z) = T\, \Phi_0\, \sigma_F \exp\left(-\overline{\mu}_{lin}\, z\right) \int_{-\infty}^{+\infty} \eta(z-y)\, Q(y)\, dy \tag{6.9}$$

Once the effective linear attenuation coefficient has been introduced, the intensity curve $\Phi(z)$ from any phantom (with the same bulk composition of the calibration sample) may be corrected for radiation attenuation. The corrected intensity profile is mathematically defined as:

$$\Theta(z) = \frac{\Phi(z)}{\exp\left(-\overline{\mu}_{lin}\, z\right)} = T\, \Phi_0\, \sigma_F \int_{-\infty}^{+\infty} \eta(z-y)\, Q(y)\, dy \tag{6.10}$$

The elemental mass density composition Q(z) may now be straightforwardly calculated by convolving the corrected intensity profile Θ(z) and the sensitivity profile η(z).

$$Q(z) = T\,\Phi_0\,\sigma_F\,\mathrm{Conv}\left\{\Theta(z),\eta(z)\right\} = T\,\Phi_0\,\sigma_F\,\mathrm{Conv}\left\{\frac{\Phi(z)}{\exp(-\bar{\mu}_{lin}\,z)},\eta(z)\right\} \tag{6.11}$$

Nowadays, many deconvolution algorithms have been developed, offering a range of possible signal processing methodologies. However, generally, most of the deconvolution algorithms do not work properly for noisy measurements; poor instrumental signal-to-noise ratio degraded the calculation of the deconvolved signal. If we have at least some knowledge of the type of noise in the data, we may be able to improve the computation through suitable filtering techniques. A widely used solution is offered by a Bayesian-based iterative algorithm, known as Richardson-Lucy (RL) deconvolution approach; it was originally introduced in the field of image processing for the extraction of a latent image from an experimentally measured intensity distribution, which contains some random noise - Poisson noise statistics (Richardson 1972).

$$Q(z) = T\,\Phi_0\,\sigma_F\,\mathrm{RL}\left\{\Theta(z),\eta(z)\right\} = T\,\Phi_0\,\sigma_F\,\mathrm{RL}\left\{\frac{\Phi(z)}{\exp(-\bar{\mu}_{lin}\,z)},\eta(z)\right\} \tag{6.12}$$

An alternative approach to the deconvolution computation is to make use of an unfolding-like technique, where the intensity profile Φ(z) is expresses as a linear combination of the intensity responses $\Lambda_i(z)$ provided by the i-th stratum multiplied by a coefficient $\xi_i \in [0,\infty]$ proportional to the elemental concentration of that stratum multiplied by a proper attenuation factor (the latter depends on the depth of the stratum in the phantom).

With this method, the effects of random noise are strongly reduced by lowering the spatial resolution of the XRF scanning: indeed the method calculated the average elemental concentration over a length (length of the stratum - 1 mm in our experiment), which is larger than the actual step of the measurement (0.2 mm). We may formally write:

$$\Phi(z) = \xi_1\,\Lambda_1(z) + \xi_2\,\Lambda_2(z) + \ldots + \xi_N\,\Lambda_N(z) = \sum_{i=1..N}\xi_i\,\Lambda_i(z) \tag{6.13}$$

The responses $\Lambda_i(z)$ may be experimentally determined using some calibration phantoms with known elemental composition or by a series of Monte Carlo simulations (figure 64).

The estimation of the corresponding parameters ξ_i is achieved by solving the least square problem:

$$\min_{Q_i \in [0,\infty]}\left(\Phi(z) - \sum_{i=1..N}\xi_i\,\Lambda_i(z)\right) \tag{6.14}$$

Eventually, assuming the sample is homogeneous in density and the elemental concentration is small enough such that the effective linear attenuation coefficient depends only on the bulk composition (soft tissue), then the elemental concentration of the i-th stratum is calculated as:

$$Q_i = \frac{\xi_i}{\exp(-\overline{\mu}_{lin}\, z_i)} \tag{6.15}$$

where z_i is the "median" depth of the stratum in the phantom. If we denote h as the thickness of a stratum, we may write

$$z_i = \frac{h}{2} + (i-1)h \qquad \text{for } i = 1, 2, 3, \ldots \tag{6.16}$$

The general methodology, described above, can be applied for the reconstruction of the concentration distribution of any element, whose characteristic fluorescence lines are of energy lower than the incident photon radiation.

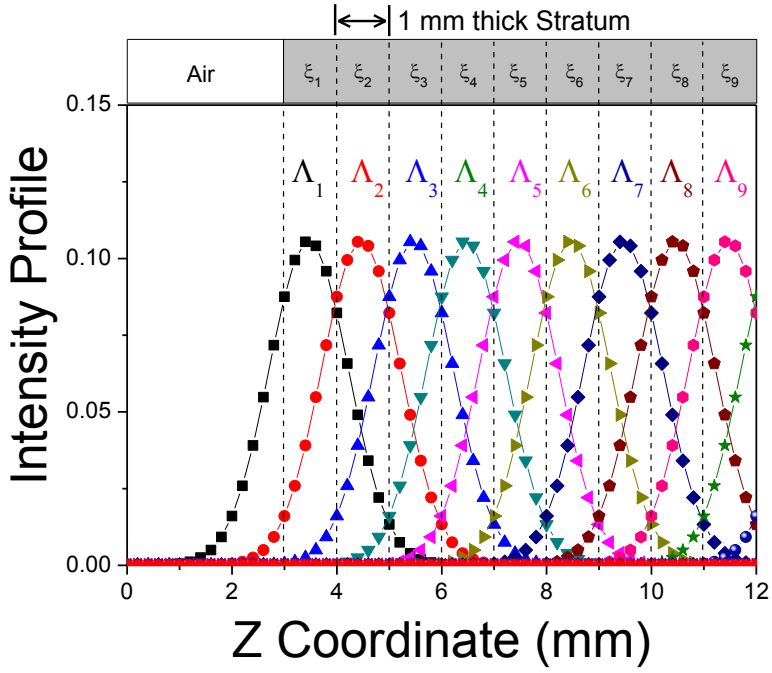

Figure 64. Schematic representation of the intensity responses from the various phantom strata.

The method may be equally applied for the reconstruction of the mass density profile, based on the intensity profile of the integrated Compton peak. Indeed, as mentioned early, the Compton mass attenuation coefficient is directly proportional to the number of electrons per gram; assuming the analyzed sample has homogeneous bulk chemical composition (soft tissue), then it follows that the Compton cross section is also (directly) proportional to the average mass density of the sample. However, in this case, the computational algorithm needs a slight modification since the attenuation

factor for the i-th stratum depends on the mass density of the preceding strata. Using an iterative approach, the mass density profile of all the strata may be determined from solving the following system of equations (6.17):

1^{st} stratum → $$Q_1 = \frac{\xi_1}{\exp\left(-\frac{\overline{\mu}_{lin}}{\rho_0} Q_1 \frac{h}{2}\right)}$$

2^{nd} stratum → $$Q_2 = \frac{\xi_2}{\exp\left(-\frac{\overline{\mu}_{lin}}{\rho_0} h\left(Q_1 + \frac{Q_2}{2}\right)\right)}$$

…..

i^{th} stratum → $$Q_i = \frac{\xi_i}{\exp\left(-\frac{\overline{\mu}_{lin}}{\rho_0} h\left(Q_1 + ... + Q_{i-1} + \frac{Q_i}{2}\right)\right)}$$

where ρ_0 is take reference mass density (for soft tissue and SZ-50 is equal to 1.06 g/cm^3) and the ratio $\left(\overline{\mu}_{lin}/\rho_0\right)$ correspond to the effective mass attenuation coefficient of the bulk material.

-) Reconstruction of the mass density profile

Figure 65a shows an example of an energy spectrum recorded during 3000 seconds irradiation of a homogeneous SZ-50 phantom (mass density of 1.06 g/cm^3), at a depth of 5 mm from the phantom surface; the highlighted green area corresponds to the Compton peak of the exciting radiation (~18 keV, Mo-K_α line). The spectrum was obtained with the set-up shown in figure 51.

Figure 65b depicts the Compton-peak intensity profile (0.2 mm step) of the homogeneous SZ-50 phantom (up to 9 mm in depth) taken as calibration sample. The recorded Compton peak intensity increases from left to right, when the target-volume moves from outside to inside the phantom and decreases again due to absorption. In figure 65b is also shown the fitted exponential model function (red line) used to compute the effective linear attenuation coefficient $\mu_{Mo(K\alpha)}$; the value of $\mu_{Mo(K\alpha)}$ = 1.76 cm^{-1} is also confirmed by MCNP simulations.

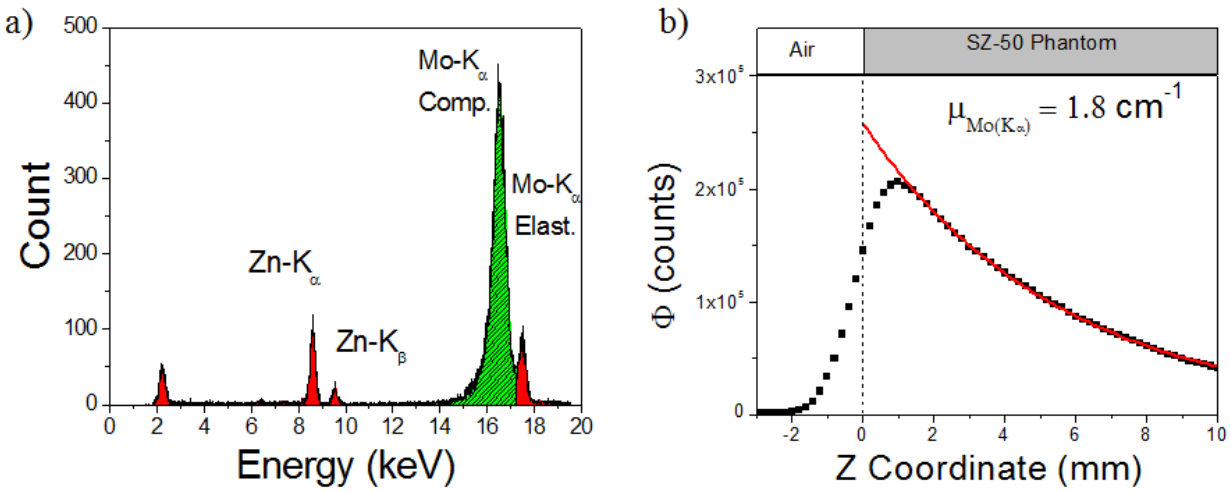

Figure 65. Part a) shows an example of an XRF spectrum recorded during 3000 seconds irradiation of a homogeneous SZ-50 phantom containing 2000 ppm of Zn, at a depth of 5 mm from the phantom's surface. Part b) shows the Compton-peak intensity profile (Mo-K$_\alpha$ 17.4 keV – green ROI in part a) resulting from depth-scanning of the prostatic phantom. The exponential fitting curve (border effect excluded), for the calculation of the effective linear attenuation coefficient, is also shown.

Figure 66 shows the "corrected" intensity profile Θ(z) of the homogeneous calibration phantom calculated for the Compton peak: it shows a flat (plateau) curve corresponding to the constant mass density profile.

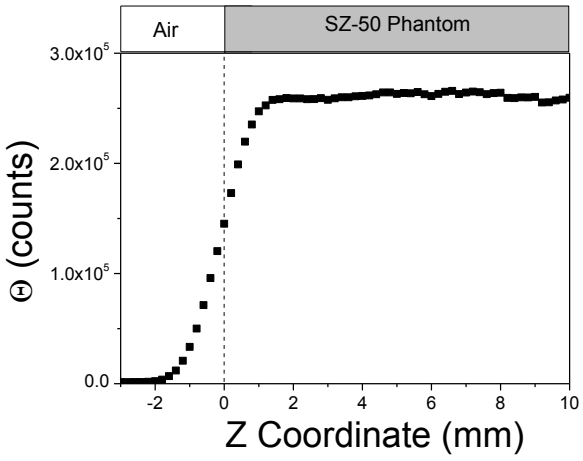

Figure 66. Compton-peak intensity profile corrected for absorption effect.

The curve of fig 65 is actually the result of folding the sensitivity function with a step function, representing a homogenous phantom. Therefore, the first derivative of the "corrected" intensity profile Θ'(z) (figure 67) is the sensitivity profile of the detection system centered at the

phantom surface (z = 0 mm), which in this case came out with a slightly larger FWHM (1.8 mm instead of 1.6 mm).

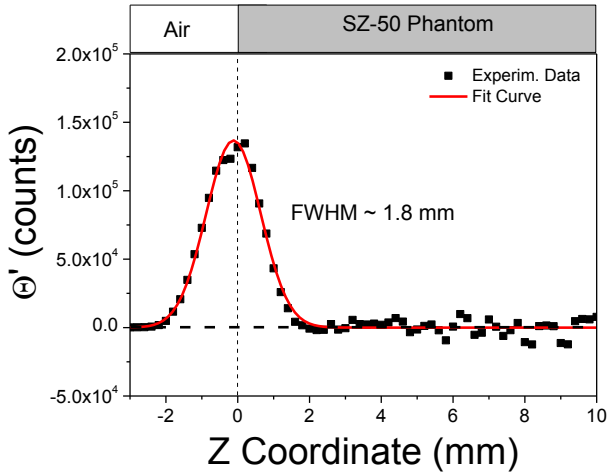

Figure 67. First derivative of the curve depicted in part figure 66, corresponding to the sensitivity profile function (i.e. target-volume depth length).

Following the prescription described above, the final step of the reconstruction process is achieved by solving the least square problem Eq. 6.14 and the system of equations Eq. 6.17.

Figure 68a depicts the mass density profile (average density = 1.06 g/cm^3), obtained with the unfolding reconstruction algorithm (bar plot) and with the 10-iterative cycles of Richardson-Lucy deconvolution (blue-line plot). Figure 68b shows the intensity profiles Φ(z) obtained from experimental data (figure 65b) compared to the one obtained from the unfolding reconstruction algorithm; the agreement is excellent.

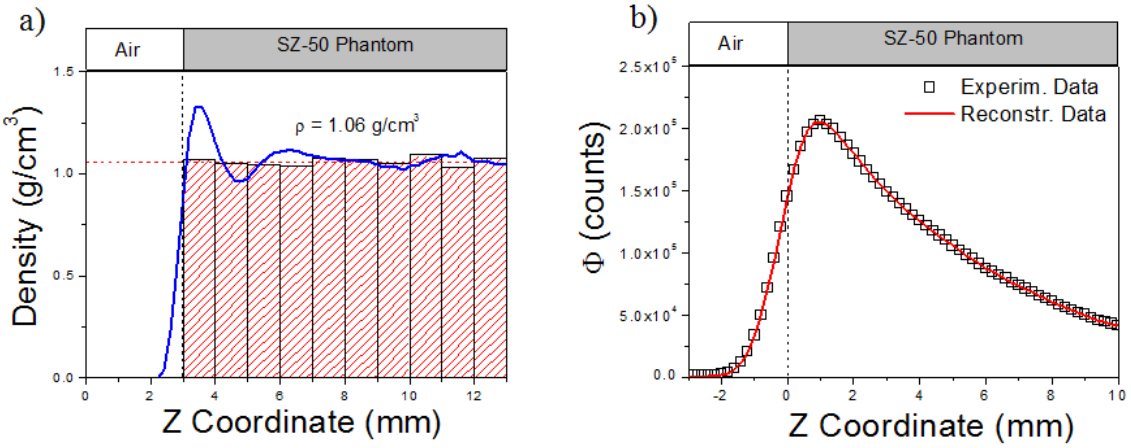

Figure 68. Part a) depicts the mass density of the various phantom strata calculated using the unfolding algorithm. Part b) shows the comparison between corrected intensity profile obtained by experimental data (black symbols) and the one obtained by the reconstruction algorithm.

As clearly evident in figure 68a, the reconstruction of the mass density profile using standard FFT-based Richardson-Lucy deconvolution is not perfectly accurate. Indeed, the use of the FFT implicitly assumes a periodic continuation of the input signals in its entire domain; as a consequence, discontinuities, appearing at the boundaries, generate Gibbs oscillations (sometimes called ripples), which degrade the quality of the reconstruction prevailingly.

The RL deconvolution method is not an appropriate analytic methodology for systematic analysis of stratified phantoms, since it contained discontinuities going from one stratum to another, but it may be effectively employed for analysis of sample with continuous and smooth distributions, like in the *in-vivo* XRF analysis of prostatic tissue.

-) Reconstruction of the Zn content

The reconstruction of Zn concentration in a stratified phantom is obtained from the analysis of the intensity profile $\Phi(z)$, which in turn can be computed by integration of the characteristic Zn-K_α peak (8.6 keV) – see enlighten green energy range (centered at 8.6 keV) in the spectrum of figure 69a. Figure 69b illustrates the resulting Zn-K_α intensity profile (and extrapolated effective linear attenuation coefficient) form the SZ-50 phantom (homogeneous distribution of 2000 ppm of Zn) taken as calibration measurement (as previously specified, scanning step is of 0.2 mm).

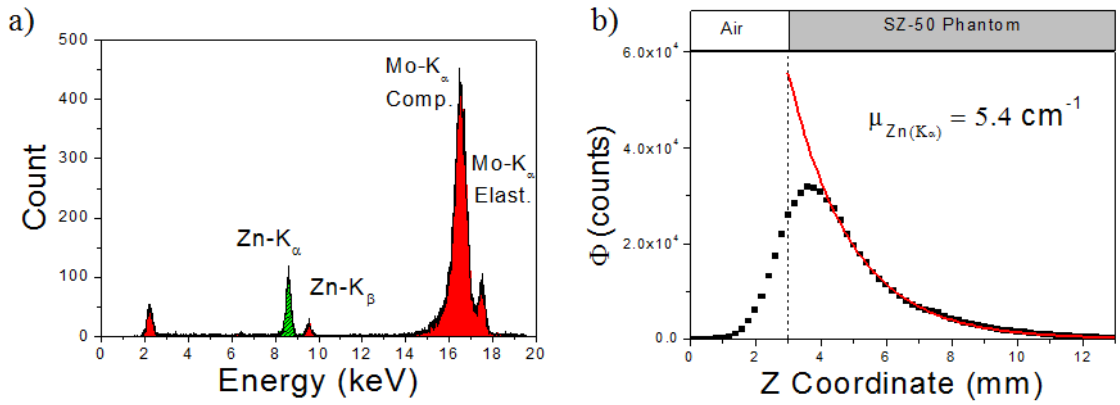

Figure 69. Part a) shows an XRF spectrum recorded irradiating a homogeneous SZ-50 phantom containing 2000 ppm of Zn (calibration phantom), for 3000 seconds and at a depth of 5 mm from the phantom's surface. Part b) depicts the Zn intensity profile Φ(z) of the calibration phantom calculated using the unfolding algorithm.

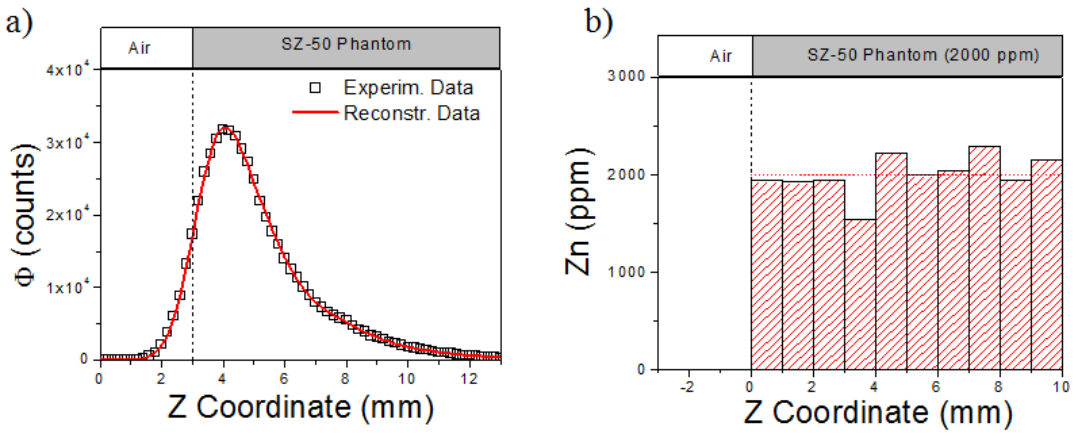

Figure 70. a) Zn intensity profile Φ(z) of the calibration phantom calculated using the unfolding algorithm (red line) in comparison with experimental data (black symbols). b) Reconstructed Zn concentration of the calibration phantom strata.

The reconstructed Zn-K_α intensity profile by the unfolding algorithm and the related Zn distribution strata of the calibration sample is shown in figure 70a and figure 70b respectively. The agreement between experimental data and reconstructed intensity profile is excellent; however, the graph in figure 70b shows a large variance in the Zn concentration calculated for the various strata (standard deviation of 7.3%), which otherwise is supposed to be homogeneous. This large discrepancy is mainly due to an intrinsic inhomogeneity of the SZ-50 phantom strata (estimated around 3%), due to instrumental uncertainties (counting statistics and instrumental accuracy) and factual errors introduced by the unfolding algorithm.

The validation of the quantitative Zn reconstruction for stratified phantoms was investigated using different multi-compartment phantoms; they consisted of healthy prostatic-like compartments (2000 ppm of Zn) containing a small inclusion with reduced Zn concentration (either 0 or 1000 ppm). Figure 71 part a) and part b) depict the Zn-K_α intensity profile and "corrected" intensity profile form homogeneous phantom in comparison with the multi-compartments phantoms. In figure 71 part c) and part d) the reconstructed Zn profile for phantom with 0 ppm and 1000 ppm test compartment are shown respectively.

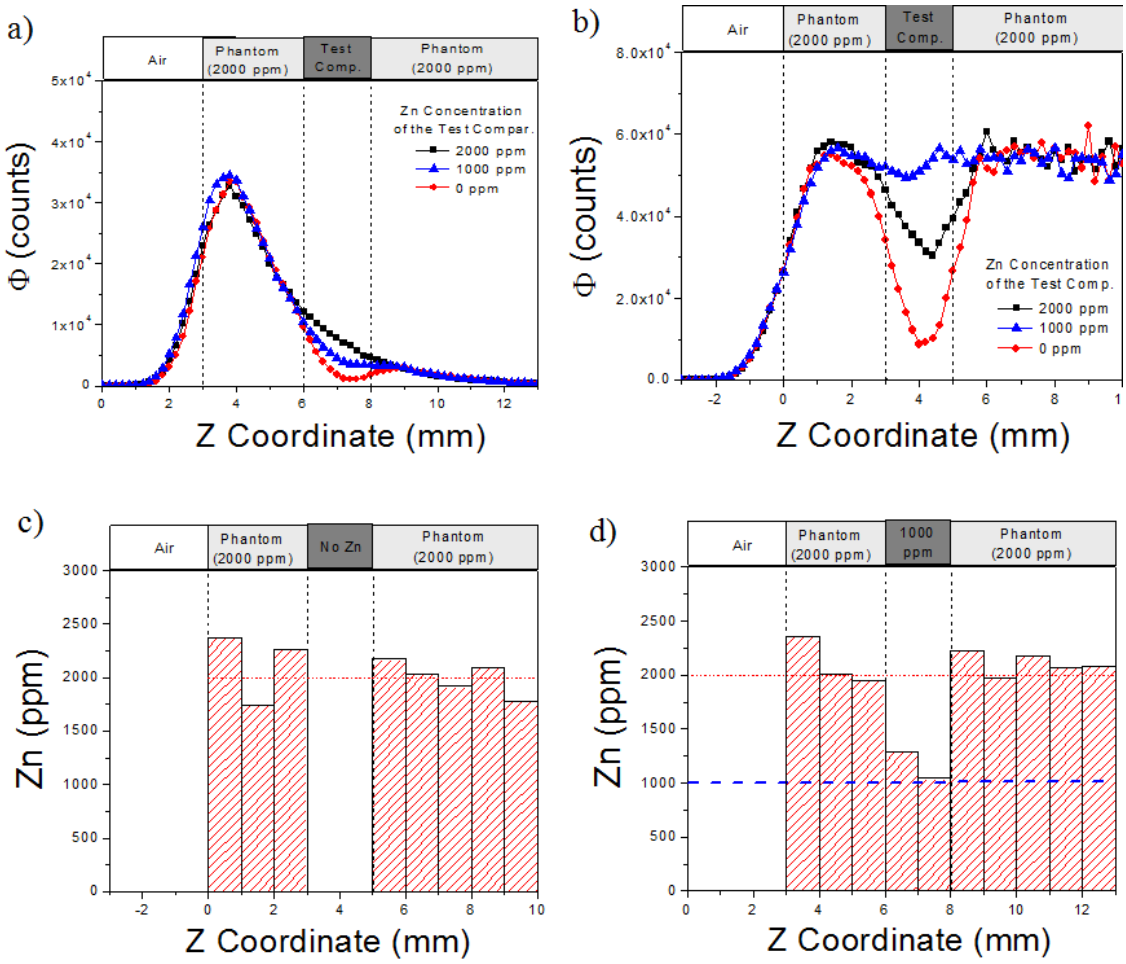

Figure 71. Intensity profile (part a) and corrected intensity profile (part b) of stratified phantom of 2000 ppm containing a compartment (2 mm) with reduced Zn concentration (either 0 and 1000 ppm). Part c) and part d) show the computed Zn distribution in the various strata of the phantom.

6.2.5 Scattering contribution to the detected XRF intensity

A great effort has been devoted to design a collimation system that will minimize the scattering contribution to the sensitivity. The multi-conical collimator (Multi-CCC) structure proposed and discussed in chapter 5 was intended to satisfy this condition. The MCNP simulation study showed that indeed, in the Multi-CCC, the scattering contribution due to a uniform distribution of Zn in the prostatic compartment increases with the depth of the sensitive volume, but, it is quite small for the relevant irradiation depths (it is less than 15% up to 7 mm in depth).

The MCNP results from computer simulation was validated by an experiment under the same conceptual scheme: a sample composed of two SZ-50 compartments, namely a 1 mm thick layer doped with 1000 ppm of Zn, immersed within a homogeneous compartment with no Zn (a

stack of 1 mm thick layers of undoped SZ-50), was investigated using a detection system comprised of a Poly-CCC and the SDD sensor. The various Zn-fluorescence measurements were carried out at a fixed irradiation depth (the target-volume was centered at a depth of 7 mm), moving the Zn-enriched layer at different position in the undoped compartment. For each measurement the sample was irradiated for 6000 seconds. This procedure allows evaluating the contribution to the sensitivity from the entire volume of the irradiated sample (figure 72).

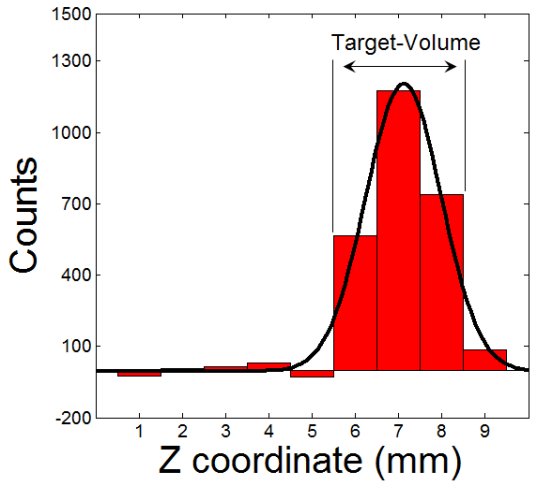

Figure 72. Contribution to the sensitivity from the various layers (1 mm thick) of the irradiated phantom, measured with Poly-CCC paired with SDD sensor. The phantom is made of SZ-50 polimer.

As shown by figure 72, basically the entire fluorescence signal comes from the target-volume, while the fluorescence originating from scattered radiation in the region preceding the target-volume is practically negligible, and actually within counting statistics. The MCNP data show a larger scattering contribution to the sensitivity, not observed experimentally, probably due to the fact that MCNP simulation used TE phantom (the above experiment was carried with SZ-50 material) and a simulated detection system with a much larger solid angle.

In the above calculations, and corresponding experiment, the contribution to the sensitivity form the rectal wall has been disregarded. However, as reported by (Tipton & Cook 1963), the amount of Zn in the various parts of the intestine is small but not negligible, being in the rectum-intestine of the order of 20 ppm, namely around five-six times below the Zn-level in normal prostatic tissue. The presence of a small amount of Zn in the rectal wall may also affect the sensitivity and detection limits. Indeed the significant amount of primary radiation, scattered towards the rectal wall (see the large coherent/Compton peaks of exciting radiation in the spectrum of detected radiation in figure 69a), may excite Zn contained in this tissue and produce fluorescence very close to the surface and to the detector, thus with low attenuation. On the other

hand, as the Zn in the rectal wall is homogeneously distributed, an appropriate instrumental calibration permits correcting the detected Zn content by subtracting this offset rectal-wall contribution. Example of scattering contribution to the detection sensitivity originating from the rectal wall has been empirically estimated, using the DPH-based detection system, from the irradiation of a test bi-compartment phantom. The first compartment (3 mm thick), representing the rectal wall, contained 2000 ppm of Zn while the second one, representing the prostate compartment, included no Zn. Figure 73 shows the resulting net Zn-K_α counts profile $\Phi(z)$.

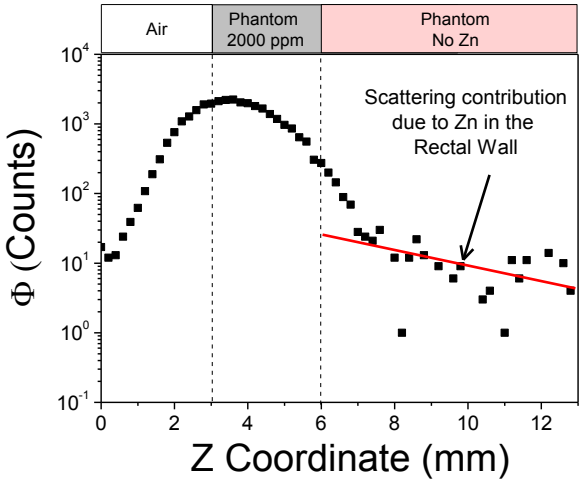

Figure 73. Net Zn-K_α counts profile, obtained by scanning a phantom made of two homogeneous compartments. The first 3 mm thick compartment contains 2000 ppm of Zn (rectal wall) while the second one do not contain any Zn (prostate). The scattering contribution to the sensitivity, originatedfrom rectal-wall Zn, is visible and is fitted by an exponential tail.

The large peak in the counts profile curve of figure 73, clearly seen in the region of the rectal wall, results from the convolution of the sensitivity profile with the uniform concentration of Zn in this compartment. For low irradiation depth, specifically when the sensitivity profile is fully contained within the prostate compartment, practically no Zn fluorescence is expected to be detected. However, as illustrated by figure 73, a small exponentially-decaying contribution is measured: these detected fluorescence photons can be originated only from Zn located in the rectal wall and by exciting radiation scattered towards the surface of the phantom.

Figure 74 shows the net Zn-K_α counts profile of figure 73, corrected by a factor which takes into account the attenuation of the exciting beam $\Theta(z)$, as the target-volume moves deeper inside the inspected phantom. At the deepest irradiation depths a constant level of recorded Zn-fluorescence counts is clearly visible, and it is proportional to the amount of Zn contained in the 3 mm rectal wall. The two described experiments were conducted with a small area detector and small detection

solid angle, such that the amount of recorded fluorescence, originating outside the target-volume by scattering effects, was negligible.

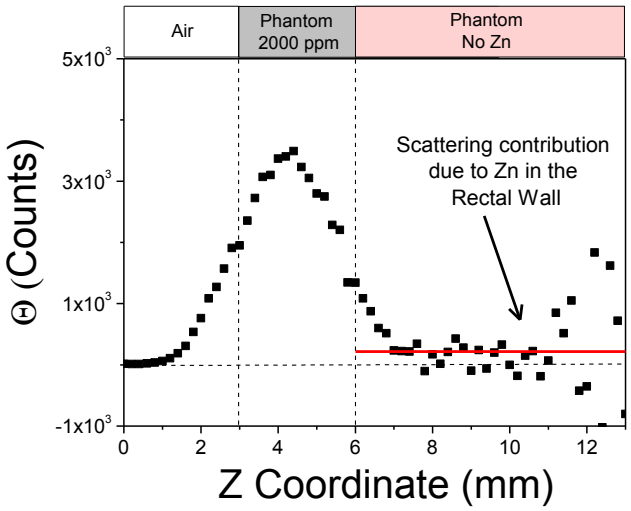

Figure 74. Net Zn-Kα counts profile corrected for the attenuation of the exciting primary beam. The constant level of fluorescence counts at the lowest irradiation depths is due to fluorescence originated in the rectal wall and proportional to the amount of Zn contained in that compartment.

With a large detector and a larger solid angle, similar to the one designed for the trans-rectal medical probe, and with a simple calculation, it turns out that, assuming a nominal amount of Zn in the rectal wall, of the order of 20 ppm, and an average amount of Zn of the order of 100 ppm in the prostatic compartment, the contribution to the detected signal due to scattering should be below 5% up to an irradiation depth of 7 mm and no more than 20% at an irradiation depth of 10 mm.

6.2.6 2D Imaging of Zn distributions in phantoms

The imaging capability of the proposed XRF-based method was investigated by recording 2D Zn-maps from multi-compartment TE phantoms with tumor-like low-Zn inclusions. The phantom was mounted on a dedicated computer-controlled X-Y stepping motor system which allowed for displacement of the target-volume within the phantom (figure 75).

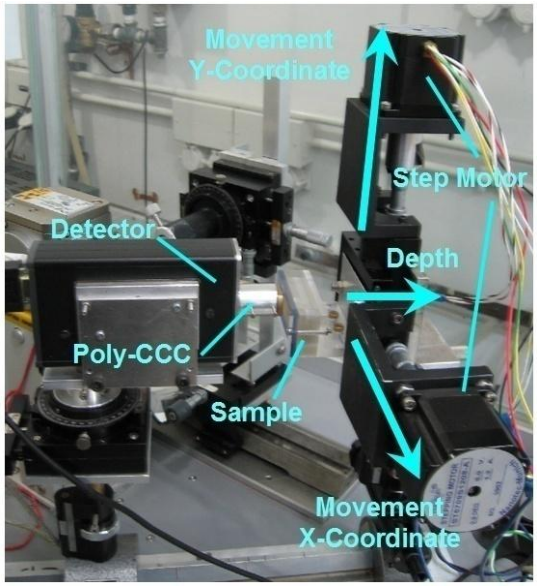

Figure 75. Experimental setup used for acquisition of 2D Zn-map images of multi-compartment phantoms.

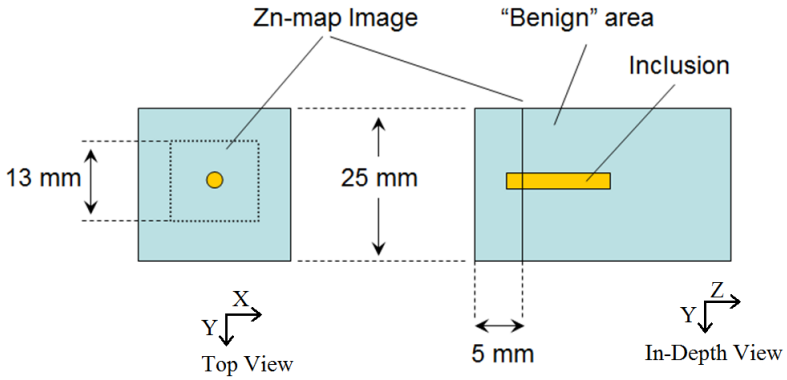

Figure 76. Typical structure of the bi-compartment SZ-50 phantom used for Zn-mapping. The spectral acquisition was taken at an irradiation depth of 5 mm. The scanned surface corresponded to a square of 13x13 mm.

The detection system comprised the 5 mm^2 SSD sensor preceded by the Poly-CCC. The Zn-map images were acquired irradiating dual-compartment phantoms (figure 76) with different benign-to-cancer contrasts and at different irradiation times, in order to study the counting-statistic effects on detection sensitivity and spectroscopic accuracy. As an example, figure 77-Figure 79 illustrate 13x13 pixels Zn-map images of a two-compartment TE phantom, comprising a homogeneous "benign compartment" with 150 ppm of Zn, containing an inclusion (around 3 mm in diameter) simulating the malignant lesion with 50 ppm of Zn. The Zn-map was measured at irradiation depths of 3 mm (figure 77a), 5 mm (figure 78a) and 7 mm (figure 79a). The irradiation times were set to 120, 400 and 1000 seconds per pixel, corresponding to an average of 3, 1.75 and 0.6 Zn-K_α net counts per ppm, respectively. The Zn-maps were digitized in 16-bit grey-scale format and successively analyzed with image processing tools developed for the computer-simulated Zn-

map images (described in paragraph 3); these tools comprised a 3x3 Median Filter for noise reduction, followed by image segmentation based on the expectation maximization (EM) algorithm. The final result (figure 77-Figure 79 part b) is a binary image showing the cluster with the lowest Zn concentration - corresponding to the cancer-like inclusion.

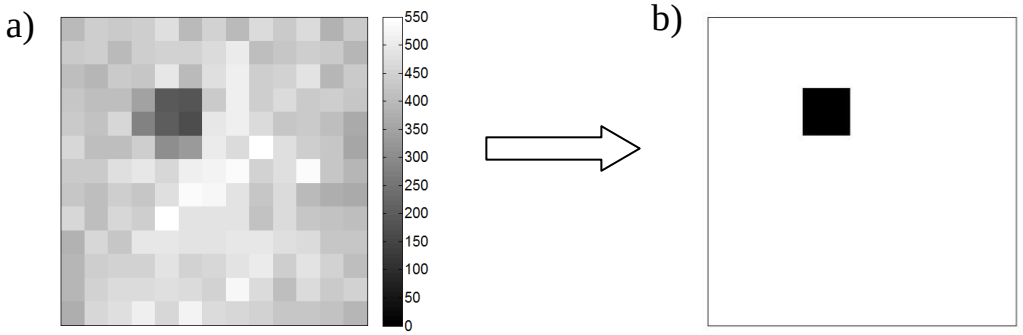

Figure 77. a) shows a 13x13 pixels raw image of Zn concentration map recorded at a depth of 3 mm in a phantom comprising a homogeneous "benign" compartment having 150 ppm of Zn and a small inclusion (~3 mm in diameter) with 50 ppm of Zn. b) shows the results after image processing with 3x3 Median filter and segmentation (only the cluster with lowest Zn is shown).

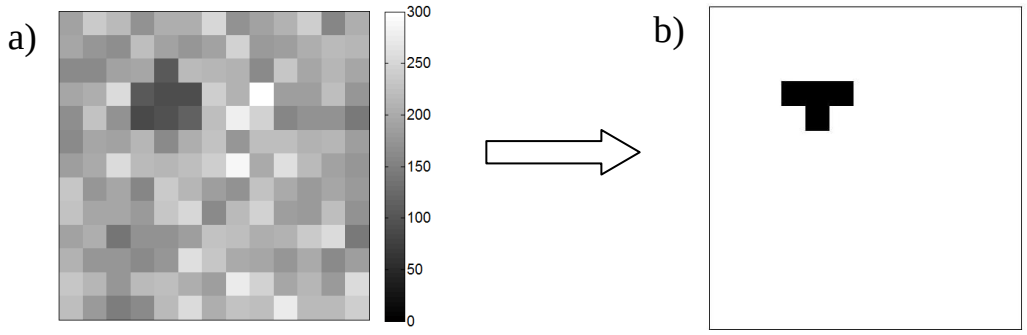

Figure 78. Same as figure 77 for irradiation depth of 5 mm.

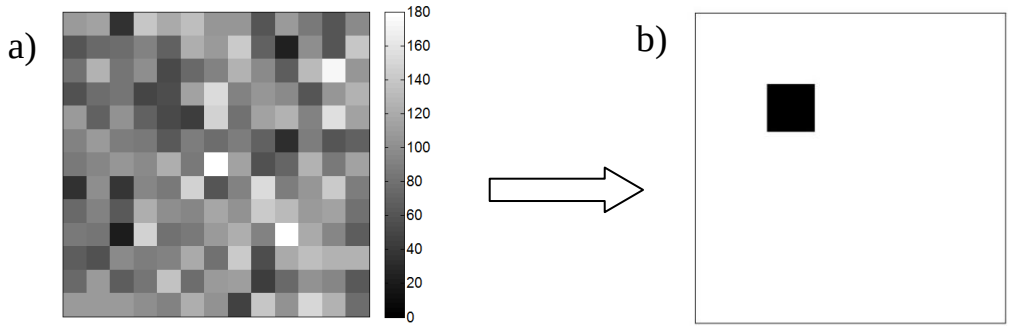

Figure 79. Same as figure 77 for irradiation depth of 7 mm.

Figure 80 illustrates detailed spectra in the energy range of the characteristic Zn-K fluorescence lines, recorded from the "inclusion" (figure 76) with ~ 50 ppm of Zn (part a - blue line) and from the "benign" area (figure 76) with ~ 150 ppm of Zn (part b - red line); their analysis allowed generating the Zn-map image depicted in figure 77a (irradiation depth at 3 mm).

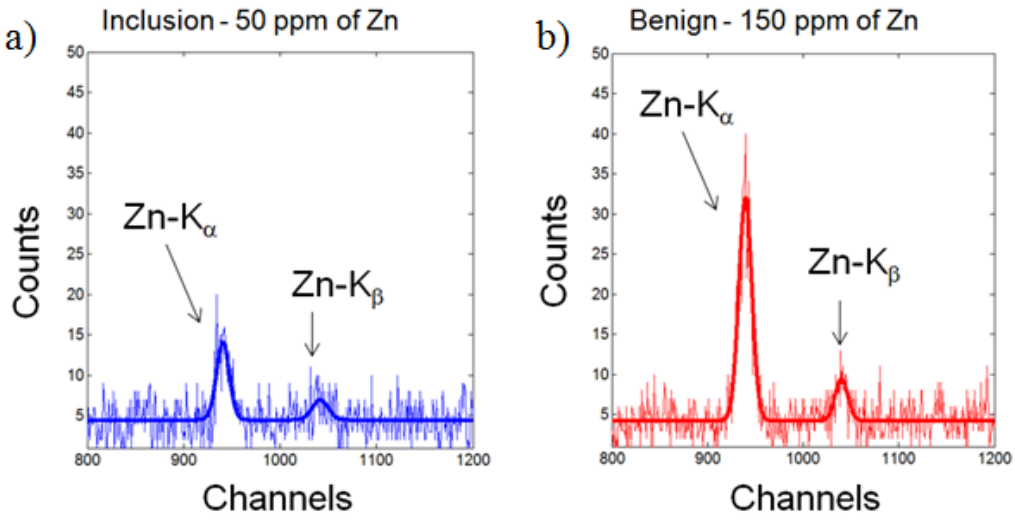

Figure 80. Details of the spectra in the energy range of the characteristic Zn-K emission lines, measured in the "inclusion" area (part a) and in the "benign" area (part b) of the Zn-map image depicted in figure 77 (irradiation depth of 3 mm). Gaussian fits of the two Zn-K lines are also shown.

Finally, figure 81 illustrates an example of a Zn-map image of a multi-compartment SZ-50 phantom comprised of a background matrix including high Zn (2000 ppm), and three cylindrical inclusions of 3 mm in diameter; two of them contain no Zn while the third one possesses a Zn concentration of 1000 ppm. Notice that, the two inclusions with no Zn are distinguishable against the high Zn background due to a significant contrast. The inclusion with 1000 ppm of Zn is also noticeable though with lower contrast, slightly masked by a markedly decrease of signal intensity in the lower right corner of image; indeed, in this particular case, the phantom was not perfectly aligned with to the X-Y motor scanning plane and the acquisition of the lower right corner of the image was performed at a slightly deeper position inside the phantom, leading to a higher signal attenuation.

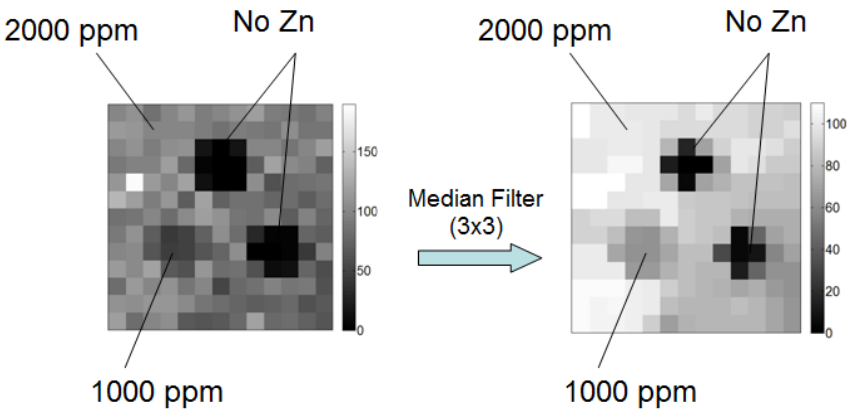

Figure 81. Part a) shows the raw Zn-map image (acquired at a depth of 5 mm) of a multi-compartment phantom (background matrix with 2000 ppm of Zn), containing three inclusions: two of them with no Zn and one with 1000 ppm of Zn. In part b) the image resulting after processing the image in part a) with a 3×3 median filter.

7. Summary and Discussion

7.1 The clinical study

We have carried out a broad systematic study on needle-biopsy samples from the prostate, encompassing several hundred patients (> 600) from two medical centers in Israel. Both the Patient-Average and the Local Zn concentration were studied for their diagnostic value by comparing their distributions with the histological information collected for the same tissue segments.

The most important result of our study is the positive correlation of the Local Zn concentration with the histological classification of the tissue, as Non-Cancer or PCa, with further correlation with the Gleason grade classification within the PCa group. This result implies that the specificity and sensitivity of Local Zn concentration improves with the grade.

It is interesting to note that the Zn depletion occurs not only in the cancerous tissue segments but also, though less pronouncedly, in the Non-Cancer components surrounding the lesion, and in correlation with the Gleason score. It is possible that although PCa has not been observed by the pathologist in these regions, the cellular precursor for its appearance is already present, and is more pronounced the more aggressive is the malignant process in the other parts of the prostate. Such behavior does point at a global aspect of the pre-malignant and malignant processes in the peripheral zone, in combination with the pronounced local quality of Zn depletion.

Since any tissue segment always contains a mixture of cells of various types, the Zn concentration in either Non-Cancer or PCa-diagnosed segments has a broad distribution, resulting in a significant overlap of the distributions for Non-Cancer and malignant tissue segments. We conjecture that the overlap between the distributions for Non-Cancer and malignant tissue segments is due to: i) the segments scan size (4 mm); and ii) the inherent spread in the Zn values associated to a group of patients. Since the measured Zn depletion is related to the lesion size and the fraction it occupies within the measured volume, it is clear that the smaller the lesion the less pronounced is the depletion in the measured Zn value. Accordingly, if the size of the lesion in any given fragment of a biopsy core is small, then the effective Zn concentration measured for that fragment will be higher and lead to a broadening of the Zn distribution curve for a particular score.

Moreover, because in our study most of the PCa patients had only a single positive (malignant) biopsy core or even a single malignant core's segment, we could not construct Zn distributions representing the situation in a single person. Instead, the distributions presented in

figure 18 or figure 21, for example, are based on local Zn data from several tens of patients and are most probably influenced by mechanisms other than the malignant process. For example, there is always patient-to-patient variation in the Zn metabolism, which influences the Zn levels and broadens the distributions based on a large ensemble of patients; we may speculate that if we could correct the data for this effect the distributions would be narrower and probably less ambiguously overlapping.

On the other hand, related to the difference in person-to-person Zn metabolism, there might be some, yet unidentified, mechanism that correlates the Zn levels in both the Non-Cancer and malignant compartments in a given person in such a way that the contrast between them is reduced. Such a mechanism might be related to the Zn transport regulation (Costello et al. 2005), affecting the concentration in the entire gland. Unfortunately, the current data do not permit to disentangle these questions or provide estimation on their importance.

To summarize, our data point at the following conclusions:

- The most important conclusion is that the Local Zn concentration, measured in 1-4 mm^3 fresh tissue segments, shows a clear correlation with the histological classification of the tissue, whether Non-Cancer or malignant, and a systematic positive correlation with the Gleason grade classification of the cancer: the higher the Gleason score the greater the Zn depletion, and the larger the contrast between the malignant and the Non-Cancer tissue components. This indicates that the amount of Zn depletion could be used as a measure of the Gleason grade of the tumor. Additionally, it means that the higher the Gleason grade, the smaller the detectable lesion.
- A new finding of this work is that there is an influence of a Zn-rich diet, tending to increase significantly the Zn levels in cancerous tissue, in opposite to the spontaneous Zn depletion preceding a malignant process. There is however no evidence that the diet is inhibiting or controlling the malignant process in any fashion.
- The current data is based on information accumulated from several tens of PCa patients in each Gleason score category. Some open questions remain, concerning the person-to-person variation and the correlation of Zn level within benign and cancerous tissue components of the same person. These could not be completely addressed within the present research: nevertheless, based on a few cases that did have sufficient statistics per person, we have a good reason to anticipate even better contrasts than the ones presented in this work.

7.2 Monte Carlo simulation of XRF imaging: PCa detection and grading

In the present section we analysed the potential diagnostic capabilities of the proposed method for the detection of prostate cancer, based on image processing of prostatic Zn-concentration images. The images were created by computer simulation, on an independent-pixel basis, using an algorithm which generated random Zn-values from empirical probability distribution functions. The algorithm further introduced random counting-statistics noise, based on Poisson distribution. The images encompassed small, randomly-distributed, cancer-lesions, of different Gleason grades, surrounded by benign tissue.

A simple mathematical procedure for the analysis of images was introduced and optimized to provide detection, grading and staging of the lesion. The images were first submitted to a noise reduction step, which preserved edge and morphological details of the Zn distribution. Then they were subject to a segmentation algorithm, which partitioned the image according to areas of similar Zn levels, defined the lowest Zn concentration cluster and provided its average Zn concentration value, LC_{Zn}. The latter was used as a binary classifier test to discriminate the cancer lesions from benign tissue. The detection quality of the classifier was evaluated with ROC analysis, which confirmed very reliable detection for high grade lesions, even if their volume is small (< 0.5 cm^3). Finally, the LC_{Zn} value was correlated with the detected area of the identified lesion, to provide the most probable grade of the lesion, and then the true area could be extracted from the detected one after some grade-dependent correction. The last step provided the grading and staging of the detected lesion.

Within the present work we have studied the quality of cancer detection and its dependence on counting statistics noise, image spatial resolution, lesion-size and cancer aggressiveness (Gleason grade). The receiver operating characteristic curve (ROC curve) analysis permitted to quantitatively evaluate the diagnostic reliability and to optimize the analysis parameters. It became clear that the detectability of cancer is primarily related to the Zn-image contrast, which in turn depends on the histological grade of the detected cancer. The approach presented in this work predicts a potential for excellent sensitivity in detecting small PCa lesions, even with rough spatial resolution. It was shown that an image of 15×15 pixels is largely sufficient for the detection of clinically relevant lesions of medium and high grades: 0.5 cm^3 for Gleason grade 4+3 and above and 1 cm^3 for cancer lesion having primary Gleason grade equal to 3. This predicted detection quality is not only significantly superior to that of PSA, but it improves with the cancer aggressiveness, promoting high-risk cancer detection. Finer spatial resolution increases detectability

and permits detecting smaller tumors, but, due to dose considerations this will, in practice, involve lower statistics and higher noise level. Furthermore, the analysis of Zn maps may also provide information about the site, size and grade of the detected lesion, the latter being a unique feature of the Zn-based approach. Low-grade cancers, with primary pattern of grade 3, have Zn frequency distributions similar to that of benign tissue. Consequently, their Zn-map analysis did not provide valuable results at present. As pointed out in the introduction, the present analysis is based on Zn-concentration frequency distributions collected from several patients per category (figure 23); these might be broader than the distributions from a single patient, due to patient-to-patient variation effects. Consequently, the images under analysis are probably of poorer contrast than could be expected for a single patient case, and the conclusions on the detection, grading and staging quality are a worst-case estimate. In particular, it is possible that the Zn distributions in single patients with low Gleason grades (3+3 and 3+4) are narrower than the ones shown in figure 23 and thus the lesion could be better differentiated from the benign-tissue. In the present work we have only considered the noise effect of counting statistics, assuming a simple model of Poisson distribution. We have studied the effect of counting statistics on cancer-lesion area detectability in relation to the image spatial resolution, the intrinsic instrumental sensitivity and the total irradiation time (dose) per pixel. We have shown that at a sensitivity of about 0.05 counts/ppm/pixel, the optimum detectability is achieved, with no further benefit from increase of dose. Other sources of noise such as scattering and detector/experimental system noise are not treated here – they are related to the specific instrumentation and geometry used for recording the Zn map, and will be the subject of a study presented in section 6.

7.3 Conceptual Design of the XRF probe

The evaluation of the most efficient exciting-beam energy and the optimization of the collimator system, aiming at reaching the highest sensitivity of detecting Zn at well-defined gland's sensitive target volume, have been established.

The calculations show that up to the deepest relevant depth of around 10 mm in tissue (namely 3 mm of rectal wall and 7 mm of prostate), the optimal energies in terms of fluorescent yield converge to a value of around 13-20 keV (figure 38) while the optimal energies in term of absorbed dose is shifted towards the range of 20-30 keV (figure 40). However, while the fluorescent yield strongly decays as the exciting beam energy deviates from the optimal value, the radiation dose per absorbed exciting photon shows a roughly smooth plateau for a wide energy range (from

20 to 30 keV). Moreover, the calibration of the exciting beam spectrum would eventually be dictated by overall performances of the employed X-ray source at the deepest irradiated tissue layer, where the sensitivity of the detection system is critically small. In these terms, a quasi mono-energetic X-ray beam, centred at an energy around 20 keV will provide the highest fluorescence yield, reducing at minimum the exposure time and with minimal absorbed dose deliver to the patients. Optimal collimator aperture: ~ 46^{O}.

A probe design-concept was sketched and some design parameters have been studied by physical simulations of the full path of interactions of the X-ray radiation with the prostate tissue and the probe components. It has been established that a critical probe component is the con-focal collimator placed between the organ and the detector, of which the role is to define the voxel from which the recorded radiation originates, with minimum contribution from scattering.

The fluorescence radiation from the inspected target volume reaching the detector is subject to self-absorption in the gland tissue, which is significant for the low characteristic zinc-fluorescence energy; this determines the radiation dose necessary for a reliable zinc-content evaluation. The calculations assumed scanning the prostate with mono-energetic incident beams and a detection system comprised of an ideal spectroscopic detector proceeded by a poly-capillary collimator system. It was shown that the information form the target-volume depends on the energy and the flux of the exciting radiation, the energy of the fluorescent radiation, the incidence angle and the angle of detection. It followed that the the detection sensitivity decays exponentially with the irradiation depth. The spatial resolution of a 3D XRF scanning system would depend on the values of the overlapping focal profiles. In addition, it was understood that the focal spot (millimeter size) seen by the conical collimator capillaries needs to be calibrated according the exciting beam diameter, in order to achieve maximal efficiency in detecting fluorescence radiation originating from the target-volume.

In addition, the accuracy of the XRF analysis may be considerably affected by scattering processes that take place in the irradiated sample: indeed the scattering of both exciting and characteristic radiations may affect the detected XRF intensity. It was shown that, up to the irradiation depths relevant for prostate diagnosis (1 cm in tissue including rectal wall), the contribution to the sensitivity due to scattering is less than 20%.

The quantitative evaluation of Zn content is projected to be achieved using the following approach (figure 82): a collimated parallel beam will be directed into the gland; the resulting characteristic Zn radiation, from a target-volume within the gland, will be recorded by a planar detector preceded by a dedicated poly-conical capillary collimator; the latter is essential for

reducing the scattered radiation reaching the detector and for precisely defining the inspected target-volume. A Zn-content map will be obtained by scanning the gland, with either probe displacement or that of its elements.

7.4 Conclusion on Medical-Probe Design

Finally, the Zn mapping method in clinic has been designed, and predictions were made for radiation-induced secondary-cancer risks. Design details, properties and expected performances are given below.

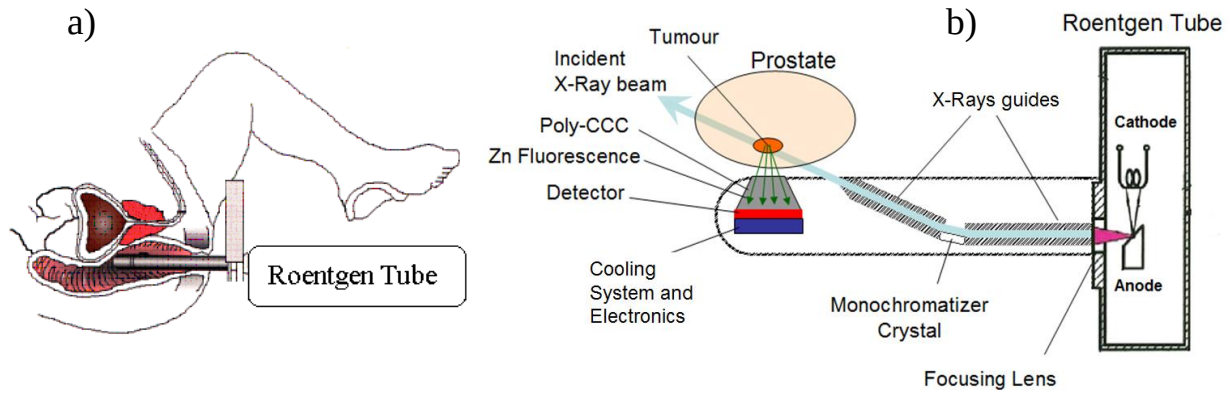

Figure 82. a) The Zn-imaging method. b) schematic view of the conceptual probe-system assembly

7.5 Exciting channel (X-rays generator, optics and monochromator)

The localization and quantification of Zn in the peripheral zone of the prostate, requires the excitation of Zn atoms by a photon beam directed to the gland. The exciting beam should have the following properties:

-) small diameter (in order to guarantee small target volume and therefore good spatial resolution);

-) good parallelism;

-) high intensity (in order to reduce exposure time);

-) good mono-chromaticity (in order to limit absorbed dose delivered during exposure);

The design of the exciting-channel and the choice of elements, including the selection of the x-ray spectrum, are dictated by the overall system performances at the deepest irradiated tissue, where the detection sensitivity is critically small (due to self absorption of the characteristic Zn

line). As already mentioned in chapter 3, the deepest irradiation depth, relevant for a clinically effective examination, is of the order of 10 mm in tissue – namely 3 mm of (not examined) rectal wall plus 7 mm of prostatic tissue. We calculated that the optimal beam, in terms of irradiation time and dose, should have a narrow energy spectrum center at 18-20 keV (see chapter 5). The monochromatization will also eliminate the undesirable part of the continuum spectrum, reducing background, and considerably enhancing sensitivity and detection limits (LOD).

The best proposed design for the exciting channel includes a low-power (50-100 W) micro-focus Mo-target x-ray tube, combined with the effective collecting and focusing properties of polycapillary half-lens. The poly-capillary half-lens focus has to be adjusted to be compatible with the distance to tube anode, in order to collect most of the photons emitted within a large solid angle (figure 83).

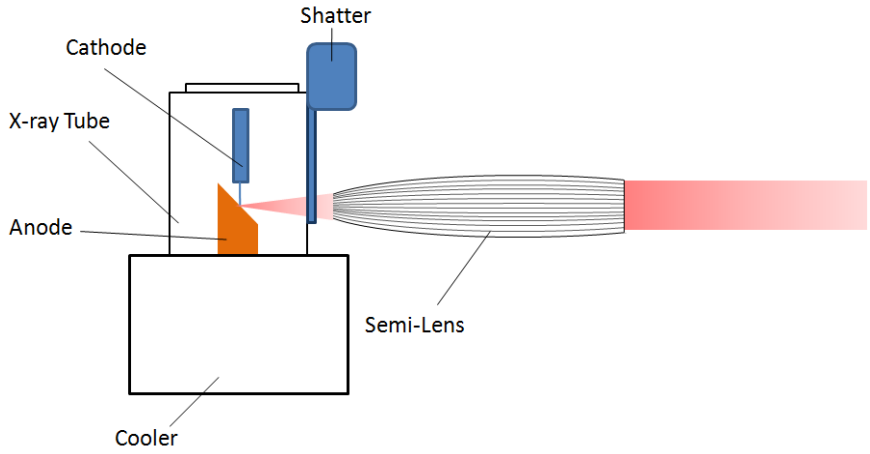

Figure 83. The X-ray source, comprising a high-intensity tube and focusing semi-lens.

The emerging radiation is transmitted in the form of a polychromatic quasi-parallel beam and directed onto a small-angle beam bending element, e.g. a highly oriented pyrolytic graphite mosaic crystal (HOPG). The HOPG monochromatizes the beam energy via Bragg diffraction, resulting in a narrow-energy (~18-20 keV) and high-intensity X-ray beam. Finally, a beam-focusing optics (e.g. a second multi-fiber polycapillary lens paired with a suitable diaphragm) is needed to irradiate the organ at well-defined geometry and to reduced beam divergence (beam divergence less than 20 mrad can be easily achieved with suitable capillary guide). For reaching maximal radiation intensity, the most important feature in this configuration is the matching between the critical angle of total reflection and the half width of the rocking curve of the crystal. This minimizes intensity losses when X-rays are reflected by the crystal and then captured again by the second capillary (Gao et al. 1997). The market offers various technological solutions and small size X-ray sources,

generating high flux quasi-monochromatic photon beams. As an example, the Institute for Roentgen Optics (IRO) has created a pioneering X-rays generator (named "Laboratory Synchrotron"), based on a 10 W x-ray tube developed in-house, combined with a new generation of polycapillary lenses - named Kumakhov Integral Lenses (KIL). This device can produce a quasi-parallel monochromatic millimetre-scale beam of fluxes reaching 10^{10} photons/sec/mm^2 (Institute for Roentgen Optics IRO – Russia) with divergence of less than 10 mrad.

The implementation of such a source and similar ones by other producers (Bjeoumikhov et al. 2005) described above, represents a suitable and feasible solution for the design of the exciting channel of the proposed probe.

An alternative solution for achieving high photon flux rate (~10^{10} photons/mm/sec) with 2 mm beam diameter may be a microfocus Roentgen tube followed by a paraboloidal mirror optics (figure 84). In this case, the mirror defocuses the x-rays into a parallel beam and removes the high-energy x-rays by absorption - the beam is reflected by the mirror surface that preferentially reflects the Mo-K energy range and absorbs higher energies - "band pass" monochromatization (Australian X-ray Capillary Optics – Australia). The optics consists of a cylinder ~300 mm long and 5 mm in outer diameter, suitable for inclusion inside the trans-rectal probe assembly. This solution could have some advantages: it provides a parallel output beam, containing solely a small fraction of high-energy photons; it does not require any other optics and the optic itself would provide sufficient shielding against scattering, to the patient and to the detector. In addition the μ-focus X-rays source is small in size, it requires no cooling and it can be easily handled. However, this system has the disadvantage that does not remove totally the low energy range of the Bremsstrahlung spectrum (not contributing to fluorescence adding to the absorbed dose).

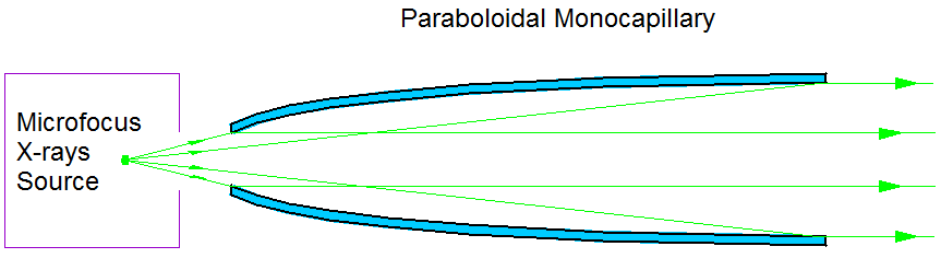

Figure 84. μ-focus Roentgen tube fitted with a paraboloidal mirror optic.

7.6 Detection channel (spectroscopic detector and collimator)

The Silicon Drift Detector is an ideal technology for applications requiring high-resolution energy-dispersive X-ray spectroscopy. The main advantage of the SDD compared to a conventional

solid-state detector of equal active area and thickness, like the ordinary p-n diode, resides in a very low electronics noise achieved thanks to the low value of output capacitance, fully exploited by the integration of the front-end transistor (JFET) on the detector. High-performance single SDD of large area (few cm^2) may be produced: excellent energy resolution (< 200 eV) may be accomplished due to the independence of the detector capacitance with respect to the active area and with leakage current reduction by a suitable cooling system (one or more on-chip Peltier cooling devices). At the moment, the size of commercially-available large-area SDD sensor is limited to 100 mm^2, though there are no technological barriers foreseen in the production of larger SSD sensors (optimal size for the prostatic trans-rectal probe is ~150 mm^2).

Another feasible solution for assembling a large-area spectroscopic detector is by tiling several independent small-area SDD elements. Figure 85 shows an example of multi-cell SDDs configuration, similar to the elements produced by PNsensor (Lechner et al. 1996); it consists of 19 hexagonal SDDs, each with an effective area of 10 mm^2 and individual on-chip JFET, arranged in a single chip with active area of 190 mm^2.

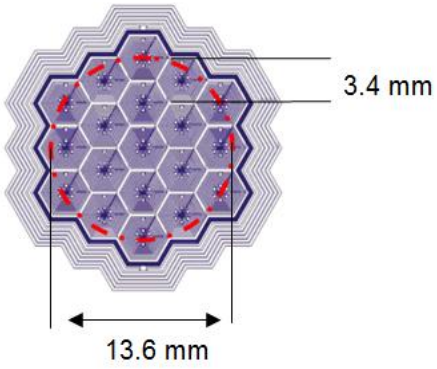

Figure 85. Monolithic array of 19x10 mm^2 hexagonal SDDs, arranged to cover an active area of 190 mm^2. The dashed-red line schematically represents the border of the present internal collimator (Poly-CCC combined with the Zr collimator) resulting in a total detection area of around 145 mm^2 (Beckhoff et al. 2006).

A miniaturized single-stage Peltier cooler mounted in a compact module may allow controlling the temperature of the detector chip. At normal working conditions the chip is cooled by ΔT ~40 °C relative to the hot side of the Peltier elements. Assuming that the temperature of probe housing, placed directly into the rectum, may reach ~37 °C, it follows that the final temperature of the chip may be of the order of 0 to few °C.

Excellent energy resolution and peak-to-background P/B ratios were recently obtained at 0 °C, respectively of 136 eV and 11,000 for a counting rate of 1 Kcps, and 145 eV and 10,000 for counting rates around 10 Kcps (figure 86). Similar performances are expected from a 150 mm^2

SDD sensor, which, according to calculation discussed in chapter 6, allows to reach a comfortable LOD of 50 ppm for the irradiation depth up to 8 mm (3 mm rectal wall plus 5 mm of prostate), assuming to assure 1 count/ppm.

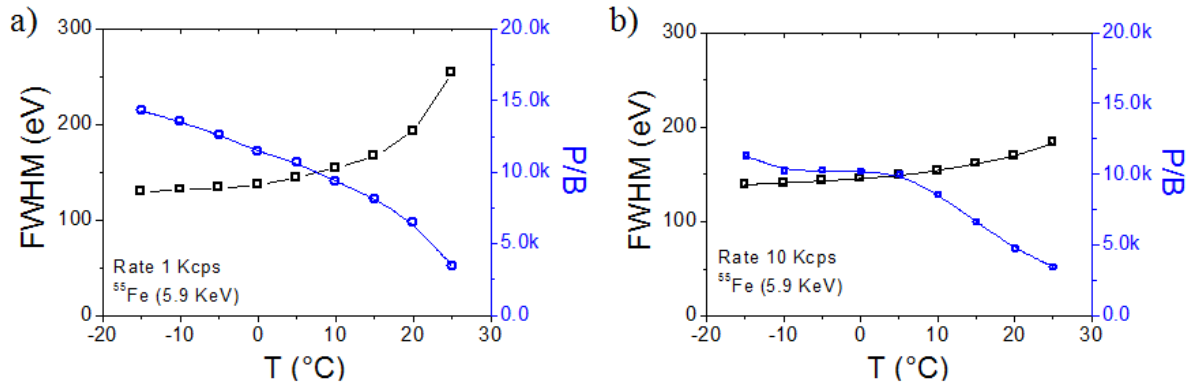

Figure 86. Energy resolution (FWHM) and peak-to-background ratio as function of the working temperature, obtained by irradiating a 5 mm^2 SDD sensor with 5.9 keV X-rays at two different counting rates, 1 Kcps (a) and 10 Kcps (b).

The structure of a feasible detection system assembly may comprise a detector enclosed in a compact package and paired with a poly-CCC, as depicted in figure 87. The net detection area of the sensor is about 150 mm^2.

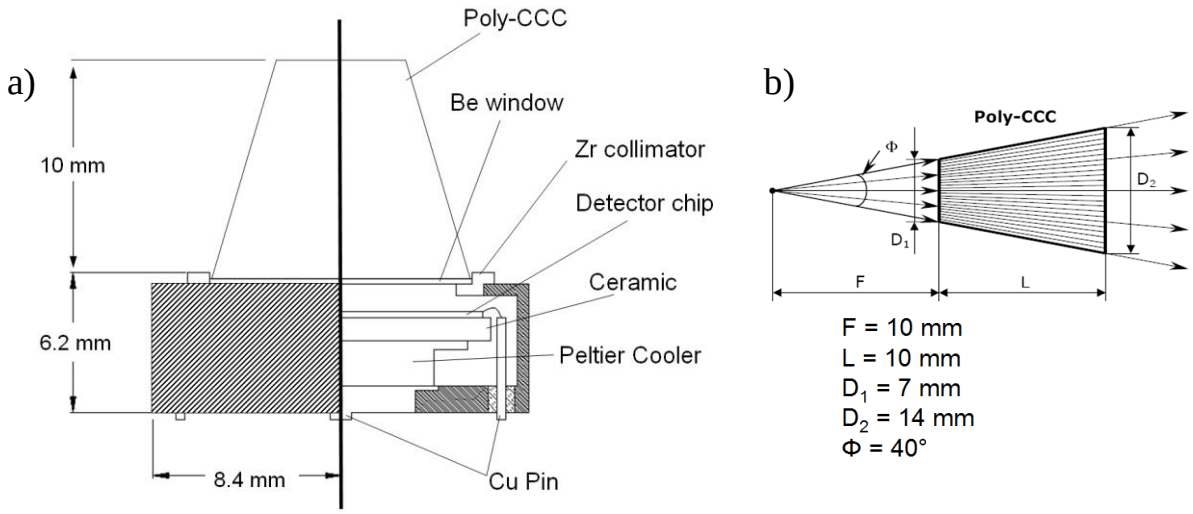

Figure 87. a): schematic drawing and dimensions of the proposed large-SDD detector package. b): geometry and dimensions of the Poly-CCC mounted on the package shown in a).

Monte Carlo simulations and table-top XRF experiments allowed us to specify geometry, dimensions, channel-diameter and material of the collimator. A pilot investigation was carried out with a commercially-available element, a Poly-CCC from IFG (Nanotec Electronic GmbH & Co.

KG, Germany), made of AR-glass; this device was coupled in our experiments to two different spectroscopic detectors (SDD and Si-PIN diode). The final version of the Poly-CCC, with precise geometry and dimensions, was designed (Figure 87b) and the expected overall performances have been computed (see next paragraph for details).

7.7 Expected performance

Further, under the following assumptions:

-) The XRF probe provides 2D scans in the peripheral zone of the prostate (depths up to 8 mm, i.e. 3 mm rectal wall plus 5 mm prostate), digitizing the measured Zn distribution of the prostate's peripheral zone in **images of 15x15 pixels**.

-) The method makes use of an optimized X-ray source system (as specified in the previous section: tube + optics + monochromatizer) providing a Narrow-spectrum (**18±0.2 keV**) exciting beam with diameter of **2 mm** and flux of **10^{10} photons/seconds/mm^2**.

-) The detection system is composed of either a single large-area or a tiled SDD sensor, with effective area of around 150 mm^2, energy resolution < 200 eV and peak-to-background ratio > 10,000, paired with a suitable Poly-CCC. The size of the target-volume would be of the order of 1.5 mm^3.

-) A total of 1 counts/ppm/pixel is considered to be adequate for obtaining the required Zn-map accuracy, overcoming counting statistics fluctuations. This, combined with the sensitivity provided by the detection system specified above, dictates the total number of photons/pixel needed in order to produce the Zn-maps at different depths.

It follows that the risk of radiation-induced cancer mortality due to a complete 2D scan of the prostate as function of the scan depth may be consequently computed; risk of induced-cancer mortality vs. scan depth is shown in figure 88, together with the total irradiation time (for details on risk of radiation-induced cancer mortality).

As an example, with the specification given above, a 2D Zn-map image with 15x15 pixels, acquired at depth of 5 mm, will take less than 5 minutes and it would lead to an induced cancer risk of around $6 \cdot 10^{-4}$; for comparison, cancer risk in mammography and in whole-body CT are 10^{-5} (Faulkner & Law 2005) and $5 \cdot 10^{-4}$ (Food and Drug Administration 2010), respectively. In addition, in the case malignant lesions are detected and efficiently graded at small depths in the

prostate, an ordinary XRF scan procedure can be interrupted with no additional dose delivered to the patient.

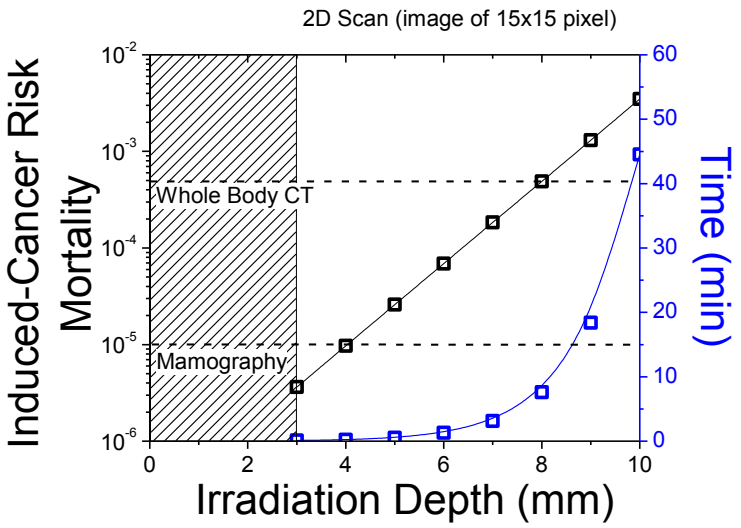

Figure 88. Induced-cancer risk mortality and total irradiation time, following a 2D XRF scan of the prostate with the specifications described above.

7.8 Potential Impact on PCa screening

The proposed Zn-imaging probe is expected to provide location, extension and grade of the suspicious lesions detected in the gland's posterior peripheral zone, where the majority of tumors are located. It has the potential to have an important impact on prostate-cancer management at various critical stages of the disease:

-) At the detection and diagnosis stage, the probe might improve patient's selection for biopsy, as a result of the expected superior specificity, sensitivity, grading capability and location information compared to present screening methods. This would increase the rate of positive biopsies above today's ~25% level, and will reduce the false-positive rate. Unlike other screening methods, the Zn-probe has the unique potential of grading the disease and staging the tumor. In view of the fact that the majority of lesions are low-grade, dormant lesions, these features are of prime importance for decision making on the disease handling, namely the strategy regarding further examinations and treatments. Besides its important role of patients' selection for biopsy, the new probe could play an important role in guiding needle-biopsy, with a potential impact of reducing the false-negative rates. Last but not least, Zn-depletion reflects chemical changes in the gland, preceding morphological ones. As such, the proposed probe may possibly localize pre-malignant stages, yet invisible in histological analysis.

-) At the pre-operative or pre-treatment stage, the probe might provide a precise tumor location and malignancy grading. It has the potential of guiding treatment tools, thus improving the efficacy of radiation therapy, brachytherapy, cryotherapy, high-intensity focused ultrasound (HIFU) etc. It is expected to provide valuable information for better decision making regarding surgery, particularly regarding tumor proximity to neuro-vascular bundles in the posterolateral aspect. Here it would have considerable impact on operative decisions regarding nerve-sparing operation vs. radical surgery.

-) At the post-treatment stage, the Zn-imaging probe could be applied as an effective, non-invasive follow-up tool and modality.

Appendix A: Image Processing

Chapter 4 was devoted to the analysis of prostatic-Zn-concentration images, aiming to evaluate clinically-relevant information that can be extracted from such images. In the absence of experimental images, synthetic ones were produced from clinically-measured Zn-concentration distributions, by means of a dedicated algorithm. Then, image analysis based on a combination of standard image processing, segmentation and classification was conceived, and used to extract the relevant information. The image processing was optimized on computer-simulated maps and was further tested on experimental ones, obtained from prostate-like phantoms with a dedicated XRF table-top system (see chapter 6). The image processing consists of:

• Denoising (Median filter)

• Detection, Localization and Staging (Image segmentation)

• Classification and Grading (Threshold selection)

The entire algorithm, comprising also a code for computer-generation of the Zn-map images, image processing and data mining was written using MATLAB 7.6 (R2008a).

A.1 Generation of computer-simulated Zn-amp image

Zn-maps representing 3x3 cm^2 prostate images were computer-generated with spatial resolution of 10×10, 15×15, 20×20, and 30×30. The zinc value in each pixel of the map was randomly selected from the experimental data (fitted with a lognormal function model) depicted in figure 23, for the benign and the malignant components. Counting statistics was also included (the value was remodeled using Poisson statistics) in order to represent a more realistic map.

The random number generator algorithm uses the matlab function:

$$Zn_{PIXEL}(x,y) = \text{lognrnd}(\mu,\sigma) \qquad \text{(A.1)}$$

which returns a random number for the pixel in position (x,y), generated from the lognormal distribution with parameters μ and σ, representing the mean and standard deviation, respectively, of the associated lognormal distribution (see footnote at pag. 31).

Counting statistics could be introduced by redefining the pixel value using the Poisson random generator function:

$$Zn_{PIXEL}(x,y) = \text{poissrnd}(\text{lambda}) \qquad \text{(A.2)}$$

which generates random numbers from the Poisson distribution with mean parameter lambda (defined by equation A.1).

A.2 Median filter

Median filtering is a nonlinear operation used in image processing to simultaneously reduce "salt and pepper" (Chan et al. 2005) noise and preserve edges. It consists of a sliding-window kernel, usually square but circular kernels and two-way hybrid kernels are also available, which replaces the center value in the window with the median of all the pixel values in the window. Various example of 5×5 Median filter kernels are explained in figure 89, including typical hybrid filter kernel: shaded squares correspond to pixels used to calculate median values, and white squares correspond to pixels that are ignored in the filtering process. The median value of the hybrid filter in figure 89 is calculated according to this methodology: M_R is the median of horizontal and vertical "R" pixels, and M_D is the median of diagonal "D" pixels. The filter value is the arithmetic mean of the two median values and the central pixel C, that is

$$\text{Median} = \frac{M_R + M_D + C}{3} \tag{A.3}$$

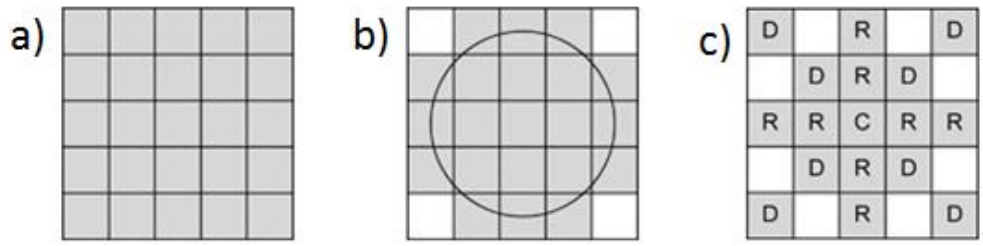

Figure 89. Examples of Median filter: a) Square kernel, box size = 5; b) Circular kernel, box size = 5; c) Example of two-way hybrid median kernel, box size = 5.

For our application, due to the limited size of the input Zn-map image to be processed, the square kernel turns out the more reliable and convenient solution: large (30×30 pixel) maps were processed with a 5×5 median filter, while smaller Zn-map images was processed with 3×3 median filter. The image processing algorithm used a standard Matlab function “medfilt2”, with the following syntax:

```
B = medfilt2(A, [n n], 'symmetric')
```
(A.4)

Where A and B are respectively the input and output Zn-map images, n is the dimension of the kernel, while the option “symmetric” extends the input matrix A at the boundaries (corresponds to mirror reflection of the input matrix A) - this allows to avoid border effects.

A.3 Image Segmentation – K-means clustering

Image segmentation refers to the process of partitioning a digital image into multiple segments (or sets of pixels). The goal of segmentation is to simplify and/or change the representation of an image into something that is more meaningful and easier to analyze. Image segmentation is typically used to locate objects and boundaries (lines, curves, etc.) in images. The result of image segmentation is a set of segments that collectively cover the entire image, or a set of contours extracted from the image (see figure 90). Each of the pixels in a region is similar with respect to some characteristic or computed property, such as color, intensity, or texture (in our case, same average Zn value). Adjacent regions are significantly different with respect to the same characteristic(s).

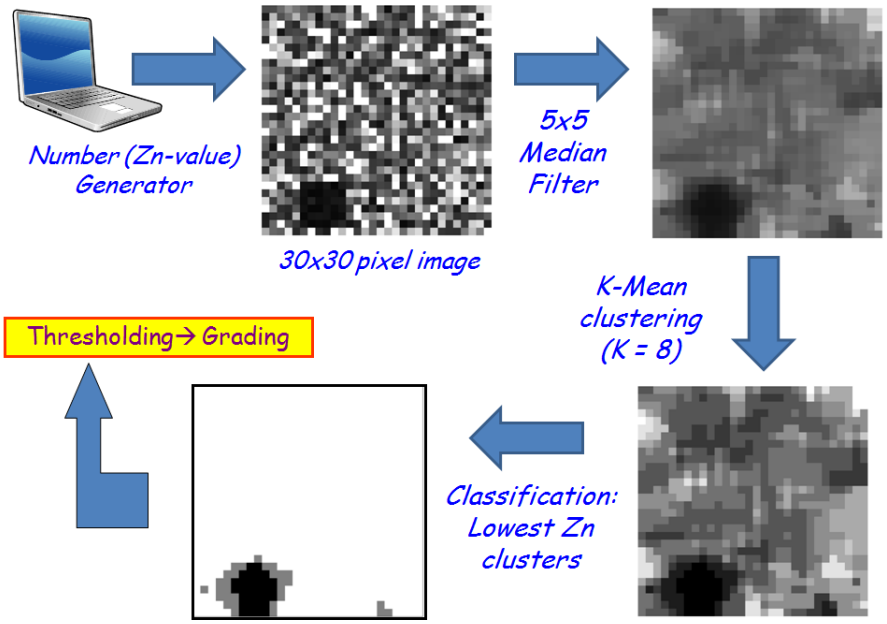

Figure 90. Image processing: Computer-generation, followed by denoising filter, image segmentation (k-means clustering) and classification (thresholding).

The k-means clustering is one of the algorithms for image segmentation; it is an iterative technique that partitions the analyzed image into k clusters (where k < n), based on the

minimization of intra-cluster variance methodology (Macqueen 1967). The most common form of the algorithm uses an iterative refinement heuristic known as Lloyd's algorithm (Lloyd 1982).

The algorithm proceeds by the following computational steps:

1. Pick k cluster centers, either randomly or based on some heuristic data
2. Assign each pixel in the image to the cluster that minimizes the distance between the pixel and the cluster center
3. Re-compute the cluster centers by averaging all of the pixels in the cluster
4. Repeat steps 2 and 3 until convergence is attained (e.g. no pixels change clusters)

Distance is defined as the squared or absolute difference between a pixel value and a cluster center: the difference is typically based on pixel color, intensity, texture, and location, or a weighted combination of these factors - in our application we consider the pixel color intensity (expressed as 8-bit gray-level), correlated to the Zn concentration value measured in that pixel. Eventually, the output of the segmentation algorithm is an image decomposed into k clusters, each cluster is characterized by the set of pixels (cluster location), average Zn value and variance.

A.4 Classification and Grading (Threshold selection)

The image segmentation process produces an image whose gray-level histogram is grouped into k modes. In order to extract Zn-depleted regions from the background (i.e. regions that are suspicious of the cancerous malignancy from benign tissue), the lowest Zn-value cluster is selected. figure 32 depicts the correlation between these two parameters, based on all lesion size/grade combinations studied (500 maps for each combination). The data segregate in clear loci, each corresponds to a single Gleason grade combination. The loci are unambiguously separated from each other in the region below the dashed line. In the region above the dashed line, data of different grades are partially overlapping, including the benign cases. Within this region, though, limited discrimination can still be done, between high and low-grade cancers, as indicated in the figure. figure 32 is the basis for the grading capability of the zinc-mapping method: when an unknown lesion is ‘‘detected’’ by the image processing of a zinc concentration map, it is assigned with zinc value and area. By plotting these coordinates on the scheme of figure 32 the lesion classification, for example, as benign or as a malignant of a certain Gleason grade, emerges. Following the grade assignment the ‘‘detected’’ area could be further corrected. The grading capability improves systematically with the aggressiveness of the disease.

Appendix B: Calculation of the radiation induced-cancer risk

This section illustrates the details of the calculation for absorbed dose, and radiation induced-cancer risk, presented and discussed in the paragraph 7.3. The calculation is based on dosimetric methodology commonly used in diagnostic medical X-ray imaging.

According to the quality assurance (QA) practice formulated by the International Commission on Radiological Protection (ICRP), an accurate determination of relevant dosimetric quantity is important for any application in diagnostic radiology. Specifically, in medical X-ray imaging there are two fundamental motivations for measuring or estimating the patient absorbed dose:

-) Dose measurements provides means from setting and checking standards of good practice, as an aid of optimization of the radiation protection of the patient and of the image quality. The most essential goal is the optimization of the image quality with respect to absorbed dose, avoiding unnecessary doses that induce significant carcinogenic risk
-) Estimates of absorbed dose to tissue and organs are needed to assess radiation detriment, so that radiological techniques can be justified and cases of accidental overexposure investigated.

As is well known, several parameters that commonly characterize the image quality (e.g. signal-to-noise ratio SNR) correlate well with absorbed dose; consequently, there may be a tendency for increasing the patient doses to levels higher than actually necessary, aiming at improving the image quality. However, not all medical imaging tasks require the same level of image quality- the latter should be judged by the relevant diagnostic information extracted from the image. For that reason, specific criteria need to be established for different imaging tasks to avoid excessive doses where there is no net benefit in the diagnosis. Nevertheless, the image quality should be understood as the relevant information appropriate to the clinical situation. As a consequence, it is important to ensure that efforts to reduce patient doses do not degrade the image quality to an unacceptable level.

The quantities used for deriving the absorbed dose and relevant coefficient for computation of the induced radiation-cancer risk, are the following:

-) The energy fluence (Ψ) is the radiative energy flux integrated over time, namely:

$$\Psi = \frac{dR}{da} = \left[\frac{Joule}{m^2}\right] \tag{B.1}$$

where dR is the radiant energy incident on a sphere of cross-sectional area da (ICRU, 1998c). For a well collimated mono-energetic photon beam, the energy fluence at depth z in a sample may be expressed as:

$$\Psi(z) = \frac{N(x)}{A}\varepsilon = \frac{N_0}{A}\ \varepsilon\ e^{\left[-\left(\frac{\mu}{\rho}\right)\rho\frac{z}{\cos(\varphi)}\right]}e^{\left[-\left(\frac{\mu_{li}}{\rho}\right)\rho z\right]} \tag{B.2}$$

where A is the cross sectional area of the beam, N(z) is the total number of photons that intersect the beam area A at depth z, N_0 is the number of photon at the surface and (μ_{li}/ρ) is the photon mass attenuation coefficient at energy ε.

-) The absorbed dose (D) is used to quantify the deposition of energy by ionizing radiation. It is defined in ICRU Report 60 (1998c) by the following equation:

$$D = \frac{d\varepsilon}{dm} = \left[\frac{Joule}{Kg}\right] = [Gy] \tag{B.3}$$

where dε is the mean energy imparted to matter of mass dm. Under conditions of charged particle equilibrium, the absorbed dose to material t is related to the energy fluence by the mass energy absorption coefficient in that material $(\mu_{en}/\rho)_t$. Charged particle equilibrium at a point P is said to exist if, in a small volume V around P, each charged particle carrying out a certain energy is replaced by another identical particle which carries the same energy into the volume. For mono-energetic photon beam, the absorbed dose at depth z is defined as

$$D_t(z) = \Psi(z)\left(\frac{\mu_{en}}{\rho}\right)_t = \frac{N_0}{A}\ \varepsilon\ e^{\left[-\left(\frac{\mu}{\rho}\right)\rho\frac{z}{\cos(\varphi)}\right]}e^{\left[-\left(\frac{\mu}{\rho}\right)\rho\frac{z}{\cos(\varphi)}\right]}\ \left(\frac{\mu_{en}}{\rho}\right) \tag{B.4}$$

where N_0 and ε are respectively the number and energy of the primary photon beam impinging on the specimen surface, (μ/ρ) is the mass attenuation coefficient of the material from which the irradiated sample is made of and φ is the incident angle of the primary photon beam.

In the case of polychromatic photons beam, an effective mass energy absorption coefficient should be used, the value of which is weighted according to the energy spectrum. It is important to specify the point where the absorbed dose is measured and the irradiation conditions should also be defined. Figure 87 shows a dose profile (absorbed dose as function of depth) normalized per impinging primary photon $D_t(z)/N_0$, calculate assuming the irradiation of a tissue-equivalent specimen (0.3 cm of rectal wall + 3 cm of prostate) by a photon beam of energy ε = 18 keV and with incident angle $\varphi = 45^o$.

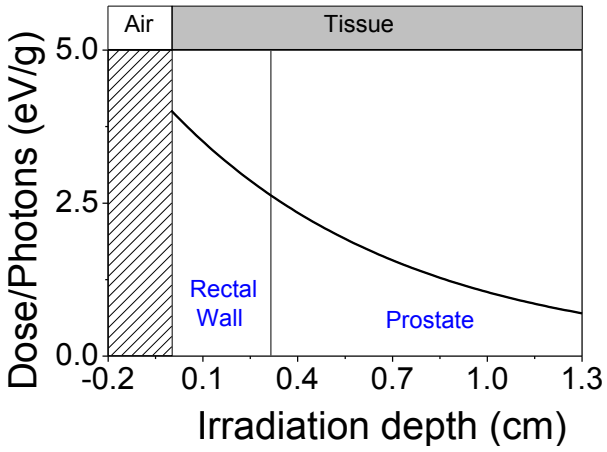

Figure 91. Dose profile delivered during irradiation of a rectal wall & prostate-like specimen (0.3 cm of rectal wall and 3 cm of prostate) by a photon beam of energy ε = 18 keV and with incident angle φ = 45°.

Several practical quantities have been introduced for dosimetric measurements in medical X-ray imaging, including for example the incident surface dose (D_{IS}), entrance surface dose (D_{ES}), dose area product (D_{AP}) (used mainly for fluoroscopy examination), CT Dose index (used for CT examination). Nevertheless, the ICRP has recommended that the appropriate dosimetric indicator for the probability of stochastic radiation effects is the average absorbed dose in a tissue or organ (ICRP, 1991b). Indeed, at low irradiation levels, the mean absorbed dose in organs or tissues in the human body are indicators of the probability for stochastic effects onset; at high irradiation levels, absorbed doses to the more heavily irradiated sites within the body are indicators of the severity of deterministic effects. In ICRU Report 51 (1993b) the mean absorbed dose in a specified organ or tissue T has been given the symbol D_T and is defined as the integral of the absorbed dose D_t over the mass of the tissue normalized by its mass m_T, namely

$$D_T = \frac{1}{m_T}\left(\int_{m_T} D_t \, dm \right) \tag{B.5}$$

where D_t is the absorbed dose at a point in tissue material t, or as the energy imparted (ICRU, 1998c) to the tissue, ε_T, divided by its mass.

$$D_T = \frac{\varepsilon_T}{m_T} \tag{B.6}$$

For simplicity, the mean absorbed dose in a specified organ or tissue is further referred to as *organ dose*, and the subscript T can be replaced by a specific organ. The general approach for the computation of dose starts by considering specifically the geometrical irradiation configuration of our application, depicted in figure 32. We can then write (B.7):

$$D_T = \frac{1}{m_T}\left(\int_{m_T} D_t\, dm\right) = \frac{1}{\rho\, A\, L}\int_{L1}^{L2} \Psi(z)\left(\frac{\mu_{en}}{\rho}\right) \rho\, A\, dz = \frac{1}{L}\int_{L1}^{L2} \Psi(z)\left(\frac{\mu_{en}}{\rho}\right) dz =$$

$$= \frac{N_0}{V}\, \varepsilon \left(\frac{\mu_{en}}{\rho}\right) \int_{L1}^{L2} \exp\left(-\left(\frac{\mu}{\rho}\right) \rho \frac{z}{\cos(\varphi)}\right) dz =$$

$$= \frac{N_0}{V\rho}\, \varepsilon \frac{\left(\frac{\mu_{en}}{\rho}\right)}{\left(\frac{\mu}{\rho}\right)} \left\{\exp\left[-\left(\frac{\mu}{\rho}\right)\rho\, L_1\right] - \exp\left[-\left(\frac{\mu}{\rho}\right)\rho\, L_2\right]\right\} \cos(\varphi)$$

where $L = L_2 - L_1$ is the in-depth length of the considered tissue with boundaries L_1 and L_2. Notice that the first term in the above equation (B.7) has dimension of energy/mass (dose), and it takes into account the amount of irradiated tissue ($V\,\rho = m_t$) and the energy of the primary photon beam ε. The second dimensionless term is the ratio between the mass energy absorption coefficient and the mass attenuation, and it depends explicitly on the chemical composition of the irradiated specimen (tissue) and the energy of the primary photons beam. Finally the last factor, also dimensionless, accounts for the total amount of photon absorbed in the irradiated volume of mass m_t and it depends on the geometry of the irradiation and photon attenuation along the in-depth direction.

Assuming that the irradiated rectal wall (R) length is of $L_R = 0.3$ cm ($L_{R1} = 0$; $L_{R2} = 0.3$ cm) and a prostate gland (P) of $L_P = 3$ cm ($L_{P1} = L_{R2} = 0.3$ cm; $L_{P2} = 3.3$ cm), both of mass density equals to 1.06 g/cm^3, the mean absorbed dose per impinging primary photon (beam diameter of 2 mm, corresponding to $A = 3.14$ mm^2) in these two tissues is obtained by applying the above equation (B.7), namely (B.8):

$$\frac{D_R}{N_0} = \frac{\varepsilon\, V_{eff}}{A\, L_R\, \rho} \frac{\left(\frac{\mu_{en}}{\rho}\right)}{\left(\frac{\mu}{\rho}\right)} \left\{1 - \exp\left[-\left(\frac{\mu}{\rho}\right)\rho\, L_R\right]\right\} \cos(\varphi) = 2.2\ \frac{KeV}{g} = 3.5\times10^{-13}\ Gy$$

$$\frac{D_P}{N_0} = \frac{\varepsilon}{A\, L_P\, \rho} \frac{\left(\frac{\mu_{en}}{\rho}\right)}{\left(\frac{\mu}{\rho}\right)} \left\{\exp\left[-\left(\frac{\mu}{\rho}\right)\rho\, L_R\right] - \exp\left[-\left(\frac{\mu}{\rho}\right)\rho\, (L_R+L_P)\right]\right\} \cos(\varphi) = 66\ \frac{KeV}{g} = 10^{-11}\ Gy$$

where the factor V_{eff} was introduced considering that only a small fraction of the colon is actually irradiated, while the dose is average over the wall tissue volume. The portion of irradiated colon can be estimated to be about 1% of the total organ (we may assume that the colon is 100 cm long and it has a diameter of 3 cm, so the total area is around 940 cm^2 while the irradiated area is solely of

9 cm^2). Mean absorbed dose delivered to tissue behind the prostate is much smaller compared to the dose delivered to the rectal wall and to the prostate, and thus in the following discussion it will be neglected. So the mean absorbed dose per impinging primary photon is given by the sum of the two above terms.

The total mean absorbed dose delivered to the rectal wall (D_R) and to the prostate (D_P) during an entire XRF scan is now calculated multiplied (B.8) by the total number of impinging primary photons (N_0^x). The latter are computed using the approach presented in section 6.2.3, known the sensitivity profile of the detection system (counts/ppm/primary-photon) as function of the irradiation depth and fixed a certain level of accuracy:

$$N_0^x = \frac{m}{Sensitivity(x)} \tag{B.9}$$

The choice of the value for the factor m strictly depends on the performances of the spectroscopic detector in terms of energy resolution and background and it affects the accuracy of the measurements as function of the irradiation depth. Since the most advanced detector, like SDD sensors, can provide peak-to-background ratio as high as 15k, we can estimate that a total of m = 1 count/ppm could be enough to guaranteed a LOD below 40-50 ppm (see for instance figure 63), for the relevant depths up to 8 mm. As an example, for a irradiation depth of 5 mm, using 145 mm^2 active area detector, the sensitivity is around 10^{-10}; it means that the number of primary photons we need to provide for each pixel, assuming a m = 1 counts/ppm for a LOD < 50 ppm, should be around 10^{10} photons. In summary, for a 2D XRF scan at depth x, the total mean absorbed dose delivered to the rectal wall (D_R) and to the prostate (D_P) is then calculated as:

$$D_R(x) = \frac{3.5\times10^{-13}}{Sensitivity(x)} \quad \frac{3.5\times10^{-13}}{Sensitivity(x)} \text{ Gy} \tag{B.10}$$

$$D_P(x) = \frac{10^{-11}}{Sensitivity(x)} \quad \frac{10^{-11}}{Sensitivity(x)} \text{ Gy} \tag{B.11}$$

The biological effects of radiation depend not only on the absorbed dose but also on the type of ionizing radiation. For this reason, in 1991, the International Commission on Radiological Protection (ICRP) introduced for dose limitation proposes a quantity called organ dose equivalent $H_{t,Y}$, based on the radiation weighting factor Q_R (also called quality factor, see table 6), and $D_{t,Y}$ the mean absorbed dose in a tissue or organ (t). Accordingly, the organ equivalent dose $H_{t,Y}$ in a tissue or organ t by the radiation type Y is

$$H_{t,Y} = D_{t,Y}\, Q_Y\, P \tag{B.12}$$

where P is the product of all other modifying factors, such as non-uniform distribution of internal deposited radionuclides (in our case, uniform distribution P = 1). The SI unit for both absorbed dose and dose equivalent is joule per kilogram, but the special name for SI unit of dose equivalent is Sievert (1 Sv = 1 Joule/kg).

Radiation	Quality factor
X-rays, γ-rays and electrons	1
Neutron	3-10 depending on the energy
Heavy particles	1-20

Table 6: Approximate quality radiation factors (Khan 2003)**.**

When the body is uniformly irradiated, the probability of occurrence of cancer or genetic defects (fatal and non-fatal) is assumed to be proportional to the dose equivalent, and risk can be represented by a single value. In reality, truly uniform whole-body exposures are rare. To deal with this situation, the ICRP introduced the concept of effective dose equivalent.

Tissue	Tissue Weighting factor
Gonads	0.20
Red bone marrow	0.12
Colon	0.12
Lung	0.12
Stomach	0.12
Bladder	0.05
Breast	0.05
Liver	0.05
Esophagus	0.05
Thyroid	0.05
Skin	0.01
Bone surfaces	0.01
Remainder	0.05

Table 7: recommended weighting factors for calculating effective dose equivalent (ICPR 1991)**.**

The effective dose equivalent is the sum of the weighted dose equivalents for all irradiated tissues, where the weighting factor W_t represents the different risk of each tissue to mortality from cancer and hereditary effects in the first two generations. The weighting factors W_t vary for different tissues (Tab. 7).

The dose due to all effects for an irradiated individual is represented as effective dose, ED, being the sum of the weighted equivalent doses over all organs (t) and over all the different types of radiation (Y). The sum of all the tissue weighting factors is unity.

$$ED = \sum_{Y} \sum_{t} H_{t;Y} W_t \tag{B.13}$$

Rectal wall, i.e. colon, has a tissue weighting factor of 0.12 while prostate has a tissue weighting factor 0.05. So the total effective dose is given by the following estimation: For external radiation sources of low linear energy transfer (LET), namely radiation that provide nearly uniform irradiation of the body, the risk of cancer incidence (morbidity) and mortality can be closely approximated using the conversion factors of 8×10^{-2} risk per Sievert and 6×10^{-2} risk per Sievert respectively (U. S. EPA/OAR/ORIA/Radiation Protection Division 1998). The radiation-induced cancer risk, as function of the radiation depth x, as consequence of a complete 2D XRF Zn-map image, with 1 counts/ppm per pixel, is then equal to

$$\text{Risk}(x) = 0.06 \left(\frac{3.5\times10^{-13}}{\text{Sensitivity}(x)}\ 0.12 + \frac{10^{-11}}{\text{Sensitivity}(x)}\ 0.05 \right) \tag{B.14}$$

The induced-cancer mortality profile, depicted in figure 88, was computed calculating the sensitivity for 145 mm^2 effective area detector for full 2D Zn-map images of prostate in 15x15 pixels (primary beam size of 2 mm).

List of publications resulting from this work

- Shilstein SSh, Cortesi M, Breskin A, Chechik R, Vartsky D, Raviv G, Kleinman N, Ramond J, Kogan G, Gladysh V, Moriel E, Huszar M, Volkov A and Fridman E, 2006. Prostatic Zn determination for prostate cancer diagnosis. *Talanta*, **70(5)**, 914-921.

- Cortesi M, Fridman E, Volkov A, Shilstein SSh, Chechik R, Breskin A, Vartsky D, Kleinman N, Kogan G, Moriel E, Gladysh V, Huszar M, Ramon J and Raviv G., 2008. Clinical assessment of the cancer diagnostic value of prostatic Zn: a comprehensive needle-biopsy study. *The Prostate*, **68(9)**, 994-1006.

- Cortesi M, Chechik R, Breskin A, Vartsky D, Ramon J, Raviv G, Volkov A and Fridman E, 2009. Evaluating the cancer detection and grading potential of prostatic-Zn imaging: a simulation study. *Physics in Medicine and Biology*, **54(3)**, 781-796.

- Cortesi M, Fridman E, Volkov A, Shilstein SSh, Chechik R, Breskin A, Vartsky D, Raviv G and Ramon J, 2010. New prospective for non-invasive detection, grading, size evaluation and tumor location of Prostate Cancer. *The Prostate*, **70(15),** 1701-1708.

Statement about independent collaboration

The development of the XRF probe and the Zn-based detection, grading and staging method is the subject of my Ph. D. thesis work which summarizes my independent efforts.

List of Figures

List of Tables

Bibliography

American Cancer Society, 2009. Cancer Facts and Figures 2009. Available at: http://www.cancer.org/.

Andriole, G.L. et al., 2009. Mortality Results from a Randomized Prostate-Cancer Screening Trial. *N Engl J Med*, 360(13), 1310-1319.

Aziz, D.C., Barathur A., Barathur R.B., 1993. Prostate-specific antigen and prostate volume: a meta-analysis of prostate cancer screening criteria. *J. Clin. Lab. Anal. 7*, 283–292.

Babaian, R.J., Mettlin C., Kane R., et al., 1992. The relationship of prostate-specific antigen to digital rectal examination and transrectal ultrasonography. *Cancer* 69, 1195–1200.

Bangma C.H., Grobbee D.E. and Schroder F.H., 1995. Volume adjustment for intermediate prostate-specific antigen values in a screening population. *Eur. J. Cancer* 31(A), 12–14.

Beckhoff, B. et al., 2006. *Handbook of Practical X-Ray Fluorescence Analysis* 1st ed., Springer.

Berney, D.M., 2007. Low Gleason score prostatic adenocarcinomas are no longer viable entities. *Histopathology*, 50(6), 683-690.

Bertrand, G. & Vladesco, R., 1921. Intervention probable du zinc dans les phénomènes de fécondation chez les animaux vertébrates. *C R Hebd Seances Acad Sci*, 173, 176-179.

Bilderback, D.H., Elleaume, P. & Weckert, E., 2005. Review of third and next generation synchrotron light sources. *Journal of Physics B: Atomic, Molecular and Optical Physics*, 38(9), S773-S797.

Bjeoumikhov, A., Arkadiev, V. et al., 2005. A new microfocus x-ray source, iMOXS, for highly sensitive XRF analysis in scanning electron microscopes. *X-Ray Spectrometry*, 34(6), 493-497.

Bjeoumikhov, A., Langhoff, N. et al., 2005. Capillary optics for micro x-ray fluorescence analysis. *Review of Scientific Instruments*, 76(6), 063115.

Bloom, J.R. et al., 2006. Family History, Perceived Risk, and Prostate Cancer Screening among African American Men. *Cancer Epidemiology Biomarkers & Prevention*, 15(11), 2167-2173.

Blume, P.A., 2007. *The LabVIEW Style Book (National Instruments Virtual Instrumentation Series)*, Prentice Hall PTR. Available at: http://portal.acm.org/citation.cfm?id=1206161 [Accessed February 23, 2010].

Bostwick, D.G., 1995. High grade prostatic intraepithelial neoplasia: The most likely precursor of prostate cancer. *Cancer*, 75(7 SUPPL.), 1823-1836.

Bray, T.M., Kubow, S. & Bettger, W.J., 1986. Effect of Dietary Zinc on Endogenous Free Radical Production in Rat Lung Microsomes. *J. Nutr.*, 116(6), 1054-1060.

Bronk et al., 2001. ArtTAX - a new mobile spectrometer for energy-dispersive micro X-ray fluorescence spectrometry on art and archaeological objects. *Fresenius' Journal of Analytical Chemistry*, 371(3), 307-316.

Bzhaumikhov, A.A., 1998. Monochromatizing x-ray concentrator (MONO-XC). In *Proceedings of SPIE*. X-Ray Optics, Instruments, and Missions. San Diego, CA, USA, pp. 512-516. Available at: http://spie.org/x648.html?product_id=331270 [Accessed February 23, 2010].

Carreras, A. & Mendoza, C., 1990. Zinc levels in seminal plasma of fertile and infertile men. *Andrologia*, 22(3), 279-283.

Catalona, W.J. et al., 2000. Comparison of percent free PSA, PSA density, and age-specific PSA cutoffs for prostate cancer detection and staging. *Urology*, 56(2), 255-260.

Catz, S.D. & Johnson, J.L., 2003. BCL-2 in prostate cancer: a minireview. *Apoptosis: An International Journal on Programmed Cell Death*, 8(1), 29-37.

Chan R.H., Ho C.W. and Nikolova M., 2005. Salt-and-Pepper Noise Removal by Median-type Noise Detectors and Edge-preserving Regularization. *IEEE Transactions on Image Processing* 14, 1479-1485.

Concato, J. et al., 2006. The effectiveness of screening for prostate cancer: a nested case-control study. *Archives of Internal Medicine*, 166(1), 38-43.

Cortesi, M. et al., 2009. Evaluating the cancer detection and grading potential of prostatic-zinc imaging: a simulation study. *Physics in Medicine and Biology*, 54(3), 781-796.

Cortesi, M. et al., 2008. Clinical assessment of the cancer diagnostic value of prostatic zinc: a comprehensive needle-biopsy study. *The Prostate*, 68(9), 994-1006.

Costello, L.C. et al., 2004. Role of zinc in the pathogenesis and treatment of prostate cancer: critical issues to resolve. *Prostate Cancer and Prostatic Diseases*, 7(2), 111-117.

Costello, L.C. & Franklin, R.B., 1997. Citrate metabolism of normal and malignant prostate epithelial cells. *Urology*, 50(1), 3-12.

Costello, L.C. & Franklin, R.B., 2009. Prostatic fluid electrolyte composition for the screening of prostate cancer: a potential solution to a major problem. *Prostate Cancer and Prostatic Diseases*, 12(1), 17-24.

Costello, L.C. & Franklin, R.B., 2006. The clinical relevance of the metabolism of prostate cancer; zinc and tumor suppression: connecting the dots. *Molecular Cancer*, 5, 17.

Costello, L.C. et al., 2005. Zinc and prostate cancer: a critical scientific, medical, and public interest issue (United States). *Cancer Causes & Control: CCC*, 16(8), 901-915.

Costello, L.C. et al., 2000. Zinc causes a shift toward citrate at equilibrium of the m-aconitase reaction of prostate mitochondria. *Journal of Inorganic Biochemistry*, 78(2), 161-165.

Costello, L.C., Franklin, R.B. and Narayan P., 1999. Citrate in the diagnosis of Prostate Cancer. *The Prostate* 38 237-245.

Costello, L.C., Liu, Y. & Franklin, R.B., 1995. Testosterone stimulates the biosynthesis of m-aconitase and citrate oxidation in prostate epithelial cells. *Molecular and Cellular Endocrinology*, 112(1), 45-51.

Costello, L.C. and Franklin, R.B. 1994. Bioenergetic theory of prostate malignancy. *Prostate*, 25(3), 162-166.

Cupp, M.R. et al., 1995. The volume of prostate cancer in the biopsy specimen cannot reliably predict the quantity of cancer in the radical prostatectomy specimen on an individual basis. *The Journal of Urology*, 153(5), 1543-1548.

Currie, L.A., 1995. Nomenclature in evaluation of analytical methods including detection and quantification capabilities (IUPAC Recommendations 1995). *Pure and Applied Chemistry*, 67(10), 1699-1723.

Degani H., Gusis V., Weinstein D., Fields S. and Strano S., 1997. Mapping pathophysiological features of breast tumors by MRI at high spatial resolution. *Nature Medicine* 3, 780 - 782.

De Samber, B. et al., 2008. Three-dimensional elemental imaging by means of synchrotron radiation micro-XRF: developments and applications in environmental chemistry. *Analytical and Bioanalytical Chemistry*, 390(1), 267-271.

De Visschere, P., Oosterlinck, W., De Meerleer, G. and Villeirs, G., 2010. Clinical and imaging tools in the early diagnosis of prostate cancer, a review. *JBR-BTR*, 93(2), 62-70.

Dhar, N.K. et al., 1973. Distribution and concentration of zinc in the subcellular fractions of benign hyperplastic and malignant neoplastic human prostate. *Experimental and Molecular Pathology*, 19(2), 139-142.

Dhez, P. et al., 1999. Instrumental aspects of x-ray microbeams in the range above 1 keV. *Review of Scientific Instruments*, 70(4), 1907-1920.

Ding, X., Gao, N. & Havrilla, G.J., 2000. Monolithic polycapillary x-ray optics engineered to meet a wide range of applications. Available at: http://adsabs.harvard.edu/abs/2000SPIE.4144..174D.

Edwards, C., 1999. Fundamental quantities and units for ionizing radiation -- ICRU report 60. *Medical Engineering & Physics*, 21(4), 277.

Epstein, J.I., 2000. Gleason score 2-4 adenocarcinoma of the prostate on needle biopsy: a diagnosis that should not be made. *The American Journal of Surgical Pathology*, 24(4), 477-478.

Epstein, J.I. et al., 2005. The 2005 International Society of Urological Pathology (ISUP) Consensus Conference on Gleason Grading of Prostatic Carcinoma. *The American Journal of Surgical Pathology*, 29(9), 1228-1242.

Epstein, J.I. et al., 1993. Is tumor volume an independent predictor of progression following radical

prostatectomy? A multivariate analysis of 185 clinical stage B adenocarcinomas of the prostate with 5 years of followup. *The Journal of Urology*, 149(6), 1478-1481.

Etzioni, R. et al., 2002. Overdiagnosis due to prostate-specific antigen screening: lessons from U.S. prostate cancer incidence trends. *Journal of the National Cancer Institute*, 94(13), 981-990.

Faulkner, K. & Law, J., 2005. Mammographic breast cancer screening for women previously treated with high breast doses for diseases such as Hodgkin's. *Radiation Protection Dosimetry*, 117(1-3), 330-333.

Fawcett, T., 2004. ROC Graphs: Notes and Practical Considerations for Researchers. *HP Laboratories*, Tech Report. HPL-2003-4.

Feustel, A. et al., 1982. Zinc and cadmium concentration in prostatic carcinoma of different histological grading in comparison to normal prostate tissue and adenofibromyomatosis (BPH). *Urological Research*, 10(6), 301-303.

Fuchsjäger, M., Shukla-Dave, A., Akin, O., Barentsz J. and Hricak H., 2008. Prostate Cancer Imaging. Acta Radiol., 49(1), 107-120.

Futterer, J.J., Scheenen, T.W., Huisman, H.J., et al., 2004. Initial experience of 3 Tesla endorectal coil magnetic resonance imaging and 1H-spectroscopic imaging of the prostate. I*nvest. Radiol.*, 39, 671-680.

Fiorini, C. & Longoni, A., 2008. Semiconductor drift detectors for X- and gamma-ray spectroscopy and imaging. *Nuclear Instruments and Methods in Physics Research Section B: Beam Interactions with Materials and Atoms*, 266(10), 2173-2181.

Fiorini, C., Longoni, A. & Bjeoumikhov, A., 2001. A new detection system with polycapillary conic collimator for high-localized analysis of X-ray fluorescence emission. *IEEE Transactions on Nuclear Science*, 48(3), 268-271.

Food and Drug Administration, 2010. Full body scanning using Computer Tomography (CT). Available at: http://www.fda.gov/ [Accessed February 18, 2010].

Forster, R.A. et al., 2004. MCNP(TM) Version 5. *Nuclear Instruments and Methods in Physics Research Section B: Beam Interactions with Materials and Atoms*, 213, 82-86.

Fradet, V., Kurhanewicz, J., Cowan, J.E., Karl, A., Coakley, F.V., Shinohara, K., Carroll, P.R.., 2010. Prostate cancer managed with active surveillance: role of anatomic MR imaging and MR spectroscopic imaging. *Radiology*, 256(1), 176-83

Franklin, R.B. et al., 2005. Zinc and zinc transporters in normal prostate and the pathogenesis of prostate cancer. *Frontiers in Bioscience: A Journal and Virtual Library*, 10, 2230-2239.

Freedland, S.J. et al., 2005. Prostate Size and Risk of High-Grade, Advanced Prostate Cancer and Biochemical Progression After Radical Prostatectomy: A Search Database Study. *J Clin Oncol*, 23(30), 7546-7554.

Gao, N. et al., 1997. Enhancement of microbeam x-ray fluorescence analysis using monolithic polycapillary focusing optics. *Applied Physics Letters*, 71(23), 3441-3443.

Gardner, W.A., 1982. Histologic grading of prostate cancer: a retrospective and prospective overview. *The Prostate*, 3(6), 555-561.

Gleason, D.F., 1992. Histologic grading of prostate cancer: a perspective. *Human Pathology*, 23(3), 273-279.

Goldstone, K., 1990. Tissue Substitutes in Radiation Dosimetry and Measurement, ICRU Report 44, International Commission on Radiation Units and Measurements, USA (1989). *Clinical Radiology*, 41(3), 220.

Gonick, P. et al., 1969. Atomic absorption spectrophotometric determination of zinc in the prostate. *Investigative Urology*, 6(4), 345-347.

Govindaraju, S.K. et al., 2008. Tissue characterisation in prostate cancer using a novel ultrasound approach. *British Journal of Medical and Surgical Urology*, 1(3), 98-106.

Graif, T., Loeb S., Roehl K.A., Gashti S.N., Griffin C., Yu X. and Catalona W.J., 2007. Under diagnosis and over diagnosis of prostate cancer. *The Journal of Urology*, 178(1), 88-92.

Gyorkey, F. et al., 1967. Zinc and Magnesium in Human Prostate Gland: Normal, Hyperplastic, and Neoplastic. *Cancer Res*, 27(8_Part_1), 1348-1353.

Habib, F.K. et al., 1979. Cancer of the prostate: early diagnosis by zinc and hormone analysis? *British Journal of Cancer*, 39(6), 700-704.

Hambidge, K.M. & Krebs, N.F., 2007. Zinc deficiency: a special challenge. *The Journal of Nutrition*, 137(4), 1101-1105.

Hand, D.J. & Till, R.J., 2001. A Simple Generalisation of the Area Under the ROC Curve for Multiple Class Classification Problems. *Machine Learning*, 45(2), 171-186.

Hicks, J.J. et al., 1972. Metabolic changes in human spermatozoa related to capacitation. *Fertility and Sterility*, 23(3), 172-179.

Hill, A.V., 1910. A new mathematical treatment of changes of ionic concentration in muscle and nerve under the action of electric currents, with a theory as to their mode of excitation. *The Journal of Physiology*, 40(3), 190-224.

Hoare, R., Deeory, G.E. & Penner, D.W., 1956. Zinc and acid phosphatase in the human prostate. *Cancer*, 9(4), 721-726.

Hubbell, J.H. and Berger M.J. 1968. Sec. 4.1: Attenuation Coefficients, Energy Absorption Coefficients, and Related Quantities. and Sec. 4.2: Photon Atomic Cross Sections, in Engineering Compendium on Radiation Shielding, Vol. 1, R.G. Jaeger, ed. (Springer, Berlin), 167-202.

Humphrey, P.A., 2004. Gleason grading and prognostic factors in carcinoma of the prostate. *Mod Pathol*, 17(3), 292-306.

Humphrey, P.A., 2003. *Prostate Pathology*, American Society Clinical Pathology.

ICPR, R.N.6., 1991. Annex A Quantities used in radiological protection. *Annals of the ICRP*, 21(1-3), 79-89.

ICRP, 1975. *ICRP Publication 23: Reference Man: Anatomical, Physiological and Metabolic Characteristics: Reference Manual*, Elsevier.

ICRU, 1989. *Tissue substitutes in radiation dosimetry and measurement.*, (Bethesda, Md., U.S.A): International Commission on Radiation Units and Measurements. Available at: http://openlibrary.org/b/OL2047861M/Tissue_substitutes_in_radiation_dosimetry_and_measurement. [Accessed April 15, 2010].

Ide-Ektessabi, A. et al., 2002. Quantitative analysis of zinc in prostate cancer tissues using synchrotron radiation microbeams. *X-Ray Spectrometry*, 31(1), 7-11.

IFG - Institute for Scientific Instruments GmbH, Germany, (http://www.ifg-adlershof.de/).

Iguchi, K. et al., 1998. Induction of necrosis by zinc in prostate carcinoma cells and identification of proteins increased in association with this induction. *European Journal of Biochemistry / FEBS*, 253(3), 766-770.

Jeldres, C. et al., 2008. Validation of the contemporary epstein criteria for insignificant prostate cancer in European men. *European Urology*, 54(6), 1306-1313.

Jemal, A. et al., 2007. Cancer Statistics, 2007. *CA Cancer J Clin*, 57(1), 43-66.

Jenkins, R. & Gilfrich, J.V., 1992. Figures-of-merit, their philosophy, design and use. *X-Ray Spectrometry*, 21(6), 263-269.

Jiang, Z. et al., 2004. Alpha-methylacyl-CoA racemase: a multi-institutional study of a new prostate cancer marker. *Histopathology*, 45(3), 218-225.

Karam, J.A. et al., 2007. Caveolin-1 overexpression is associated with aggressive prostate cancer recurrence. *The Prostate*, 67(6), 614-622.

Kavanagh, J.P., 1985. Sodium, potassium, calcium, magnesium, zinc, citrate and chloride content of human prostatic and seminal fluid. *Journal of Reproduction and Fertility*, 75(1), 35-41.

Kavanagh, J.P., 1983. Zinc binding properties of human prostatic tissue, prostatic secretion and seminal fluid. *Journal of Reproduction and Fertility*, 68(2), 359-363.

KETEK - X-Ray Detectors, Germany (http://www.ketek.net/).

Key, M.H., 1985. Laboratory production of X-ray lasers. *Nature*, 316(6026), 314-319.

Khan, F.M., 2003. *The Physics of Radiation Therapy* Third Edition., Lippincott Williams & Wilkins.

Kotsiantis, S., Zaharakis, I. & Pintelas, P., 2006. Supervised machine Learning: a review of classification techniques. *Artificial Intelligence Review*, 26(3), 159-190.

Kravchick, S. et al., 2003. Colour Doppler ultrasonography for detecting perineural invasion (PNI) and the value of PNI in predicting final pathological stage: a prospective study of men with clinically localized prostate cancer. *BJU International*, 92(1), 28-31.

Kumakhov, M.A., 2000a. Kumakhov Optics and Application. Available at: http://adsabs.harvard.edu/abs/2000SPIE.4155.....K.

Kumakhov, M.A., 2000b. Capillary optics and their use in x-ray analysis. *X-Ray Spectrometry*, 29(5), 343-348.

Kyotokagaku Co., Ltd., Japan, (http://www.kyotokagaku.com/index.html).

Lahtonen, R., 1985. Zinc and cadmium concentrations in whole tissue and in separated epithelium and stroma from human benign prostatic hypertrophic glands. *The Prostate*, 6(2), 177-183.

Lechner, P. et al., 1996. Silicon drift detectors for high resolution room temperature X-ray spectroscopy. *Nuclear Instruments and Methods in Physics Research Section A: Accelerators, Spectrometers, Detectors and Associated Equipment*, 377(2-3), 346-351.

Lee, T.H., Kantoff, P.W. & McNaughton-Collins, M., 2009. Screening for prostate cancer. *The New England Journal of Medicine*, 360(13), e18.

Leman, E.S. et al., 2007. EPCA-2: a highly specific serum marker for prostate cancer. *Urology*, 69(4), 714-720.

Liang, J.Y. et al., 1999. Inhibitory effect of zinc on human prostatic carcinoma cell growth. *The Prostate*, 40(3), 200-207.

Liebscher, K. & Smith, H., 1968. Essential and nonessential trace elements. A method of determining whether an element is essential or nonessential in human tissue. *Archives of Environmental Health*, 17(6), 881-890.

Littrup, P.J. et al., 1991. Determination of prostate volume with transrectal US for cancer screening. Part II. Accuracy of in vitro and *in-vivo* techniques. *Radiology*, 179(1), 49-53.

Lloyd, S., 1982. Least squares quantization in PCM. *Information Theory, IEEE Transactions on*, 28(2), 129-137.

Lotan, T.L. & Epstein, J.I., 2010. Clinical implications of changing definitions within the Gleason grading system. *Nat Rev Urol*, 7(3), 136-142.

MacDonald, R.S., 2000. The Role of Zinc in Growth and Cell Proliferation. *J. Nutr.*, 130(5), 1500S-1508.

Macqueen, J., 1967. Some methods of classification and analysis of multivariate observations. In *Proceedings of the Fifth Berkeley Symposium on Mathematical Statistics and Probability*. pp. 297, 281.

Mann, T. & Lutwak-Mann, C., 1981. *Male Reproductive Function and Semen*, Springer-Verlag Berlin and Heidelberg GmbH & Co. KG.

Marks, L.S. & Bostwick, D.G., 2008. Prostate Cancer Specificity of PCA3 Gene Testing: Examples from Clinical Practice. *Reviews in Urology*, 10(3), 175-181.

Mawson, C.A. & Fischer, M.I., 1952. The occurrence of zinc in the human prostate gland. *Can. J. Med. Sci.*, 30, 336-339.

Mawson, C.A. & Fischer, M.I., 1951. Zinc Content of the Genital Organs of the Rat. *Nature*, 167(4256), 859.

May, R.A. & Stevenson, K.J., 2009. Software Review of Origin 8. *Journal of the American Chemical Society*, 131(2), 872.

McNeal, J.E., 2003. Origin and development of carcinoma of the prostate. *Aktuelle Urologie*, 34(2), 81-82.

McNeal, J.E. et al., 1988. Zonal distribution of prostatic adenocarcinoma. Correlation with histologic pattern and direction of spread. *The American Journal of Surgical Pathology*, 12(12), 897-906.

McWilliam, L.J., Roberts, I.S.D. & Davies, D.R., 2002. Problems in grading and staging prostatic carcinoma. *Current Diagnostic Pathology*, 8(2), 65-75.

Mikuz, G., 1997. Pathology of prostate cancer. Old problems and new facts. *Advances in Clinical Pathology: The Official Journal of Adriatic Society of Pathology*, 1(1), 21-34.

Miller, L.H., 1956. Table of Percentage Points of Kolmogorov Statistics. *Journal of the American Statistical Association*, 51(273), 111-121.

Mol, A.J.M. et al., 2007. New experimental markers for early detection of high-risk prostate cancer: role of cell-cell adhesion and cell migration. *Journal of Cancer Research and Clinical Oncology*, 133(10), 687-695.

Mood, A.M., Graybill, F.A. & Boes, D.C., 1974. *Introduction to the Theory of Statistics* 3rd ed., McGraw-Hill Companies.

Moskalik, A. et al., 2001. Analysis of three-dimensional ultrasound Doppler for the detection of prostate cancer. *Urology*, 57(6), 1128-1132.

Nakanouchi, T. et al., 2001. Possible use of transrectal power Doppler imaging as an indicator of microvascular density of prostate cancer. *Urology*, 58(4), 573-577.

Nayyar, R., Kumar, R., Kumar, V., Jagannathan, N.R., Gupta, N.P. and Hemal, A.K., 2009. Magnetic resonance spectroscopic imaging: current status in the management of prostate cancer. *BJU Int.*, 103(12) 1614-20.

National Institute of Standard and Technology - NIST, X-Ray Mass Attenuation Coefficients, (http://physics.nist.gov/PhysRefData/XrayMassCoef/cover.html).

Naz, R.K., 1997. *Prostate: basic and clinical aspect* 1st ed., Informa Health Care.

Negendank, W. 1992. Studies of human tumors by MRS: a review. *NMR Biomed*, 5(5), 303-324.

Noguchi, M. et al., 2000. An analysis of 148 consecutive transition zone cancers: clinical and histological characteristics. *The Journal of Urology*, 163(6), 1751-1755.

Petrescu, A. et al., 2006. Immunohistochemical detection of p53 protein as a prognostic indicator in prostate carcinoma. *Romanian Journal of Morphology and Embryology = Revue Roumaine De Morphologie Et Embryologie*, 47(2), 143-146.

Panebianco V., Sciarra A., et al. 2009. Role of magnetic resonance spectroscopic imaging (MRSI) and dynamic contrast-enhanced MRI (DCE-MRI) in identifying prostate cancer foci in patients with negative biopsy and high levels of prostate specific antigen (PSA). *Radiol. Medic.*, DOI 10.1007/s11547-010-0575-3.

Pham, D.L., Xu, C. & Prince, J.L., 2000. Current methods in Medical Image Segmentation. *Annual Review of Biomedical Engineering*, 2(1), 315-337.

PNsensor GmbH, Germany, (http://www.pnsensor.de/).

Prasad, A., 1982. *Clinical, biochemical, and nutritional aspects of trace elements*, (New York): A.R. Liss.

Ramos, V. & Muge, 2000. Map Segmentation by Colour Cube Genetic K-Mean Clustering. In *Lecture Notes In Computer Science*. Springer-Verlag, pp. 319-323.

Richardson, W.H., 1972. Bayesian-Based Iterative Method of Image Restoration. *Journal of the Optical Society of America*, 62(1), 55-59.

Sauter, G. & Cancer, I.A.F.R.O., 2004. *WHO Classification of Tumors: Pathology and Genetics of Tumors of the Urinary System and Male Genital Organs* 1st ed., International Agency for Research on Cancer.

Scattoni, V. et al., 2005. Detection and diagnosis of prostate cancer: what's new. *Archivio Italiano Di Urologia, Andrologia: Organo Ufficiale [di] Società Italiana Di Ecografia Urologica E Nefrologica / Associazione Ricerche in Urologia*, 77(3), 173-179.

Schröder, F.H. et al., 2009. Screening and prostate-cancer mortality in a randomized European study. *The New England Journal of Medicine*, 360(13), 1320-1328.

Schrodt, G.R., Hall, T. & Jr, W.F.W., 1964. The concentration of zinc in diseased human prostate glands. *Cancer*, 17(12), 1555-1566.

Selly S., Donovan J., Faulkner A., Coast J. and Gillatt D., 1997. Diagnosis, management and screening of early localised prostate cancer. *Health Technology Assessment* 1(2), 1-97.

Seltzer, S.M., 1993. Calculation of Photon Mass Energy-Transfer and Mass Energy-Absorption Coefficients. *Radiation Research*, 136(2), 147-170.

Shankar, A. & Prasad, A., 1998. Zinc and immune function: the biological basis of altered resistance to infection. *Am J Clin Nutr*, 68(2), 447S-463.

Shannon, B.A., McNeal, J.E. & Cohen, R.J., 2003. Transition zone carcinoma of the prostate gland: a common indolent tumor type that occasionally manifests aggressive behaviour. *Pathology*, 35(6), 467-471.

Shilstein, S.S. et al., 2004. *In-vivo* determination of prostatic zinc: phantom feasibility study. *Physics in Medicine and Biology*, 49(4), 485-499.

Shilstein, S.S. et al., 2006. Prostatic Zn determination for prostate cancer diagnosis. *Talanta*, 70(5), 914-921.

Shukla-Dave, A., Hricak, H., Moskowitz, C., et al., 2007. Detection of prostate cancer with MR spectroscopic imaging: An expanded paradigm incorporating Polyamines. *Radiology*, 245, 499–506.

Singh, K.K. et al., 2006. Mitochondrial aconitase and citrate metabolism in malignant and nonmalignant human prostate tissues. *Molecular Cancer*, 5, 14.

Sosna, J., Pedrosa, I., Dewolf, W.C., Mahallati, H., Lenkinski, R.E. and Rofsky, N.M., 2004. MR imaging of the prostate at 3 Tesla: comparison of an external phased-array coil to imaging with an endorectal coil at 1.5 Tesla. *Acad. Radiol.* 11 857–862.

Stenman, U.H. et al., 1998. The clinical importance of free prostate-specific antigen (PSA). *Current Opinion in Urology*, 8(5), 393-399.

Theodorescu, D., 2009. Prostate Cancer - Biology, Diagnosis, Pathology, Staging, and Natural History: eMedicine Urology. Available at: http://emedicine.medscape.com/article/458011-overview.

Tipton, I.H. & Cook, M.J., 1963. Trace elements in human tissue. II. Adult subjects from the United States. *Health Physics*, 9, 103-145.

U. S. EPA/OAR/ORIA/Radiation Protection Division, 1998. Risk Assessment Publications. Available at: http://www.epa.gov/radiation/assessment/pubs.html.

Vallee, B.L. & Falchuk, K.H., 1993. The biochemical basis of zinc physiology. *Physiological Reviews*, 73(1), 79-118.

Vartsky, D. et al., 2003. Prostatic zinc and prostate specific antigen: an experimental evaluation of their

combined diagnostic value. *The Journal of Urology*, 170(6 Pt 1), 2258-2262.

Vincze, L., 2004. X-ray fluorescence microtomography- and polycapillary-based confocal imaging using synchrotron radiation. In *Proceedings of SPIE*. Developments in X-Ray Tomography IV. Denver, CO, USA, pp. 220-231. Available at: http://spie.org/x648.html?product_id=560416 [Accessed February 23, 2010].

X and Gamma Ray Electronics XG-Lab, Italy (http://www.xglab.it/).

Yan, M. et al., 2008. Zinc deficiency alters DNA damage response genes in normal human prostate epithelial cells. *The Journal of Nutrition*, 138(4), 667-673.

Zaichick, V., Sviridova, T.V. & Zaichick, S.V., 1997. Zinc in the human prostate gland: normal, hyperplastic and cancerous. *International Urology and Nephrology*, 29(5), 565-574.

Zakian, K.L., Sircar, K., Hricak, H., et al., 2005. Correlation of Proton MR Spectroscopic Imaging with Gleason Score Based on Step-Section Pathologic Analysis after Radical Prostatectomy. *Radiology*, 234, 804-814.

תקציר:

השיטות הנפוצות כיום לניפוי סרטן הערמונית (PSA, DRE, TRUS) לוקות בחוסר רגישות ובחוסר ספציפיות, ולא ניתן להבחין באמצעות אף אחת מהן בין גידול לא תוקפני לבין סרטן קטלני. משום כך יש לפתח שיטות חלופיות בעלות רגישות וספציפיות יתרות לשם סינון יעיל יותר של חולים המועמדים לביופסיה, שתהיינה בעלות יכולת להנחות את מחט הביופסיה.

מטרתו העיקרית של מחקר זה הינה פיתוח של שיטה וכלי חדישים ובלתי-פולשניים אשר יאפשרו גילוי, מיקום, אבחון ומעקב אחר סרטן הערמונית. השיטה מבוססת על דימות בגוף החי (in vivo) של התפלגות אבץ בחלקים הפריפריאליים של הערמונית, באמצעות גשוש טראנס-רקטאלי הפועל על עקרון פלואורסנציה של קרינת X (XRF).

במסגרת מחקר קליני מקיף אשר כלל כמה מאות מטופלים, רמות אבץ מקומיות שנמדדו ברקמות ביופסיה בגודל 1-4 ממ"ק הראו מתאם חד משמעי עם הסיווג ההיסטולוגי של הרקמה (לא סרטנית או סרטן הערמונית) וכן מתאם חיובי עקבי בין רמות דילול האבץ לבין דרגת האלימות של הסרטן (סיווג Gleason). ניתוח מפורט של תמונות ריכוז אבץ שנוצרו בהדמיה באמצעות מחשב (תוך שימוש במשתנים שנלקחו מניסויים קליניים) הוכיח את יכולתה של השיטה לספק זיהוי ומיפוי רגישים וספציפיים של הנגע ואפיון דרגתו ומידת התפשטותו. ניתוח זה גם הניב מידע חיוני בנוגע לפרמטרים כגון כושר ההפרדה של התמונה וסטטיסטיקת הספירה, הנדרשים מגשוש XRF טראנס-רקטאלי לשם מיפוי בגוף החי של אבץ הערמונית בחולים. הגשוש ורכיביו השונים תוכננו ועברו תהליכי ייעול באמצעות ניסויים על עצמים דמויי ערמונית המכילים נגעים דמויי-גידול ממאיר ועל ידי ביצוע הדמיות מחשב בשיטות מונטה-קארלו. ניתוח רב-משתנים של הנתונים שנאספו בניסוי אישר את התחזיות שהתקבלו מההדמיה עבור מערכת גילוי הפלואורסנציה, כגון מנת הקרינה שנבלעה, סטטיסטיקות ספירה, כושר הפרדת הסריקה, נפח המטרה והדיוק במציאת מיקום נגעים בעלי נפח קטן דמויי-גידול ממאיר בעומקים שונים בתוך מטרות דמויות-רקמה.

המחקר הקליני, הדמיות המונטה-קארלו וניתוח מפות האבץ סיפקו מידע חיוני וחזון מבטיח באשר לביצועים הצפויים של שיטת גילוי סרטן הערמונית המבוססת על רמות אבץ. הדמיות שהתמקדו בתכנון הגשוש הרפואי וביצועיו ברמות קרינה מותרות הניבו תוצאות חיוביות אשר אוששו על ידי סדרת ניסויי מעבדה באמצעות מערכת פלואורסנציית קרינת X שולחנית.

מחקר זה הביא לתכנון רעיוני של גשוש רפואי טראנס-רקטאלי לדימות אבץ בערמונית למטרות גילוי סרטן הערמונית ואבחון רמת אלימותו וכן אפשר ניתוח ביצועיו הצפויים של הגשוש.